AMMONIA ELECTRO-SYNTHESIS FROM NITROGEN AND WATER USING A CYCLIC LITHIUM-MEDIATED METHOD

ZHU YINGGANG

MPhil

The Hong Kong Polytechnic University

2023

The Hong Kong Polytechnic University
Department of Mechanical Engineering

Ammonia Electro-synthesis from Nitrogen and Water Using a Cyclic Lithium-mediated Method

Zhu Yinggang

A thesis submitted in partial fulfillment of the
requirements for the degree of Master of Philosophy

August 2022

CERTIFICATE OF ORIGINALITY

I hereby declare that this thesis is my own work and that, to the best of my knowledge and belief, it reproduces no material previously published or written, nor material that has been accepted for the award of any other degree or diploma, except where due acknowledgment has been made in the text.

Zhu Yinggang

Abstract

Ammonia (NH_3) synthesis is vital to feed a growing world population. However, its primary synthesizing method, the Haber-Bosch process, is fossil fuels-powered and unsatiable. The lithium-mediated pathway has shown to be a promising alternative to produce ammonia with renewable feedstocks and electric energy. However, its continuous operation is still hampered by limited methods to plate Li stably from its aqueous solution because of its exceptionally high reactivity. In this study, a novel lithium metal battery (LMB)-mimic strategy, consisting of Li^+ recovery and Li plating steps, is adapted to electro-plate lithium metals from its aqueous solution. Li^+ in the solution is extracted spontaneously by a Li-deficient electrode in the Li recovery step and then electro-plated into metallic Li in a Li-friendly system by the Li plating steps. The obtained Li deposits could be utilized for subsequent nitridation and ammonia synthesis.

The LMB-mimic system gave a Li plating efficiency exceeding 95% when the capacity of Li deposits was over 12.65 mAh cm^{-2}. This result was similar to the Faradic efficiency (FE) towards ammonia. After the plating capacity was increased to over 15 mAh cm^{-2}, the FE could reach more than 92 %, which is among the best-reported values. From the experimental results and characterization, the solid-electrolyte interphase (SEI) layer was found to play an essential role in high-efficiency Li plating. During Li plating, a limited amount of Li would be consumed upon its first contact with the electrolyte, forming a protective layer to avoid further consumption. Furthermore, the LMB-mimic system can be operated stably because of the highly reversible phase transition of $LiMn_2O_4$ during the Li recovery and plating process. This research provides a stable and efficient method for sustainable ammonia synthesis under ambient pressure.

Acknowledgments

This thesis results from several years of literature reading, experiments, and group meetings. I could not finish it without the help and support of many people.

First of all, I would like to express my thanks to my chief supervisor, Prof. CHEN Guohua, who has been influential in helping me in both my study and research. I truly appreciate every time he gives me guidance and suggestions when I need them. And I also appreciate the freedom he gives me so that I could try some of the ideas whenever they came up. I want to thank him for giving me the chance to work in his research group. I am grateful of the support and suggestions whenever I fall into a dilemma in my research, as well as in my life. He is an incredible mentor and always cares about the individual development of his team members.

I also want to thank my co-supervisor, Dr. LIU Qiang, for his suggestions and support in my research work whenever I needed them. And I appreciate his patience in listening to my talk about my troubles in my research work or life. To me, he is not only the mentor who provides guidance and suggestions but also a true friend who can directly point out my mistakes and cheer me up. I am sincerely thankful that he took me to the church, spent time together, inspired me, and pulled me up when I was down. His optimistic attitude influenced me positively.

I appreciate the help and support from my research groupmates, Dr. YU Xiaoliang, Dr. LIN Cong, Dr. WANG Jingwei, Dr. ZHU Yanan, Dr. LIU Yang, Dr. Bai Zhaowen, Dr. ZHANG Fei, Dr. QIN Xusong, Dr. Soumyadip MAJUMDER, Dr. HUANG Lei, Mr. WENG Qingsong, Mr. HU Liang, Mr. Hassan RAZA, Mr. Subash KANDASMY, Mr. CHEN Junjie, Mr. JIANG Kai, Miss LIU Yutong, Miss ZHOU Zeqi, Miss XIE Chuyi. Thanks for your support and advice in my experiments and lab work. The harmonious atmosphere in the research group always warms me up. And special thanks also go to my friend, Dr. ZHANG Fei, for cheering me up and helping me a lot when I was down with medicine.

I would like to thank Ms. Lily Tam and Merlin Wong from the ME department. They are so professional in their work. Their support and help in my study, especially the suggestion on smoothly changing my research programs, mean a lot to me. Thanks for the office seat provided by Dr. Curtis Ng, and Mr. Benny LEUNG for the help in ordering gases and coping with lab affairs. And I would like to thank Dr. Hardy LUI and Ms. Pendy HO from UMF for their professional training in handling the characterization tools and their suggestions on my research work.

Finally, I want to express my gratitude to my family members. They gave me unconditional love and support. With that, I have the courage to pursue my dream and face the unknown world. Thanks also for the company all the time. And I would express my deep love to my grandpa. I want to tell him that I am living well in the world, not so satisfied, but bravely finding my future and happiness.

Table of Contents

List of Figures

List of Tables

Chapter 1 Introduction

1.1 Background

Nitrogen is one of the primary nutrients necessary for the existence of all life. It is required to form several biomolecules, including amino acids, DNA, and chlorophyll. Plants use nitrogen to produce the amino acids necessary to build plant tissue and proteins. Without proteins, plants wither and die. For human beings, each of us must eat ten essential amino acids to create the body proteins required for tissue growth and maintenance. Nitrogen is also a crucial component of the nucleic acid that produces DNA, a genetic material essential for transmitting certain characteristics and traits that promote survival. In addition, it helps maintain the genetic information in the nucleus of living organisms. Nitrogen is also a component of the chlorophyll molecule, which gives plants their green color and contributes to food production for the whole ecosystem through photosynthesis.

Although nitrogen is abundant in nature and 78% of our atmosphere is composed of nitrogen, almost all are in an unreactive form (gaseous nitrogen, N_2) that is not usable by most organisms, creating a shortage of nitrogen and often restricting primary production in many ecosystems. Only when nitrogen element is transformed from its unreactive form into the reactive form, such as ammonia or nitrate, can it be accessible to these organisms in the ecosystem (Figure 1.1). The process of transforming unreactive N_2 in the atmosphere into the reactive nitrogen is called nitrogen fixation. In nature, nitrogen fixation is mainly accomplished by the nitrogen-fixing bacteria, and a small amount of nitrogen is fixed during lightning. Only after the nitrogen fixation, can the unreactive N_2 in the atmosphere flow to plants. Then the plants could utilize the fixed nitrogen to produce more complex organic nitrogen, such as amino acids and nucleic acids. The organic nitrogen is then transferred up the food chain by eating other living organisms. Thus, to support more living organisms, including we human beings, it is imperative to fix more nitrogen from the atmosphere N_2.

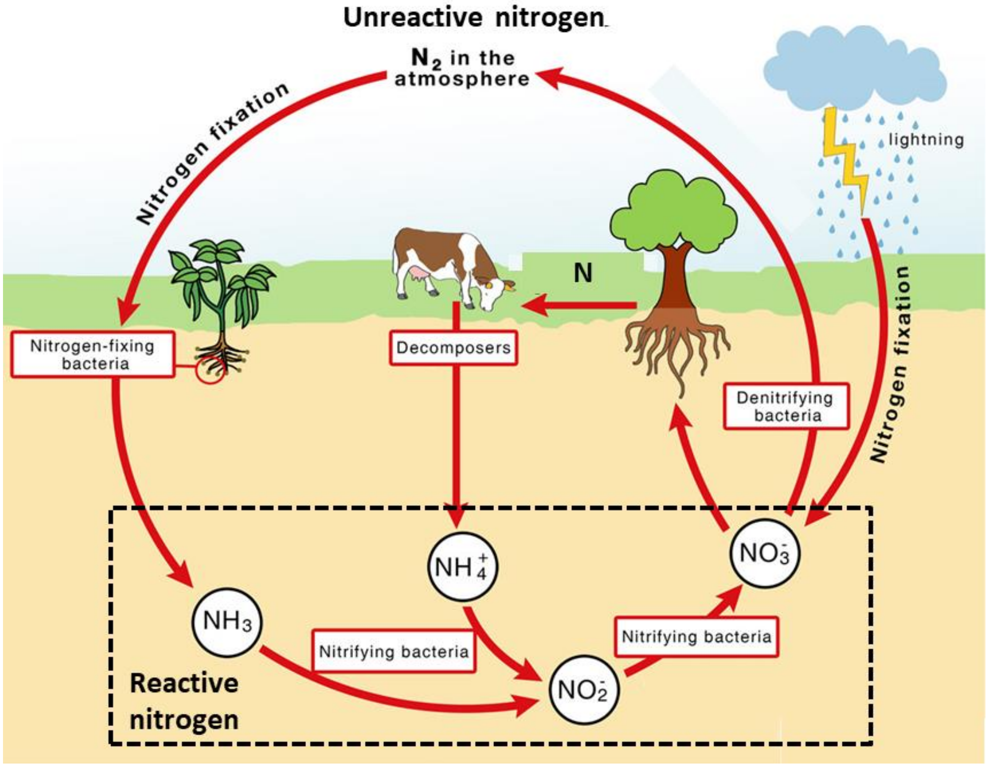

Figure 1.1 Schematic nitrogen cycle in nature.[1]

Before the early 1900s, fixed nitrogen came almost exclusively from microbes containing the enzyme nitrogenase through biological nitrogen fixation from dinitrogen (N_2) in the air. Without human intervention, the organic nitrogen supply in the environment is insufficient to sustain the current abundance of human life. This landscape changed in the early 1900s with the invention by Haber and Bosch of an industrial process to reduce N_2 to NH_3 (Eq. 1-1).[2, 3] This process has dramatically altered the possibilities for human society's evolution. By supplying additional NH_3 as fertilizer to agriculture, its development has addressed the most stressful concern at the start of the 20th century: the avoidance of global hunger.[4] As illustrated in Figure 1.2, since the Haber-Bosch process was invented, the global population has been increasing consistently with the increase of Harbor-Bosch nitrogen. It has been estimated that more than 50% of the nitrogen in each human body has been derived through this process.

It can be seen that after the 1940s, the world population grew at a higher rate because of the extensive use of the Haber-Bosch process (HBP). It is claimed that without the Haber-Bosch process, agricultural output would not have been able to feed the growing population in the world, making the manufacture of ammonia essential for human society.

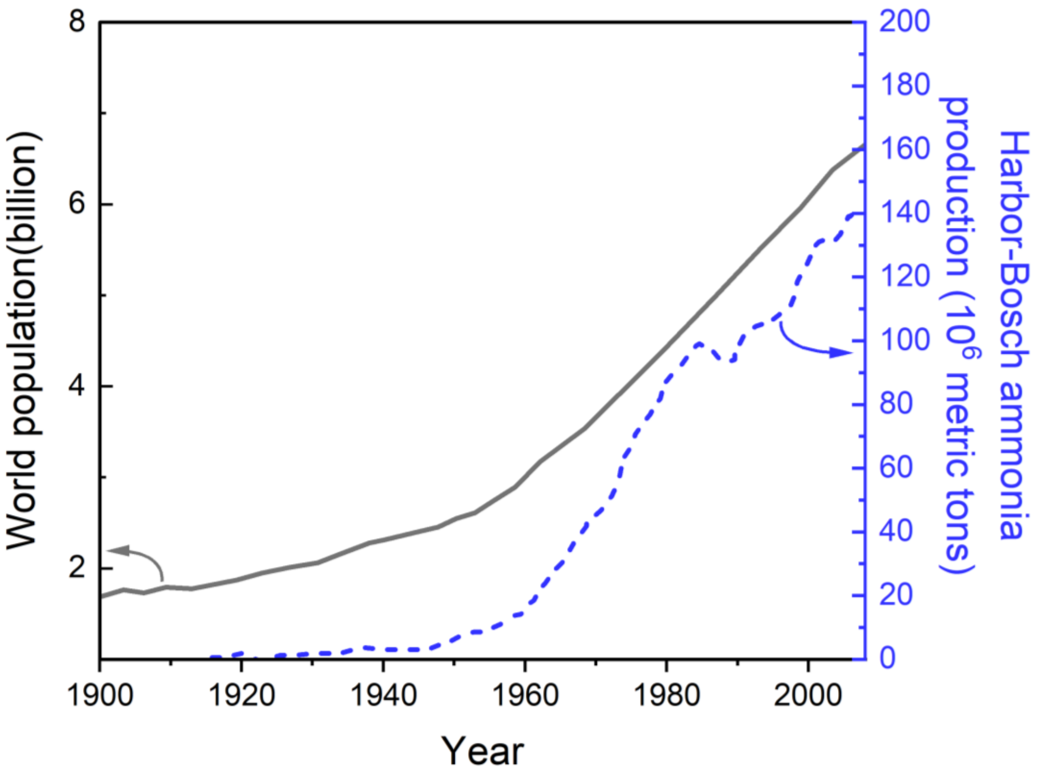

Figure 1.2 The relationship between the world population and ammonia production from the Haber-Bosch process. (Adapted with permission.[5] Copyright 2008, Springer Nature)

$$N_2 + 3H_2 \rightarrow 2NH_3 \qquad 1\text{-}1$$

Despite its outstanding achievements, the Haber-Bosch process has significant issues that indicate the need for an alternative ammonia production method. Industrially, in the Haber-Bosch process, nitrogen and hydrogen gas molecules are reacted under high temperatures (450-500 °C) and pressures (up to 20 MPa) to produce ammonia, according to Eq. 1-1. The solid and inert triple bond in dinitrogen (N_2) results in extremely high activation energy for the nitrogen-involved reaction.[6] To enable the reactions at appreciable rates, they are typically operated under harsh conditions. Such a reaction under harsh conditions is only cost-effective for large-scale production, which is also the reason why ammonia production is mostly centralized.[7, 8] Because of the high-cost and centralized nature of Haber-Bosch plants, many remote communities need to pay more for transportation to get access to ammonia fertilizers in other forms such as urea. Lack of fertilizers supplements possibly leads to decreased soil fertility, diminishing agricultural yields, and widespread food shortages, especially in places with deficient soil nitrogen.

The significant greenhouse gas emission is another concern. Extremely clean hydrogen gas (H_2) is required to produce ammonia without poisoning the catalysts.[9] Typically, as shown in Figure 1.3, the H_2 required for this process is supplied by steam-methane reforming and water-gas shift reactions using natural gas. (Eq. 1-2, 1-3). It can be calculated that the use of natural gas as the source of hydrogen generates at least 1.9 tons of carbon dioxide for production of every ton of NH_3. The annual global ammonia production in 2018 results in around 500 million tons of carbon dioxide emissions.[10, 11] As a result, the Haber-Bosch process accounts for around 1.8% of CO_2 emissions in the world in 2018.[12] Such a large amount of greenhouse gases emission will be directly responsible for global warming. Therefore, urgent demand emerges for the development of an alternative, sustainable technology for ammonia production that does not require harsh conditions.

$$\mathrm{CH_4 + H_2O \rightarrow CO + 3H_2} \qquad 1\text{-}2$$

$$\mathrm{CO + H_2O \rightarrow CO_2 + H_2} \qquad 1\text{-}3$$

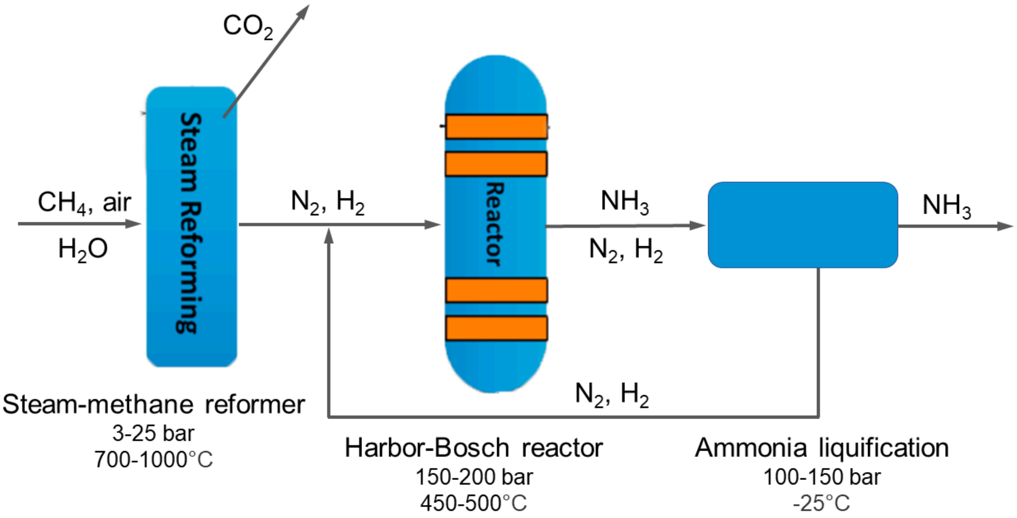

Figure 1.3 A simplified representation of ammonia production in the industry.

With decrease in renewable electricity prices, electrochemical synthesis of ammonia from N_2 and H_2O (Eq. 1-4) presents a desirable alternative to the HBP. As illustrated in

Figure 1.4, an ideal electrochemical process would consume nitrogen, even air as the nitrogen source, and water as the hydrogen source, driven by the electricity from renewable sources, such as solar or wind. Such a process could generate ammonia under ambient conditions, producing ammonia at the consumption site. Moreover, on-site ammonia production method avoids the dilemma that centralized manufacturing is currently absent in less developed countries or areas.[13, 14] Providing renewable electric energy as the power source and water as the hydrogen feedstock, the reaction can be proceeded without fossil fuel, thus, eliminating the release of CO_2 during ammonia production. Therefore, NH_3 could be produced in a sustainable pathway under ambient conditions.

$$2N_2 + 6H_2O \rightarrow 4NH_3 + 3O_2 \qquad 1\text{-}4$$

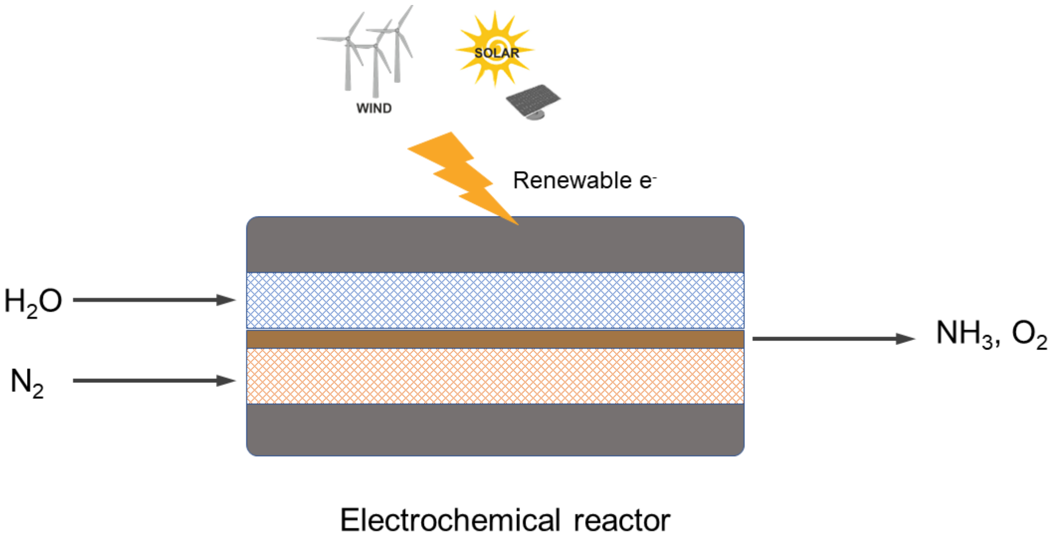

Figure 1.4 Electrochemical reactor for ammonia synthesis from N_2, water, and renewable electricity.

Although many ammonia electro-synthesis systems with various configurations and catalyst compositions have been proposed,[15] many of them report Faradaic efficiencies (FE) (i.e., selectivity) and production rates too low for practical utilization. Ideally, the electrochemical process enables the direct electrons and protons addition to the nitrogen molecules. Thus, the electrons from the electricity supply can be fully utilized to convert N_2 to NH_3 through nitrogen reduction reaction (NRR). However, as illustrated in Figure 1.5, the intended splitting of the strong triple bonds of N_2 is too sluggish compared to the parasite combination of electrons and protons, that is, hydrogen evolution reaction (HER), resulting in a low FE in electron utilization (usually lower than 5%).[16] Consequently, the final production of NH_3, ranging from the PPB to the PPM level, is too low to be distinguished from the environmental contaminant.

The value of FE is essential in ammonia production by the electrochemical method. It represents the ratio of effective electrons utilized for ammonia production over the total amount of electrons supplied. A high value of FE is expected to efficiently produce ammonia with the electron supply, especially for the on-site ammonia production with the electrons directly supported by renewable energy. Thus, for the electrochemical method, it is desirable to reach a high FE towards ammonia and reliable production for effective NH_3 electro-synthesis from N_2 and H_2O.

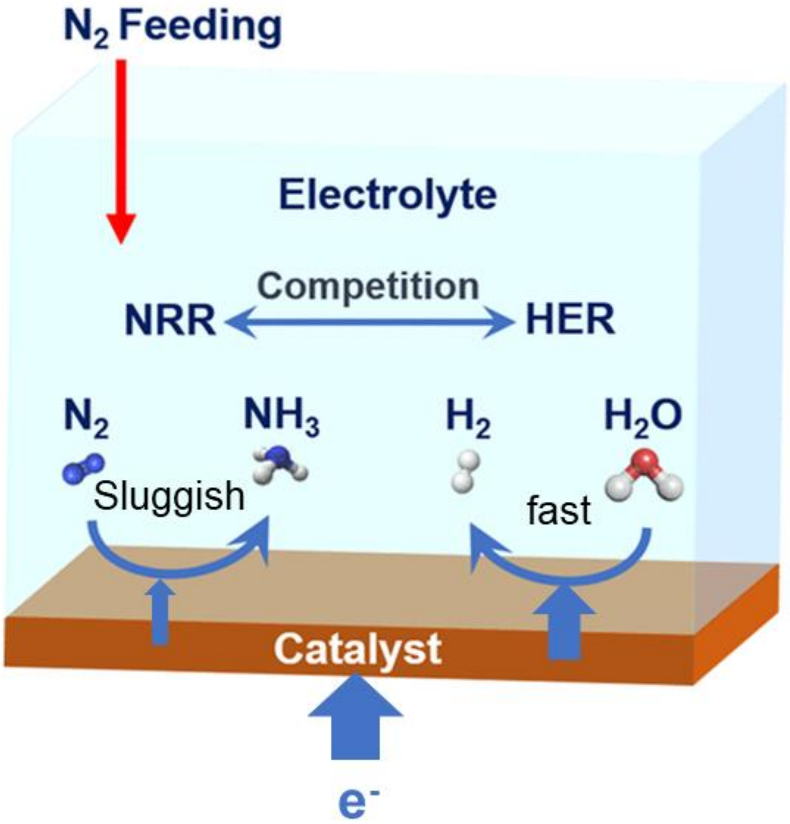

Figure 1.5 Schematic illustration of the electrocatalytic interface for electrochemical ammonia synthesis from N_2 and water. (Reproduced with permission.[17] Copyright 2020, American Chemical Society)

Among reported electrochemical approaches for NH_3 synthesis from H_2O and N_2, methods that use lithium metal as a mediator report some of the highest Faradaic efficiencies and absolute production rates, as well as strict and reproducible controls.[18] Because of the negative potential of Li^+/Li (-3.04 V vs. SHE), metallic Li can easily open the stubborn triple bonds in the nitrogen molecules, even under ambient temperature.[19] In lithium-mediated nitrogen reduction (Figure 1.6),[20] ideally, lithium metal could be obtained by electrochemical reduction of Li-ions (Li^+) (Eq. 1-5). Then Li can easily react with the nitrogen molecules under ambient conditions through a known reaction (Eq. 1-6), forming lithium nitride, Li_3N. Lithium nitride is a reactive alkaline that violently reacts with water to form ammonia, (Eq. 1-7). After ammonia production, the LiOH could be recovered and once again be reduced to lithium metal for the next cycle. Each step in the Li-mediated ammonia synthesis is shown as follows:

Li plating $$4\mathrm{LiOH} + \mathrm{e}^- \longrightarrow 4\mathrm{Li}^0 + 2\mathrm{H_2O} + \mathrm{O_2}\uparrow \tag{1-5}$$

Nitridation $$6\mathrm{Li} + \mathrm{N_2} \longrightarrow 2\mathrm{Li_3N} \tag{1-6}$$

Hydrolysis $$2\mathrm{Li_3N} + 6\mathrm{H_2O} \longrightarrow 2\mathrm{NH_3} + 6\mathrm{LiOH} \tag{1-7}$$

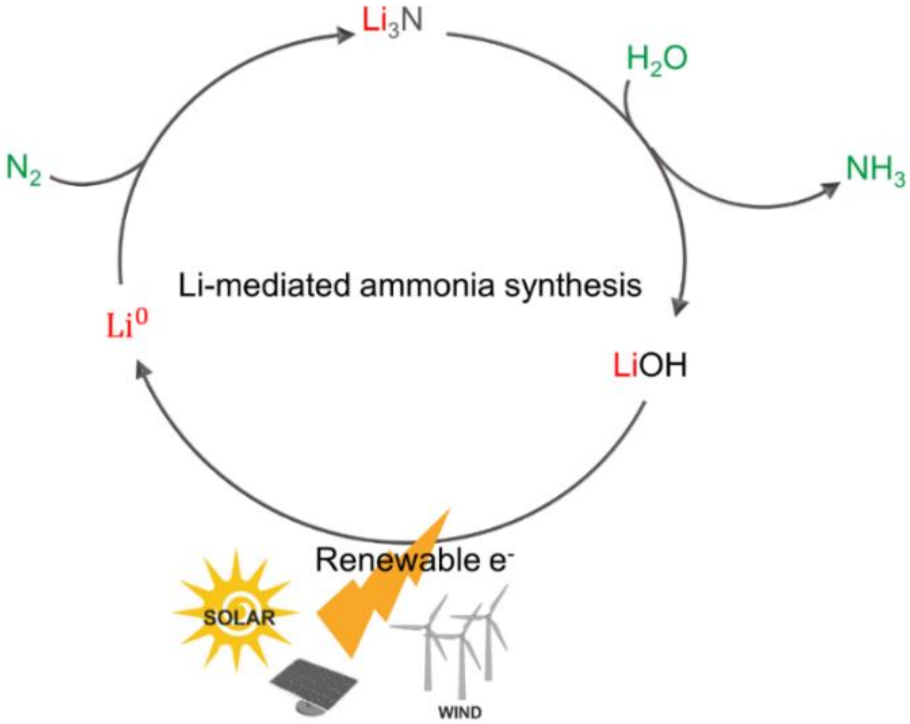

Figure 1.6 Schematic illustration of sustainable Li-mediated ammonia synthesis from N_2 and H_2O under ambient conditions.

Unlike direct electrochemical ammonia production, the Li-mediated pathway can produce ammonia by the cycles of three individual steps. Li only serves as the mediator in the cycles and theoretically can be reused for the following cycles. Furthermore, in each Li-mediated cycle, only N_2 and H_2O will be converted to NH_3 with O_2 released. For cheap and efficient ammonia production, it is expected that the efficiency in each cycle should be as high as possible, and the stepwise Li-mediated pathway can be operated as many cycles as possible. And it has been reported that the efficiency of nitration and hydrolysis is equal to 100 %. Thus, it is required to plate Li from LiOH efficiently in each cycle, and the Li plating setup can be operated stably in multiple cycles. Consequently, for cheap and efficient ammonia production under ambient conditions, a stable and an efficient method for Li plating is urgently required.

Previous research has built up the Li plating method by the electrolysis of molten LiOH to provide a reactive Li surface, obtaining a high FE towards NH_3, as demonstrated in Figure 1.7a. However, such a high temperature is unsuitable for the ammonia electro-synthesis under ambient conditions. Others reported that it is possible to plate Li in a less reactive organic electrolyte by separating the Li plating from the Li salt solution (Figure 1.7b).[21] Even though it can obtain Li metal under ambient conditions, its practical application is hampered by the costly LISICON, and it is questionable about its chemical stability, especially under long-term operation. Thus, exploring a stable and efficient method to continuously plate metallic Li for the Li-mediated pathway under ambient conditions is expected.

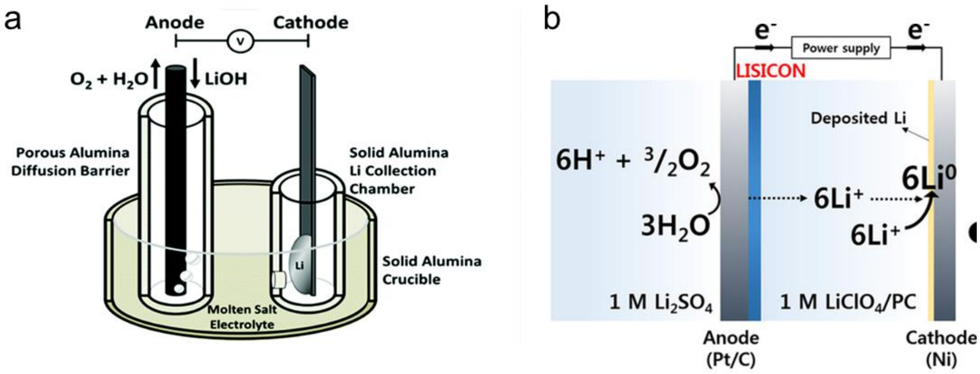

Figure 1.7 Metallic Li plating strategies (a) Li plating by the electrolysis of molten LiOH under 450 °C, and b) Li plating from the aqueous Li-containing solution by separated with LISICON membrane under ambient conditions. (a) Reproduced with permission from. Copyright 2017, Royal Society of Chemistry. (b) Reproduced with permission. Copyright 2017, Wiley.

1.2 Research objectives

The objectives of the present study therefore are:

1. To explore feasible method to efficiently plate Li metal from LiOH solution.
2. To establish the critical parameters for ammonia production based on the Li-mediated method.
3. To create the essential engineering knowledge for the Li-mediated ammonia synthesis process.

Chapter 2 Literature Review

2.1 Introduction

In this chapter, both conventional and emerging methods of ammonia synthesis methods will be reviewed, beginning with the industrial Haber-Bosch process, followed by the emerging photochemical and electrochemical ammonia synthesis methods. Li-mediated ammonia synthesis, a branch of the electrochemical approach, is considered as one of the most promising alternatives to the commercial HBP method because lithium metal can readily break the stubborn N≡N bond under ambient conditions.

2.2 Conventional method of ammonia synthesis

The conventional industrial process for ammonia synthesis inclusively consists of hydrogen feedstock production from Stream methane reforming (SMR) and the Harbor-Bosch process. After producing H_2, the N_2 would be separated from the air by secondary steam reforming or separation of air. After that, ammonia would be fabricated using the Haber-Bosch process from N_2 and H_2. To facilitate the process, high pressure (20-30 MPa) was implemented to improve its production rate, and high temperature (400-450 ºC) would be supplied to favor the reaction kinetics. The reaction is typically catalyzed by metallic iron. The process is demonstrated in Figure 2.1.[22]

2.2.1 Stream methane reforming (SMR)

Industrial ammonia synthesis has deleterious effects on the environment because it is fossil-fuel dependent and energy intensive. Typically, cryogenic techniques are necessary to extract N_2 feedstock from the atmosphere[23]. H_2 is generated by highly endothermic processes from fossil fuels such as natural gas, coal, and petroleum, while exothermic reactions produce CO_2. Natural gas is the primary source of H_2 for ammonia production, comprising 72% of the amount.[24] The production of H_2 from natural gas involves desulfurization, steam reformation, and the water-gas shift reaction, as shown in the following equations.[25, 26]

Steam reformation:

$$\mathrm{CH_4 + H_2O \rightarrow CO + 3H_2, \Delta H_{298K} = +206\ kJ\ mol^{-1}} \qquad 2\text{-}1$$

Water-gas shift reaction

$$\mathrm{CO + H_2O \rightarrow CO_2 + H_2, \Delta H_{298K} = -41.1\ kJ\ mol^{-1}} \qquad 2\text{-}2$$

Steam reformation is a highly endothermic and energy-intensive process. Along with the cost of natural gas, the creation of hydrogen accounts for roughly 75% of the operating expenses associated with ammonia manufacturing.[27] The remaining 25% is allocated to gas compression, ammonia synthesis, and separation processes. It was calculated that industrial ammonia synthesis utilizes 3 to 5% of the world's natural gas output and produces more than 300 million metric tons of CO_2 annually, of which two-thirds are derived from the generation of H_2 from natural gas.

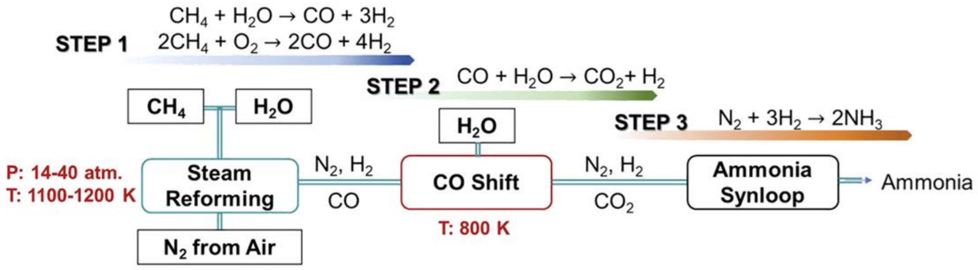

Figure 2.1 Ammonia production through the Haber-Bosch process. (Reproduced with permission.[28] Copyright 2021, American Chemical Society)

2.2.2 Haber-Bosch Reaction

In the Haber-Bosch process, N_2 and H_2 are run through ruthenium- or iron-containing catalysts at high temperatures (450-500 °C) and pressures (up to 20 MPa) to generate ammonia by Eq. 1-1 with the reaction enthalpy , ΔH_{298K} being $-92\ \mathrm{kJ\ mol^{-1}\ N_2}$[29, 30] This process is exothermic, and according to Le Chatelier's principle, low temperatures promote the formation of ammonia. However, the kinetic barrier for breaking the strong N≡N connection is considerable. High temperature is required to break it at sufficient rates.[31] Furthermore, according to the equilibrium calculations, under temperatures over 400 °C and 0.1 MPa, ammonia decomposes to N_2 and H_2. [32] Therefore, to force the equilibrium of Eq. 1-1 toward the formation of ammonia, the Haber-Bosch synthesis of ammonia is usually undertaken at high pressures ranging from 20 to 40 MPa. Although only 15% conversion to ammonia is achieved in a single reaction, the unreacted N_2 and H_2 will be cycled back to the reactor, enabling total yields of around 97%.

2.2.2.1 Thermodynamic equilibrium

Understanding the thermodynamic equilibrium of the ammonia synthesis process is crucial for determining the possible maximum ammonia production of a catalyst under certain circumstances. In 1906, Fritz Haber computed the equilibrium production of ammonia from nitrogen and hydrogen at temperatures ranging from 200 to 1000°C and pressures of 0.1, 3, 10, and 20 MPa.[33] The thermodynamic equilibrium data calculated from Gillespie and Beatties's [33]study and published by Max Appl[34] are shown in Figure 2.2.

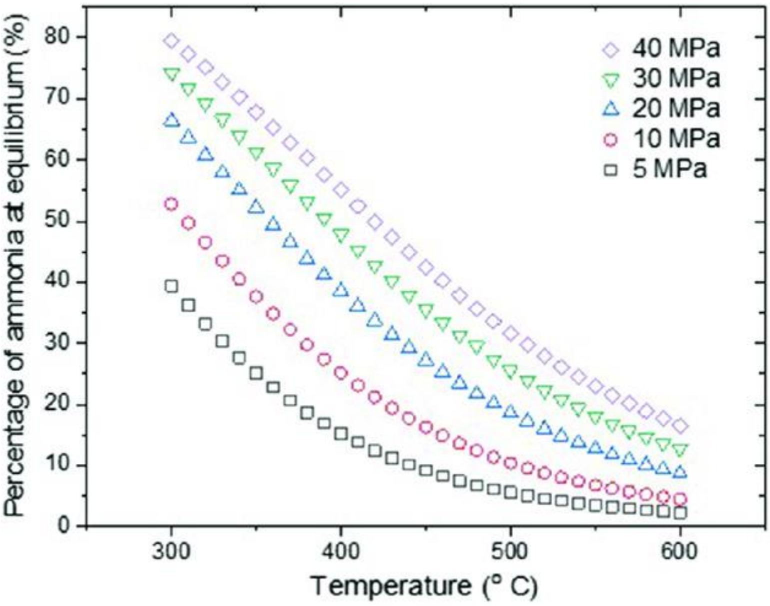

Figure 2.2 The influence of temperature and pressure on the reaction equilibrium of ammonia production. (Reproduced with permission,[26] Copyright 2002, Wiley)

This enables us to establish under what circumstances the theoretical maximum ammonia yield could be achieved. Due to the yield restriction imposed by thermodynamic equilibrium, the goal of any catalyst for ammonia synthesis should be to obtain its highest yield at low temperatures. As stated before, the reaction rate at low temperatures is too sluggish to synthesize ammonia, despite the enormous equilibrium limit, which approaches 100% conversion. It is reported that the majority of current ammonia synthesis catalysts used in the Haber-Bosch process produce a conversion rate of between 10 and 15% while working at temperatures between 425 and 450°C and pressures over 10 MPa.[35]

2.2.2.2 Reaction mechanisms

In the last century, the reaction mechanisms for synthesizing ammonia from H_2 and N_2 over an industrial iron catalyst have been heated in discussion. [36-38] Only in the late 1970s Ertl et al. [36] were able to develop a free energy diagram for gas phase ammonia synthesis and ammonia synthesis over an industrial iron catalyst. Table 2-1 details the chemical pathway to produce ammonia, where the asterisk (*) represents a surface site of the catalyst.

Table 2-1 Ammonia synthesis mechanism of the Harbor-Bosch reaction based on the industrial iron catalyst

	Reaction	**Note**
H_2 dissociation	$H_2 + 2* \rightleftharpoons 2H*$	
N_2 dissociation	$N_2 + 2* \rightleftharpoons 2N*$	Rate-determining step
Hydrogenation reactions	$N* + H* \rightleftharpoons NH* + *$	
	$NH* + H* \rightleftharpoons NH_2* + *$	
	$NH2* + H* \rightleftharpoons NH_3* + *$	
NH_3 desorption	$NH_3* \rightleftharpoons NH_3 + *$	

In the 1910s, Mittasch *et al.*[39] exerted much effort in searching for an appropriate catalyst for synthesizing ammonia by examining most periodic table elements and their combinations. It was not until decades later that the binding strength of nitrogen on the reaction surface was shown as an indicator of ammonia production activity.[40] Based on the theory of binding strength, the so-called volcano curves were built up by using the binding energy to nitrogen to describe the ammonia synthesis activity (Figure 2.3a).

It has been widely accepted that the ammonia synthesis activity is directly related to the nitrogen adsorption energy on the surface of catalysts, which is described by the volcano curves. As demonstrated in Figure 2.3a, observed from each side of the plot, some metal catalysts have a higher N binding adsorption energy. Thus, N could bind the catalyst surface strongly. Whereas other catalysts with a smaller value could bind the nitrogen too weakly.[41] For those catalysts with considerable adsorption energy, they easily bind the N_2 molecules. However, after the N≡N, the nitrogen species should leave the catalyst's surface for ammonia formation. Generally, it is not easy for catalysts with high binding energy for the nitrogen species to leave after the reaction. Thus, the limited number of active sites could be the limiting factor for its activity. Therefore, an excellent catalyst must bind nitrogen not so strongly and also not so weakly. That is also why the catalyst with medium binding energy could deliver a peak ammonia synthesis activity in the volcano plot.

According to the volcano-type relationship, the catalysts with medium binding adsorption energy could be suitable for the HBP. Based on the theory, new strategies to explore catalysts were proposed by choosing the catalysts from the two sides of the volcano, forming a new form of alloy catalyst, such as CoMo.[42] The alloy could deliver improved ammonia production activity through this strategy. Despite this, the industrial application of these improved catalysts is still limited by the high cost compared to cheap iron catalysts, especially in large-scale production.

Although plenty of progress has been made, the scaling relationship still hampered the exploration of more active catalysts.[43, 44] As illustrated in Figure 2.3b, the activation barrier for N≡N dissociation is scaling with the desorption energy of the intermediates since they share the same intrinsic bonding properties. Consequently, it is difficult to find a new and highly active catalyst stabilizing the transition state of N_2 dissociation and, meanwhile, having a weak affinity for NH_x (x=0,1,2) intermediates for the following steps. As a result, to further improve the catalysis effects, efforts can also be made to explore new processes or systems that break the scaling relationship and realize ammonia synthesis from nitrogen with high efficiency and production rate under ambient conditions.

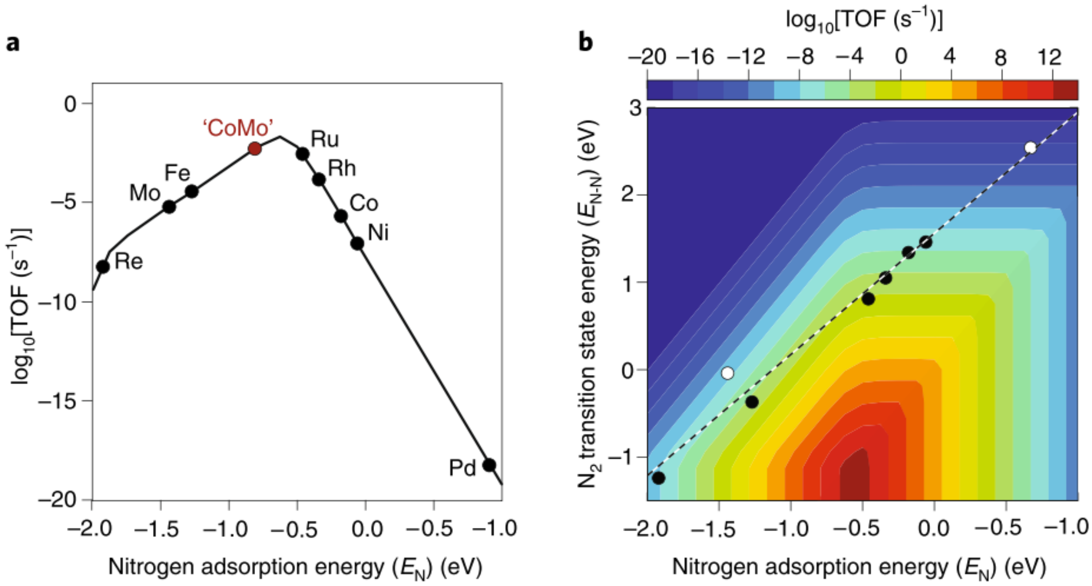

Figure 2.3 Theoretical predictions based on computation for heterogeneous catalysts. [45] a) Volcano diagram for ammonia production on the surface of transition metals catalysts b) Typical scaling relation for the N_2 dissociation versus the transition state intermediate on the transition state metals.(Reproduced with permission.[45] Copyright 2015 Elsevier)

2.2.3 Challenges and Opportunities

Significant improvement has been made in the past century, including improving the energy balance of ammonia synthesis and optimizing its industrial plants. However, exploring a new ammonia synthesis catalyst with excellent catalyzing activation and acceptable expense is still challenging when considering large-scale ammonia production. Possibly, there may remain the reaction pathway to break the scaling relationship. That is, the N_2 dissociation is decoupled from its intermediated products in the Harbor-Bosch process. Such a strategy could bring us a promising pathway to deliver an appreciable ammonia production rate while operating under lower temperatures and pressure, contributing to a portion of the significant expense in industrial production. If such catalysts or pathways could be achieved, harsh conditions would no longer be required. The massive energy consumption for the process and the capital cost of the ammonia plant would be reduced significantly.[46]

2.3 Emerging methods of ammonia synthesis

2.3.1 Photochemical methods of synthesizing ammonia

2.3.1.1 General description

The photochemical synthesizing of ammonia has been a promising alternative for sustainable ammonia production. The process is driven by sunlight. The advantage of the photochemical process is that the energy for the process is derived directly from sunlight, using sustainable feedstocks such as water and air. Photochemical synthesis is a viable contender for decentralized, off-grid ammonia production since energy was not supplied from the electric network, unlike the electrochemical approach. One disadvantage of photochemical reactions is that they are only operated when the sun is shining.

Photochemical ammonia synthesis is similar to other photochemical processes, such as H_2 production and CO_2 reduction. The process can be separated into three fundamental steps (Figure 2.4):

1. Under the illumination of sunlight, the semiconductor will be excited by the photon, and the electrons receive the energy of the photons in the valance band (VB), get excited by jumping into the conduction band (CB) of the semiconductor. Meanwhile, the holes are generated in the VB because of the leave of electrons. There remains some possibility for the induced electrons and the holes to recombine and disappear.
2. The electrons jumped into the CB would move to the active site to reduce the reactant, and thus the photochemical reaction happens. For the photochemical ammonia synthesis, the N_2 molecules, bound on the catalyst surface, can accept the electron to produce ammonia.
3. Meanwhile, the hole created in the VB would react with the reactant to oxide it. For a charge balance, the H_2O will receive the holes and be oxidized to O_2 in the photochemical process.

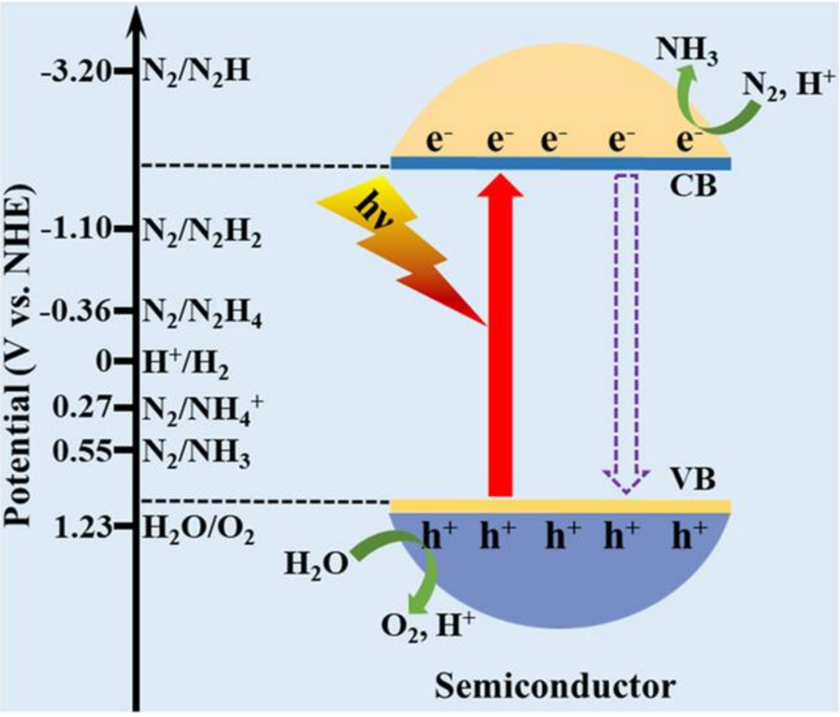

Figure 2.4 Schematic illustration of photochemical reaction and the equilibrium potential (vs. NHE) of several typical reactions related to N_2, assuming the pH in the solution equals 0. (Reproduced with permission.[47] Copyright 2020, Wiley).

In a typical photochemical process for ammonia synthesis, the reaction occurs when the N_2 molecules accept the photo-induced electrons to produce NH_3. To improve ammonia production, some sacrificial reagents, such as water, will be used to consume the holes and prevent their accumulation. In this way, ammonia production can be improved. In theory, many reductive chemicals, including ethanol, methanol, Na_2SO_3, etc., can be used as the sacrificial reagents.[48, 49] Considering the potential interference in detecting the produced NH_3, the reagents should be well selected. There is no doubt that water could be an ideal sacrificial regent considering its no interface to NH_3 detection and its sustainable nature.

In the photochemical process, the whole reaction for ammonia involved two half redox reactions and six electrons, six holes, and six photons. Thus, the reactions in the process are a little complicated with different equilibrium reaction potentials as follows:

$$N_2 + 6H^+ + 6e^- \rightarrow 2NH_3, E^0_{NHE} = 0.55V \qquad 2\text{-}3$$

$$3H_2O + 6h^+ \rightarrow 6H^+ + \frac{3}{2}O_2, E^0_{NHE} = 1.23V \qquad 2\text{-}4$$

Overall reactions: $N_2 + 3H_2O \rightarrow 2NH_3 + \frac{3}{2}O_2, \Delta G^0 = 7.03\ \text{eV}$ 2-5

It has been known that the photochemical reaction is heavily dependent on the energy band structure of the photocatalyst, as well as the reaction potential of reactants. Ideally, the electrons are expected to flow to the N_2 reduction for NH_3. Thus, the CB of the catalysts should be negative for the reaction potential of N_2 reduction. Meanwhile, the energy level of VB should be more positive than the potential of oxygen evolution reaction (OER) for consuming holes. As demonstrated in Figure 2.4, the equilibrium potential of nitrogen reduction for NH_3 is 0.55 V or for NH_4^+ is 0.27 V, both of which are more positive than the HER. Thus, comparable to the HER, the NH_3 formation is more thermodynamically favorable to happen (Figure 2.4). However, because HER is a 2-electron reaction and the NH_3 formation is a 6-electron reaction, the HER is more kinetically beneficial compared to NH_3 formation. Furthermore, due to the energy required to split the stubborn nitrogen bonding, high potential is usually required. For example, for the first photo-induced electron transfer process (PCET), $\mathrm{N_2 + H^+ + e^- \rightarrow N_2H}$, a reduction potential of -3.2 (vs. NHE) is necessary. It is a significant challenge to lower the energy barrier for the photocatalyst with an effective active site.

2.3.1.2 Mechanisms of photocatalytic ammonia synthesis

In general, the photocatalytic processes of NRR may be classified as either dissociative or associative, as shown in Figure 2.5.[50-52]. The dissociative mechanism relates to splitting the N≡N in dinitrogen, followed by the production of NH_3 by hydrogenation. The dissociative mechanism includes splitting the N≡N and H-H bonds, followed by the direct reaction of N and H atoms. Since sunlight cannot generate the enormous energy to break down N_2 molecule, all photochemical ammonia production systems were proceeding with the associative mechanism. Typically, the photochemical method of synthesizing ammonia is comprised of three steps, including:

1. Nitrogen molecules are absorbed on the surface of catalysts at the active sites.
2. Through the PCET process, electrons, and photons flow to the N_2 and split the triple nitrogen bonds.
3. After ammonia formation, the NH_3 molecules will be desorbed and leave the active sites.[53]

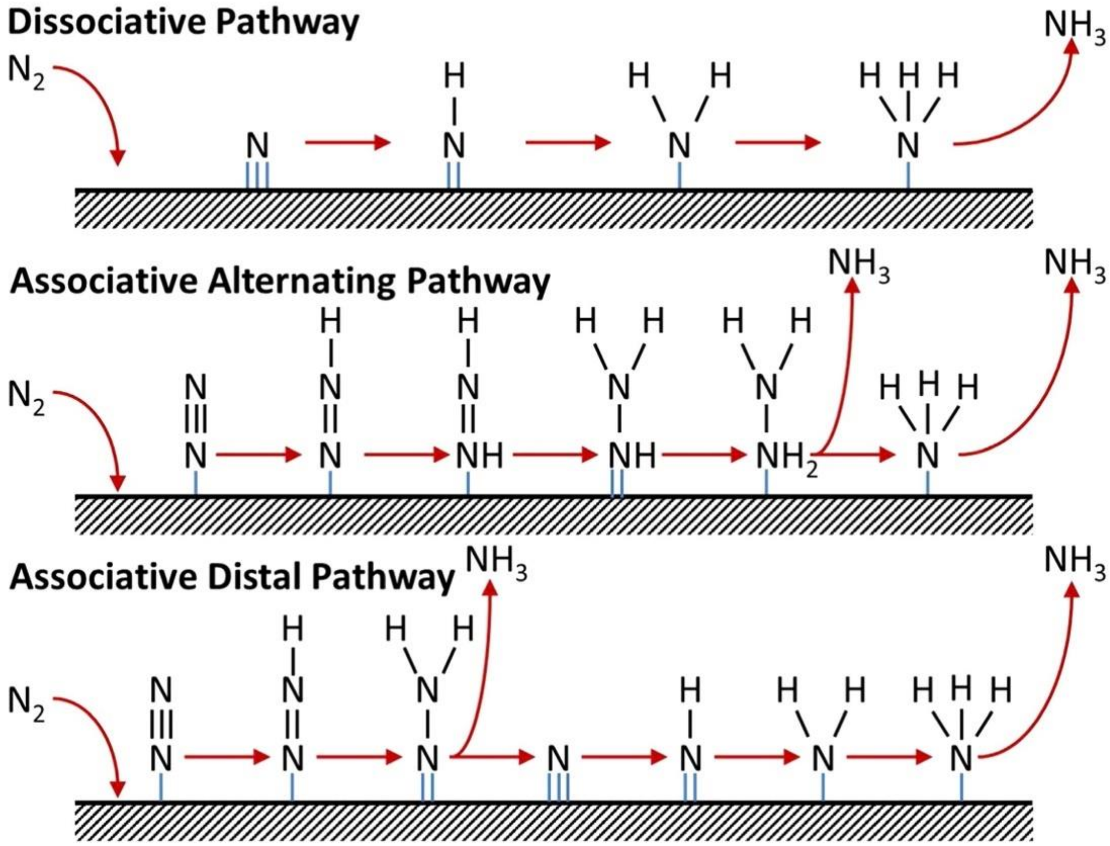

Figure 2.5 Schematic representations of the conventionally recognized routes of nitrogen reduction to ammonia. (Reproduced with permission.[54] Copyright 2016, Elsevier)

2.3.1.3 Photocatalytic systems

According to the existing photocatalyst modes in the photochemical process, the advanced and developed photochemical ammonia production systems can be divided into two basic categories: (1) photocatalyst suspensions, which include two-phase or three-phase photo-reaction systems, and (2) photocatalyst films, which include single-chamber and dual-chamber photoelectrochemical cells.

a) Two-phase suspension photochemical system

As depicted in Figure 2.6a, in the two-phase suspension photochemical system, the photocatalysts suspension is dispersed uniformly in the water solution, possibly with the sacrificial reagent. N_2 is introduced into the solution till its saturation. Such a system is mostly used in photochemical ammonia production. However, the limited N_2 solubility in the water (~1.0 mmol L^{-1} at 25 °C, 0.1 MPa) will influence the supply of N_2 for the reaction by the limited mass transfer. When the N_2 reduction is not beneficial to accept the electrons, the parasites' reaction, HER, would be dominant, thus leading to low electron utilization towards ammonia. Moreover, the oxygen molecule in the feedstocks may oxide the NH_3 products and further decrease the selectivity of ammonia.

b) Three-phase system

To improve the mass transfer and avoid the oxidation of NH_3 products, a three-phase system was designed in the field of photochemical ammonia production.[56] In the system, photocatalyst suspensions are distributed in the gas and liquid phases interface, Figure 2.6b. Since the N_2 concentration in the gas is far higher than in the water saturated with N_2 (at the value of ~140 times), the photochemical reaction in the three-phase system is much faster than in the two-phase system. Thus, the performance of NH_3 production is largely improved.[46] O_2 is separated from the NH_3 by distributing them on the different sides of the photocatalyst. Thus, the parasite oxidation reaction could be avoided. For this reason, the air can directly provide N_2 for the system instead of pure nitrogen, significantly decreasing the cost of the system and facilitating its industrialization.[56]

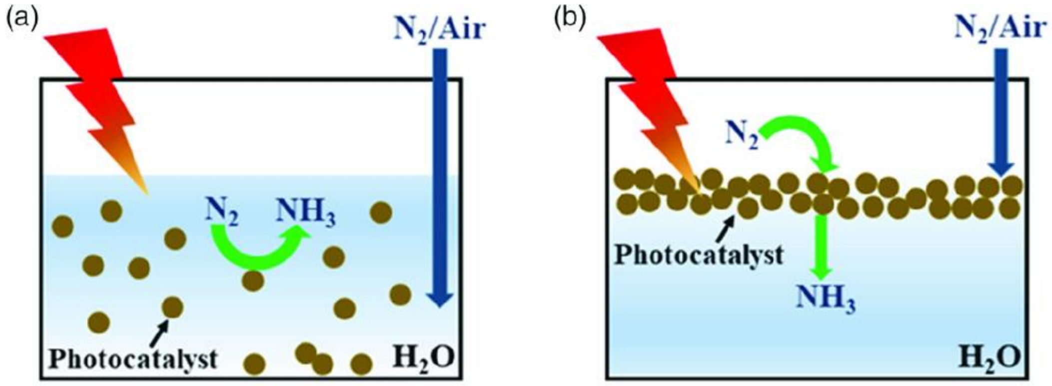

Figure 2.6 Diagrams of the a) two-phase and b) three-phase photocatalyst suspension systems. (Reproduced with permission.[55] Copyright 2020, Wiley)

2.3.1.4 Photocatalyst films

An apparent issue related to the suspension system is the challenge and high expense of separating the photocatalysts from the solution. For easy recycling, the photocatalysts are fabricated into a conductive film. Such a structure is beneficial in separating and recovering. Typically, the film serves as the cathode in the photoelectrochemical ammonia production system, including single-chamber and dual-chamber cells. Besides the light-driven reaction, external electric energy could also be applied to accelerate the reaction. A typical photoelectrochemical system consists of a reaction cell, a light source, a three-electrode system with a working electrode (WE), a counter electrode (CE), and a reference electrode (RE).[56] During operation, the applied electric bias facilitates the photo-electrons to move towards the WE to generate NH_3, and the holes are trapped in the CE to produce O_2. Such a design can efficiently avoid the recombination of electrons and holes, thus significantly improving the ammonia production efficiency.[56]

Photocatalysts are the primary components of a light-driven nitrogen-fixation system. Thus, it is essential to rationally design and manufacture photocatalysts and reaction systems. However, most conventional single semiconductors are either incapable of meeting the criteria of photochemical ammonia production or are very inefficient. Several efforts have been made to enhance the ammonia synthesis processes, such as the selection and modification of semiconductors, including doping, vacancy introduction, cocatalyst support, morphological control, and heterojunction formation. Table 2-2 provides a summary of the reported ammonia production performance based on various photocatalysts. Different ammonia synthesis photocatalysts may be classified according to their elemental compositions: TiO_2 and other metal oxides, bismuth oxyhalides, metal sulfides, biomimetic materials, graphitic nitride carbon, as well as the corresponding composites or heterojunctions.

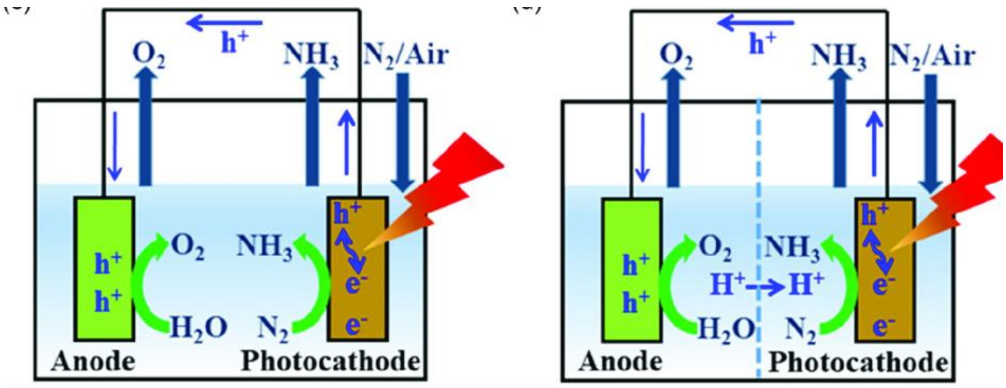

Figure 2.7 Illustration of the photocatalyst film system from photochemical ammonia production. (a) the single-chamber system, and (b) the dual-chamber system. (Reproduced with permission.[55] Copyright 2020, Wiley)

Table 2-2 A summary of the reported photocatalysts for ammonia production under ambient conditions.[55]

Photocatalyst	light source, scavenger	Measurement method	NH_3 yield [μmol g^{-1} h^{-1}]	AQE (or QE) [%]
Fe-doped TiO_2	254 nm, ethanol	Nessler’s reagent	400.0	0.18 m^{-2} (QE)
Gd-IHEP-8	UV-vis, -	IC	220	2.25 at 365 nm
0.5%-ZnAl-LDH	UV-vis, –	IC	110	1.77 at 265 nm
Bi_5O_7I-001	≥280 nm, methanol	Nessler's reagent	223.0	5.10 at 365 nm
Bi_5O_7I-100	≥280 nm, methanol	Nessler's reagent	95.2	2.30 at 365 nm
Fe single-atom/C-PPh_3/NaI	UV-vis, –	Indophenol blue	98.0	0.06 at 375 nm
BiOBr-001-OVs	UV-vis, -	Nessler's reagent	223.3	0.23 at 420 nm
BiOCl NS-Fe-5%	UV-vis, -	Indophenol blue	1022	1.80 at 420 nm
H-BiOBr	UV-vis, -	Nessler's reagent	499.8	2.10 at 380 nm
1% Mo-$W_{18}O_{49}$ nanowires	UV-vis, Na_2SO_3	IC, Nessler’s reagent	195.5	0.70 at 350 nm
6% Cu-ultrathin TiO2	UV-vis, -	Nessler’s reagent, IC	78.9	0.74 at 380 nm
TiO2/Au/a-TiO_2	UV-vis, -	Indophenol blue	13.4	4.9×10^{-3} at 254 nm
Defective $Bi_2O_2CO_3$	UV-vis, methanol	Nessler’s reagent	398.7	1.05 at 420 nm
Pt-loaded ZnO	UV, EDTA-2Na	Indophenol blue	860	-
TiO_2 (rutile); TiO_2 (P25)	≥280 nm, 2-propanol	IC	3.80; 2.96	0.70 at $\lambda < 350$ nm
TiO_2 (rutile); TiO_2/0.2 wt% Fe_2O_3	390-420 nm, -	Kruse-Mellon colorimetry	4.17; 11.5	-
P-doped CN-V	≥420 nm, -	IC	1.88	~1 at 420 nm
$Ni_2P/Cd_{0.5}Zn_{0.5}S$	≥400 nm, -	Nessler’s reagent	253.8	4.3 at 420 nm
$Zn_{0.1}Sn_{0.1}Cd_{0.8}S$	400-800 nm, ethanol	Nessler's reagent	131.9	-
α-Fe_2O_3/Fe-doped $SrTiO_3$	UV-vis, -	Nessler's reagent	30.1	-

(IC: Ion Chromatography)

In photocatalytic ammonia synthesis, this value of apparent quantum efficiency (AQE) or quantum efficiency (QE) stands for the N_2-fixation efficiency. It is defined as the ratio of photoelectrons towards ammonia production over the theatrical amount of incident photons under the light source with given wavelength. (Eq. 2-6). The value can be expressed as the product of the efficiencies during light absorption, charge separation, and photoelectrons-involved redox reaction. Besides, AQE or QE also can reflect the energy conversion efficiency of the photocatalysts towards ammonia at a specific monochromatic light wavelength. As shown in Table 2-2, most of the photocatalysts were tests under the light sources with the wavelength near the one of ultraviolet light (UV, <400nm), and even with such high energy light source, nearly all the photocatalysts can only deliver a small AQE (or QE) less than 5%. Some of them even only give out a value smaller than 1%. Such small AQE or QE values means the low utilization of the light towards ammonia. Considering the target of photocatalytic process utilizing sunlight as the light source, instead of UV, the AQE (or QE) value could be even smaller than the reports. Thus, effective photocatalysts still need to be explored for further improving the photocatalytic ammonia synthesis.

$$\mathrm{AQE}\ (\%) = \frac{\text{number of reacted electrons}}{\text{number of incident photos}} \times 100 \qquad 2\text{-}6$$

2.3.1.5 Challenges and opportunities

There remain some challenges in the field of photochemical ammonia production. The first one is the light source. Most current research on photochemical ammonia production relies on the UV as the light source to provide enough energy to split N≡N bonds. Such a requirement will limit its practical application for ammonia production. Furthermore, the production of the photochemical method is usually low, which is usually 3-5 orders of magnitude lower than the electrochemical one. Control experiments should be carefully taken to prove the effective ammonia production from the photochemical system due to a large amount of NH_3 from contamination or some other sources.

2.3.2 Electrochemical method of ammonia synthesis

Recent interest in electrochemical conversions has increased significantly due to the development of low-cost, renewable electricity. For this reason, the electrochemical method of synthesizing ammonia is globally studied. Compared to the conventional HBP, the electrochemical method has obvious advantages. Firstly, the electrochemical setup is much simpler than the HBP, with only an electrochemical unit. Moreover, it is possible to bypass the unsustainable hydrogen feedstocks by using water oxidation as the counter electrode, directly using the proton in the water for ammonia synthesis.

Depending on the cell design (material composition, physical state) and operating circumstances, many pathways exist for performing the electrochemical synthesis of ammonia (temperature, pressure). Typically, the process is divided into three primary categories based on the type of electrolytes employed, namely solid oxide electrolytes, molten salt electrolytes, and liquid electrolytes, or classified by the operating temperature, including the high temperature (500-800°C), intermediate temperature (100-500°C), as well as the low temperature (<100°C). The solid-state protons or oxide-ion conductors are usually utilized for the high-temperature system. For the intermediate temperature range, the molten salt system is preferred. Finally, at a low temperature, polymer electrolytes or liquid electrolytes would be utilized. In this part, the electrochemical system will be introduced by the types of electrolytes.[47] Figure 2.8 presents a typical structure of an electrochemical system with different electrolytes.

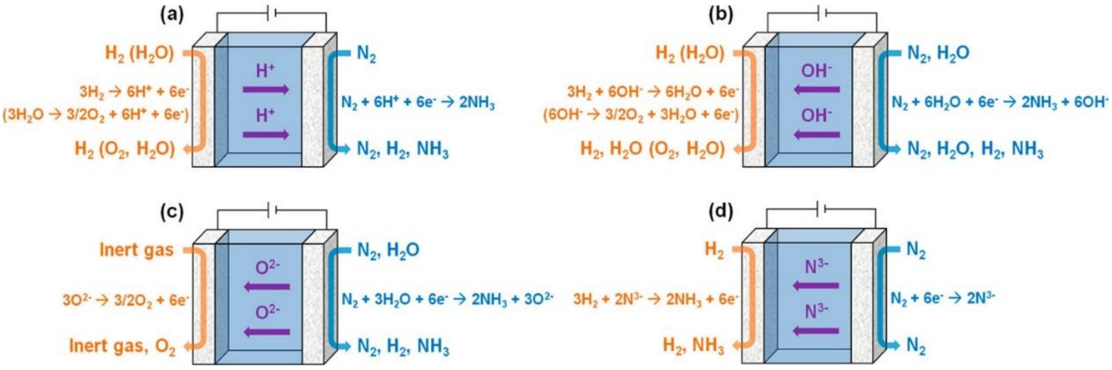

Figure 2.8 Typical electrochemical system for ammonia production using different types of electrolytes. (Reproduced with permission. Copyright 2020, American Chemical Society)

2.3.2.1 Solid-state electrolytes (500-800°C)

The electrochemical synthesis of ammonia using solid oxide electrolytes provides a significant advantage over the traditional Haber-Bosch process because it can work at ambient pressures. The solid-state electrolyte system typically works at a high temperature ranging from 500 to 800°C, largely dependent on the conditions of the electrolyte. For a high value of ions conductivity, high temperature is necessary for these systems. As shown in Figure 2.8a, c, the dense electrolytes are placed between two porous electrodes for a typical solid-electrolyte system. During their operation for ammonia synthesis, ions will pass through the solid electrolyte (usually H^+ or O^{2-} ions).

a) Proton-conducting electrolyte

Electrochemical reactors using protonic membranes have been identified as a viable alternative to the industrial HBP. The reactors are assembled with the proton-conduction membrane, which only permits the protons (H^+) to pass through. Thus, this process could be operated without hydrogen purification as in HBP, extensively reducing the cost in this part. A typical device based on a proton-conduction system is shown in Figure 2.8a.

In 1998, Marnellos and Stoukides[57] were the first to propose the electrochemical ammonia synthesis from N_2 and H_2 at a high temperature of 570°C. Their electrochemical system was similar to that shown in Figure 2.9, based on a proton-conducting solid oxide electrolyte. The metal palladium served as both the anode and cathode in the system. An H^+-conductor of $SrCe_{0.95}Yb_{0.05}O_3$ was placed between them. During its operation under 570 ºC, the hydrogen gas was continuous to the anode chamber, and the nitrogen was provided to the cathode chamber. Under a current density of ~2 mA cm^{-2}, the system delivered a high FE of ~78%, and the highest production rate of the system could achieve 17.4 mmol cm^{-2} h^{-1}. Compared to HBP, the system can be operated for NH_3 under atmospheric pressure. Thus, it was confirmed that the electric energy supplied could satisfy the thermodynamic needs for high pressure.

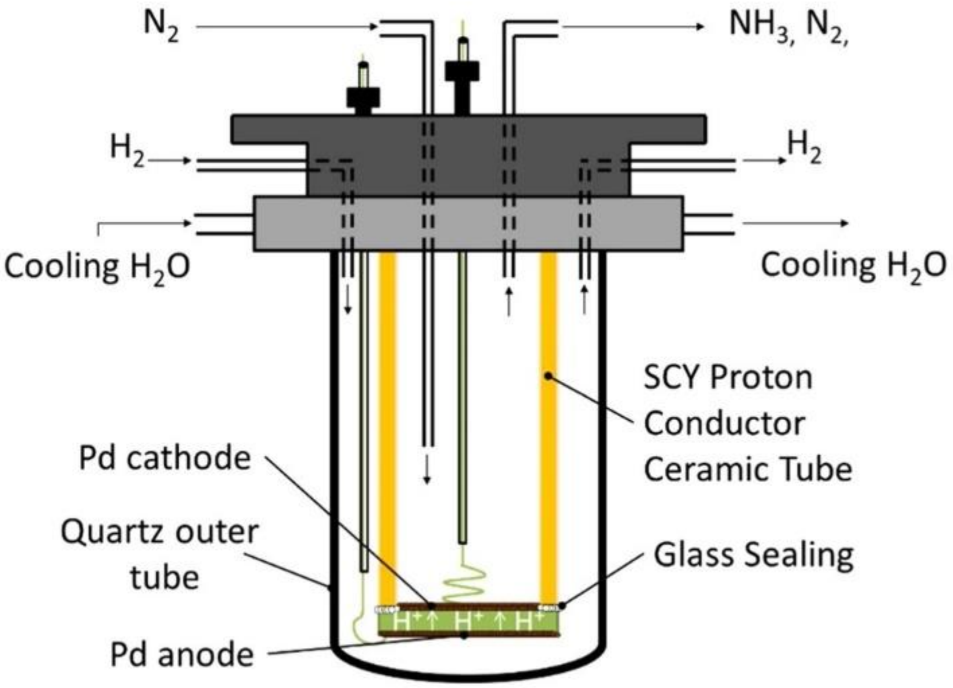

Figure 2.9 Solid-electrolyte ammonia synthesis reactor developed by Marnellos and Stoukides. (Reproduced with permission. Copyright 1998, American Association for the Advancement of Science)

Since then, as indicated in Table 2-3, several different teams have reported their study on this topic. Regardless of the proton electrolyte used, the data indicate that the ammonia generation rates are of the same order of magnitude, ~10^{-9} mol cm^{-2} s^{-1}, which is much below the rates required for commercial viability (4.3-8.7×10^{-7}mol cm^{-2} s^{-1}). As ammonia decomposes at 450°C (Figure 2.10), using ceramic materials with strong conductivity at temperatures below 450°C is desirable for further developing this technology.

Table 2-3Selected results of the electrochemical ammonia synthesis based on the solid-electrolyte system.[58]

Electrolyte	**WE**	**T (°C)**	**r_{NH3} (mol cm^{-2} s^{-1})**	**Input**
$Ba(Ca_{1.18}Nb_{1.82})O_{9-a}$ (BCN)	Ag-Pd	620	1.42×10^{-9}	H_2, N_2
$Ba_3Ca_{0.9}Nd_{0.28}Nb_{1.82}O_{9-a}$	Ag-Pd	620	2.16×10^{-9}	H_2, N_2
$Ba_3CaZr_{0.5}Nb_{1.5}O_{9-a}$ (BCZN)	Ag-Pd	620	1.82×10^{-9}	H_2, N_2
$BaCe_{0.2}Zr_{0.7}Y_{0.1}O_{2.9}$ (BCZY)	Rh	600	1.28×10^{-8}	H_2, N_2
$BaCe_{0.85}Y_{0.15}O_{3-a}$ (BCY)	BSCF	530	4.10×10^{-9}	H_2, N_2
$BaCe_{0.8}Gd_{0.1}Sm_{0.10}O_{3-a}$	Ag-Pd	620	5.82×10^{-9}	H_2, N_2
$BaCe_{0.9}Sm_{0.1}O_{3-a}$ (BCS)	Ag-Pd	620	5.23×10^{-9}	H_2, N_2
$BaCe_{0.9-x}Zr_xSm_{0.1}O_{3-a}$ (BCZS)	Ag-Pd	500	2.67×10^{-9}	H_2, N_2
$BaCe_{1-x}Ca_xO_{3-a}$ (BCC)	Ag-Pd	480	2.69×10^{-9}	H_2, N_2
$BaCe_{1-x}Dy_xO_{3-a}$ (BCD)	Ag-Pd	530	3.50×10^{-9}	H_2, N_2
$BaCe_{1-x}Gd_xO_{3-a}$ (BCG)	Ag-Pd	480	4.63×10^{-9}	H_2, N_2
$BaCe_{1-x}Y_xO_{3-a}$ (BCY)	Ag-Pd	500	2.10×10^{-9}	H_2, N_2
$Ba_xCe_{0.8}Y_{0.2}O_{3-a}$-0.04ZnO	Ag-Pd	500	2.36×10^{-9}	H_2, N_2
$Ce_{0.8}Gd_{0.2}O_{2-a}$ (CGO)	Ag-Pd	650	7.70×10^{-9}	H_2, N_2
$Ce_{0.8}La_{0.2}O_{2-a}$	Ag-Pd	650	7.20×10^{-9}	H_2, N_2
$Ce_{0.8}Sm_{0.2}O_{2-a}$ (CSO)	Ag-Pd	650	8.20×10^{-9}	H_2, N_2
$Ce_{0.8}Y_{0.2}O_{1.9}$-$Ca_3(PO_4)_2$-K_3PO_4	Ag-Pd	650	6.95×10^{-9}	CH_4, N_2
$Ce_{0.8}Y_{0.2}O_{2-a}$ (CYO)	Ag-Pd	650	7.50×10^{-9}	H_2, N_2
CeO_2-$Ca_3(PO_4)_2$-K_3PO_4	Ag-Pd	650	9.50×10^{-9}	H_2, N_2
$La_{0.9}Ba_{0.1}Ga_{1-x}Mg_xO_{3-a}$	Ag-Pd	520	1.89×10^{-9}	H_2, N_2
$La_{0.9}Sr_{0.1}Ga_{0.8}Mg_{0.2}O_{3-a}$ (LSGM)	Ag-Pd	550	2.37×10^{-9}	H_2, N_2
$La_{1.95}Ca_{0.05}Ce_2O_{7-a}$ (LCC)	Ag-Pd	520	1.30×10^{-9}	H_2, N_2
$La_{1.95}Ca_{0.05}Zr_2O_{7-a}$ (LCZ)	Ag-Pd	520	2.00×10^{-9}	H_2, N_2
$La_{1.9}Ca_{0.1}Zr_2O_{6.95}$ (LCZ)	Ag-Pd	520	1.76×10^{-9}	H_2, N_2
$SrCe_{0.95}Yb_{0.05}O_{3-a}$ (SCY)	Pd	570	4.50×10^{-9}	H_2, N_2
$SrCe_{0.95}Yb_{0.05}O_{3-a}$ (SCY)	Ru	650	4.90×10^{-13}	H_2O, N_2
Yttria-stabilized zirconia (YSZ)	Ru	650	1.12×10^{-13}	H_2O, N_2

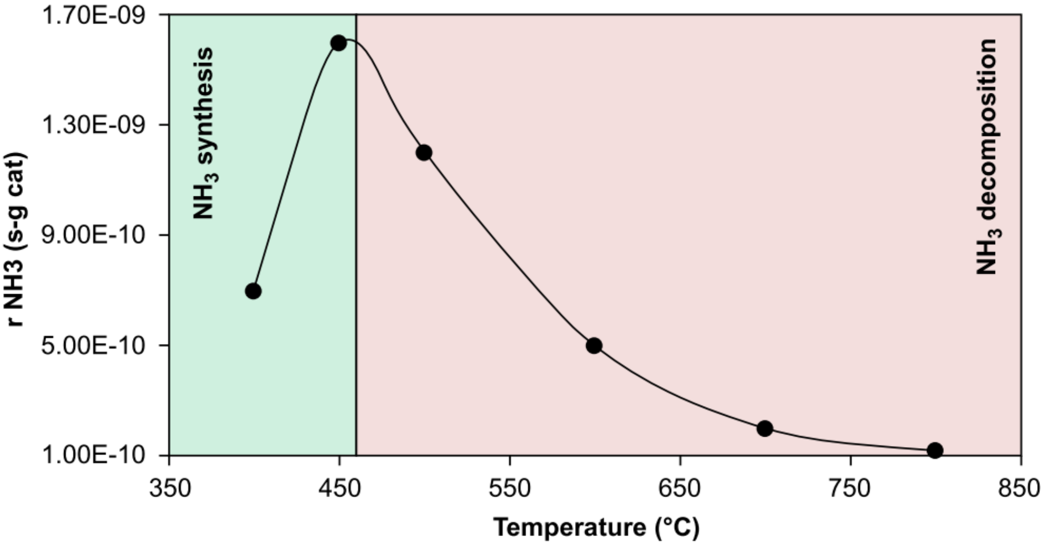

Figure 2.10 Ammonia production under different temperatures. (Reproduced with permission.[58] Copyright 2022, Elsevier)

b) Oxygen-ion conducting electrolytes

At atmospheric pressures, in addition to proton-conducting electrolytes, oxygen-ion-conducting electrolytes could also be employed for ammonia synthesis. At the cathode of this system, steam electrolysis and ammonia synthesis occur.

Stoukides' group[59] reported a solid-electrolyte system based on 8% Y_2O_3/ZrO_2 as an oxygen-ion conductor to produce ammonia under ambient pressure. At 650°C, the system delivered a production rate of 1.50×10^{-13} mol cm^{-2} s^{-1} from N_2 and H_2O as the reactants. The ammonia production rate was three times smaller than that reported proton-conductor system. This was explained by the presence of oxygen-containing species (H_2O) on the cathode side, which may increase the ammonia dissociation at these temperatures.

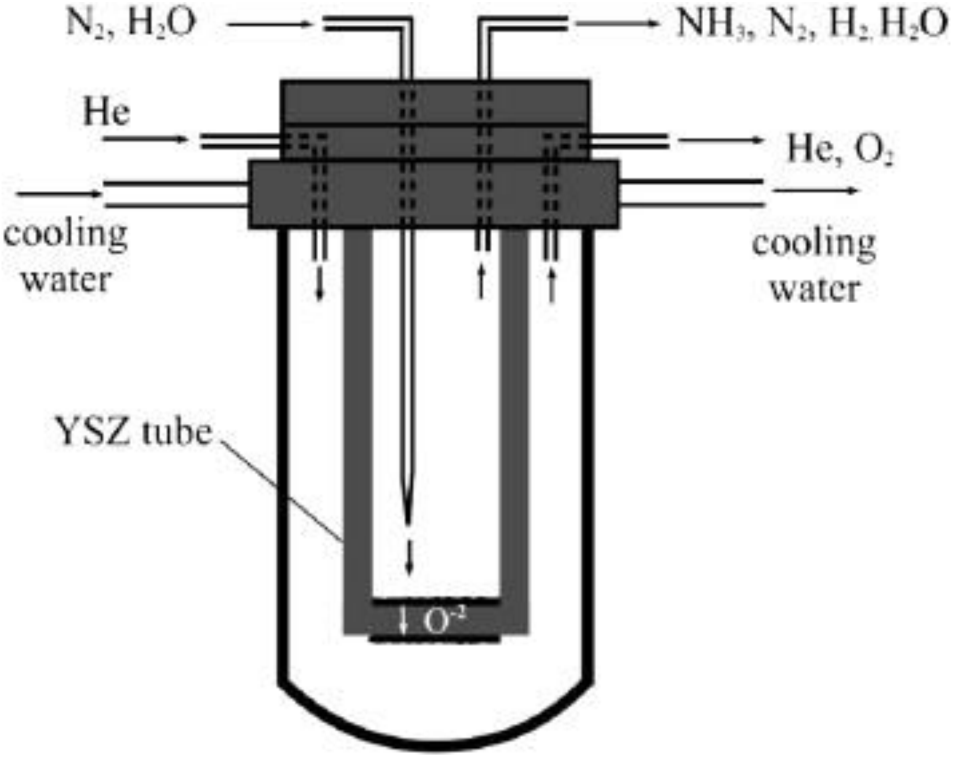

Figure 2.11 Illustration of the O^{2-}-conduction cell for ammonia production. (Reproduced with permission.[59] Copyright 2009, Elsevier)

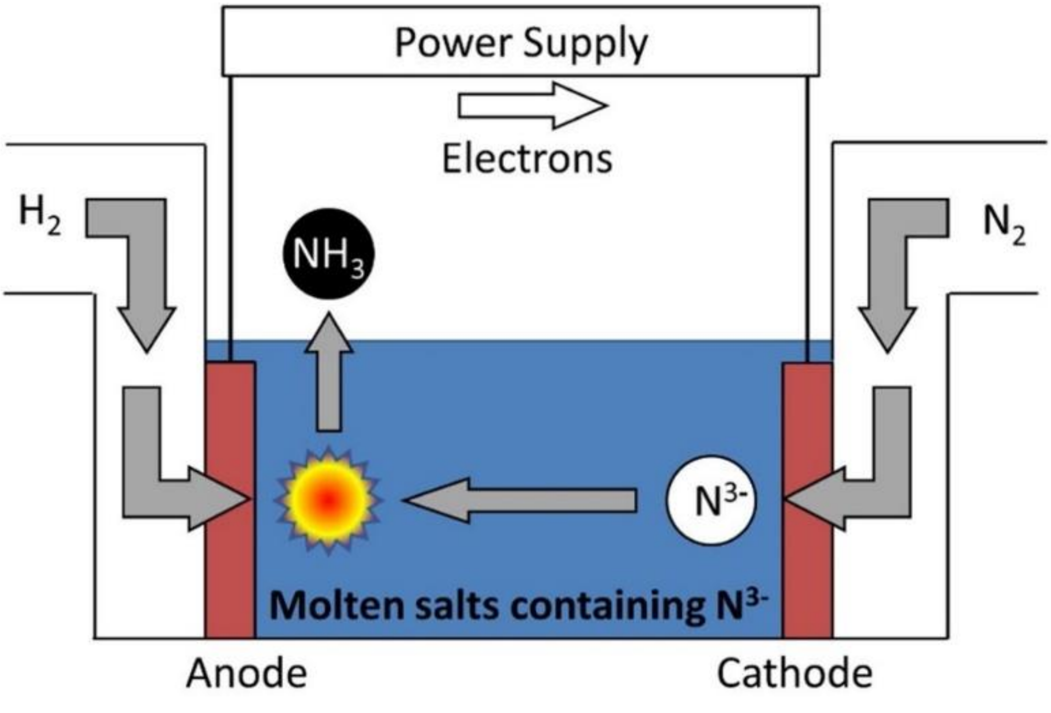

Figure 2.12 Schematic illustration of the operation of a molten salt electrochemical system for ammonia synthesis. (Reproduced with permission.[60] Copyright 2003, American Chemical Society)

2.3.2.2 Molten salt electrolytes (200-500°C)

For the electrochemical system, a temperature range of 200-500°C was typically employed for the molten salt electrolyte system. In this type of system, the nitrogen and hydrogen molecules would be converted to N/H species at the interface of the electrode. Under the driving force of the electric field, they would pass through the molten salt electrolyte. Furthermore, ammonia gas would be formed at the anode side by the reactions as follows:

$$\mathrm{N^{3-}} + \frac{3}{2}\mathrm{H_2(g)} \rightarrow \mathrm{NH_3(g)} + 3\mathrm{e^-} \qquad \text{2-7}$$

Therefore, it could be easily understood that in this type of system, the ionic mobility in the cell played an essential role in improving its ammonia production performance. Depending on the electrolyte used and the reaction mechanisms, the molten salt electrolyte system can be classified into molten chloride salts, molten hydroxide salts, and composite electrolytes.

Murakami's group[61] was the first to investigate ammonia production employing a molten salt electrolyte, including a eutectic combination of chlorides (LiCl, KCl, and CsCl).

Figure 2.12 depicts the functional diagram of the system. Using N_2 and H_2 as the feedstocks, the system reported an ammonia production rate of 3.33×10^{-9} mol s^{-1} cm^{-2} and a high FE of 72%. A similar work reported an increased rate of 2.02×10^{-8} mol s^{-1} cm^{-2}, using the H_2O as the hydrogen source, but with a relatively low FE of ~23%.[62] This decrease in FE can be explained by the competition of H_2O splitting with ammonia production in the electrochemical system. One of the critical issues in the molten system is that in the molten system, the evolution of Cl_2 in the Cl^- salt system could corrode the electrochemical system. And for the OH^--electrolyte system, the OH^- in the cell could facilitate the HER, thus leading to an unsatisfactory FE result.

c) Liquid electrolytes (<100 °C)

Under low temperatures, the decomposition of ammonia is no longer a concern. Electrochemical synthesis of ammonia using liquid electrolytes is a recent technology that has the advantage of being conducted at low temperatures (<100°C) and pressure, with ambient pressure being the mostly used. Ideally, reducing nitrogen into ammonia directly using water as the proton source near ambient temperature is sustainable. The concept of an aqueous electrochemical NRR system is that water is oxidized at the anode, providing protons and electrons to reduce nitrogen at the cathode with the following reaction:

$$\mathrm{N_2(g) + 8H^+ + 6e^- \rightleftharpoons 2NH_4^+} \qquad 2\text{-}8$$

$$\mathrm{N_2(g) + 6H^+ + 6e^- \rightleftharpoons 2NH_3} \qquad 2\text{-}9$$

As depicted in Figure 2.13, the Pourbaix diagram for the N_2-H_2O system, N_2 reduction to NH_4^+ or NH_3, is accessible thermodynamically. However, a highly effective electrocatalyst is required to suppress the influence of the parasitic hydrogen evolution reaction (HER), especially when high polarization is considered due to the high voltage needed to break the highly stable N_2 molecules.[63, 64] Unfortunately, few electrochemical systems are proven effective for competing with HER. As reported by Andersen et al.,[16] these electrolytes provide the concentration ranging from the PPB to PPM level, which is difficult to distinguish from the containment. Consequently, it is suggested to explore highly selective electrocatalysts to avoid HER, and in the meanwhile, rigorous control tests should be taken to confirm the reliability.

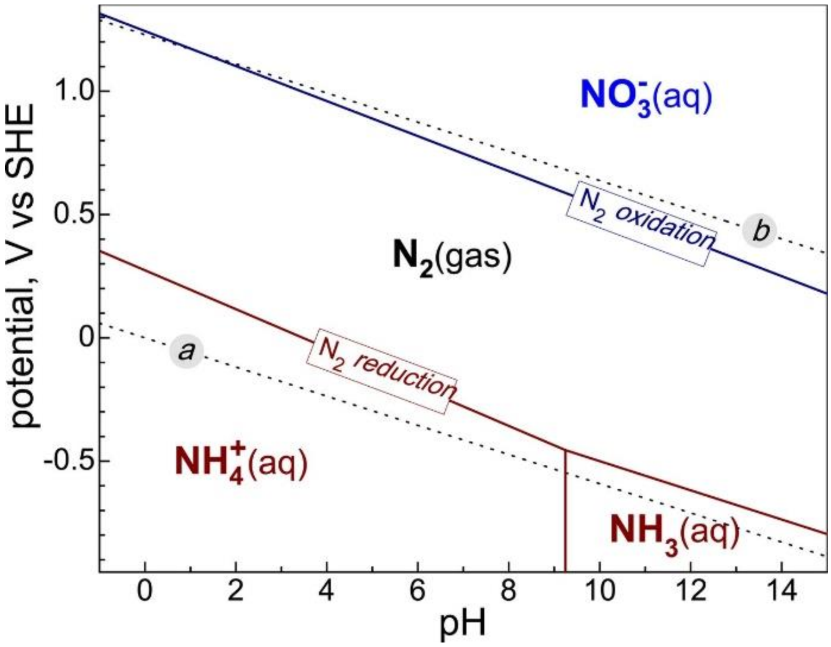

Figure 2.13 Partial Pourbaix diagram for the N_2-H_2O system. Solid lines represent N_2 reduction to NH_4^+/NH_3 and NO_3^- oxidation. Lines a (reduction to H_2) and b (oxidation to O_2) span the stability area of water. (Reproduced with permission.[14] Copyright 2018, American Association for the Advancement of Science)

2.4 Li-mediated ammonia electro-synthesis

2.4.1 Overview

Among the published chemistries utilizing electric energy, methods that employ lithium metal as a mediator report some appreciable rates with the highest Faradaic efficiencies (FEs) and for NH_3 synthesis, as well as repeatable results even under strict controls.[18, 20, 65, 66] Lithium metal is unique in that it can spontaneously dissociate the triple nitrogen bond at ambient conditions.[19] Such property makes it possible to produce ammonia under ambient conditions by combining thermochemical and electrochemical reactions.

In the Li-mediated ammonia electro-synthesis, as illustrated in Figure 1.6, Li-ions are firstly reduced to metallic Li under electric energy. The produced Li metal could provide the reactive surface to spontaneously split the N≡N through a known reaction, forming lithium nitride, Li_3N. Li_3N is an alkaline solid material, which can be easily reacted with a proton source (e.g., ethanol or water) to produce ammonia and release Li^+. After ammonia formation, the Li^+ will be reduced to metallic Li for another Li-medicated cycle. In the Li-mediated cycle, the initial Li plating is the electrochemical step that is uphill climbing step from a thermodynamic perspective. Furthermore, the remaining steps are chemical and thermodynamically spontaneous.

The Li-mediated ammonia synthesis could be operated using different routes based on the operation condition of the three steps. Herein, the process is divided into two main categories, determined by whether the three steps are performed separately or simultaneously, namely, the stepwise or continuous strategy.

2.4.2 Continuous Li-mediated method

2.4.2.1 Process description

Typically, as demonstrated in Figure 2.14,[67] a continuous method was designed based on the non-aqueous electrolyte (e.g., 0.2 M lithium perchlorate, 1% ethanol in tetrahydrofuran solution) to avoid parasite reactions consuming Li. During operation for ammonia, the Li-ions in the electrolyte would be electro-deposited on the surface of the metal electrode (e.g., Mo, Cu, etc.) as metallic Li. The Li spontaneously breaks the triple N_2 bond of the nitrogen gas molecules dissolved in the electrolyte. After contact with the electrolyte's protons (e.g., ethanol), ammonia will be produced in the system. Through the continuous method, ammonia could be directly produced in one device without further operations.

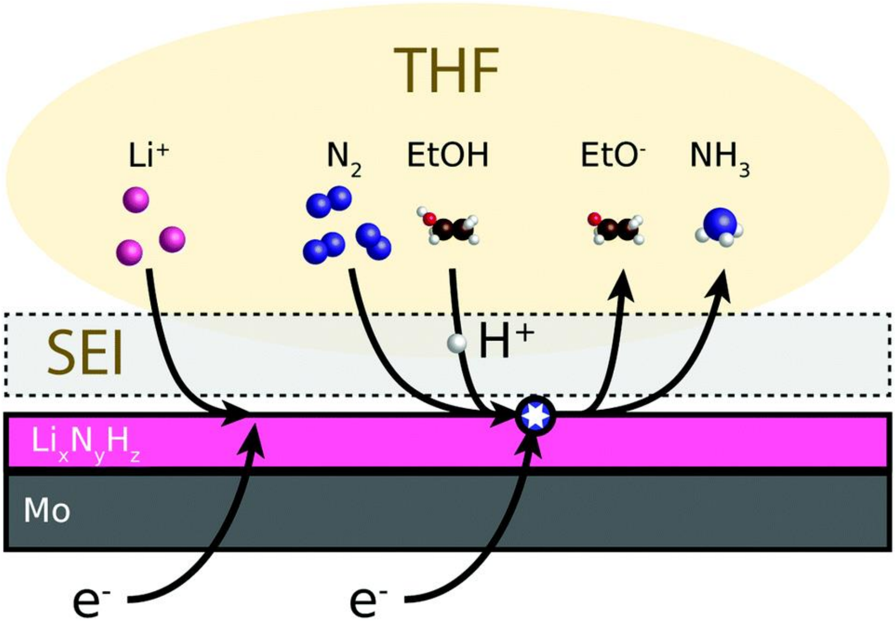

Figure 2.14 Mechanism illustration for the lithium-mediated ammonia electro-synthesis.(Reproduced with permission.[68] Copyright 2020, Royal Society of Chemistry)

2.4.2.2 Research advances of continuous Li-mediated method

a) Building up the continuous Li-mediated method

The conceptual approach was proposed early in 1930.[69] In 1993, Tsuneto et al.[70] built up the first electrochemical device using electrolyte 0.2M $LiClO_4$ in THF/ ethanol (99:1 v/v) for NRR, realizing a high FE of 8.4% and calculated production rate of 2.09 mmol cm^{-2} h^{-1} under 0.1 MPa of N_2. Based on the device and experimental results, they proposed a possible mechanism of Li-mediated ammonia synthesis. The Li metal deposited on the electrode reacts with N_2 gas, producing Li_3N, which is then protonated by an appropriate protic additive (ethanol) to produce ammonia. This research provided an intuitive and straightforward mechanism understanding of the process.

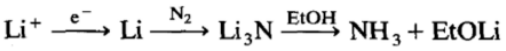

$$Li^+ \xrightarrow{e^-} Li \xrightarrow{N_2} Li_3N \xrightarrow{EtOH} NH_3 + EtOLi$$

Figure 2.15 Possible mechanism of continuous Li-mediated pathway proposed by Tsuneto.[65]

In 1994, their following study obtained a higher FE of 57.7% under 5 MPa N_2, followed by a rate of 14.34 mmol cm^{-2} h^{-1} They pointed out that the FE is related to the protic source, nitrogen pressure, as well as deposited substrates.[16] Subsequent research was also built based on the system that organic Li-containing electrolytes with a sacrificial proton source were uniquely able to reduce nitrogen under ambient conditions. The repeatability and consistency of these two works have been confirmed with blanks and isotope tests in 2019.[16]

b) Mechanism understanding

The high and quantifiable FE and NH_3 formation rate make it essential to explore a clear understanding of the Li-mediated electrochemical NRR process so as to optimize it. Early in the 1990s, Tsuneto et al. proposed the possible mechanism, as depicted in Figure 2.15, that deposited Li reacts with N_2 to produce Li_3N followed by protonated with protic additives for ammonia production alongside returning parts of deposited Li to the solution in the form of EtOLi.[65]

Since then, only in 2019, some progress has been made by Lazouski et al. by developing a microkinetic model and introducing the concept of transport limitation into the mechanism (Figure 2.16).[67, 71] It is observed that FE for ammonia tends to exhibit a peak value with increased protic concentration and current density. Furthermore, FE increases linearly with the N_2 pressure. The model applied optimal conditions to obtain a high FE of 18.5% ± 2.9% and a production rate of 7.9 ± 1.6 nmol cm^{-2} s^{-1}. However, this progress was built upon the critical assumption that Li has been consumed in the reaction to H_2 or NH_3, failing to consider SEI growth.

Most recently, Schwalbe et al.,[72] reported that there remains an intact deposited layer of Li metal, beneath the SEI layer, through Li stripping test and EIS. Based on the results and DFT calculation, they provided a more complex mechanism that, besides the Li deposition, ammonia formation, and nitrogen activation, there possibly remains an additional pathway that electrons for driving catalysis come from the underlying Li metal when operated under Li deposition potential, considering the intact Li, proceeding a heterogenous mechanism like the HBP catalysts and reach a FE of ~10%. However, in the absence of an understanding of the mechanism for Li dissolution, the role of accumulated Li is still unclear.

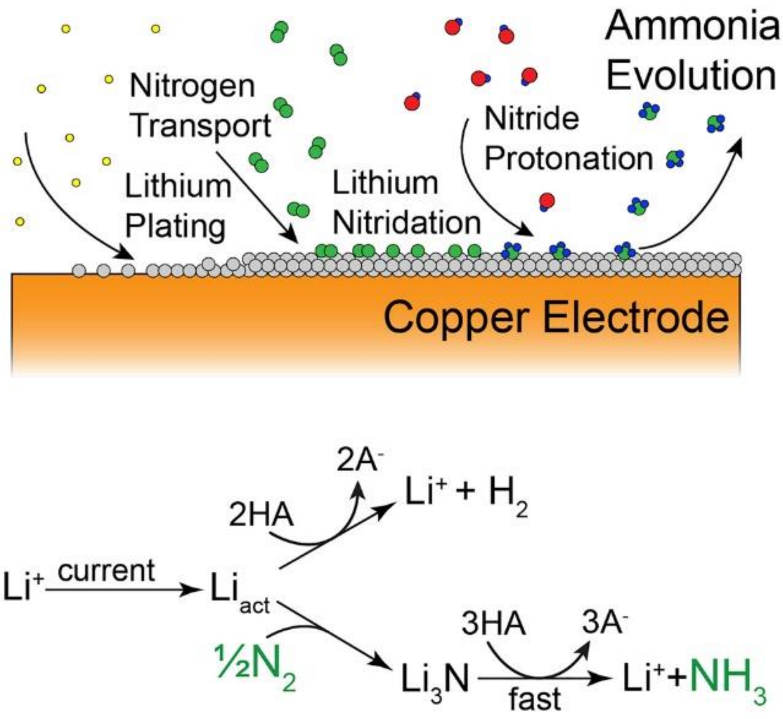

Figure 2.16 Possible mechanism of Li-mediated method provided by Lazouski in 2019, with additional consideration of the impact of N_2 transport limitations. (Reproduced with permission.[67] Copyright 2019, Elsevier)

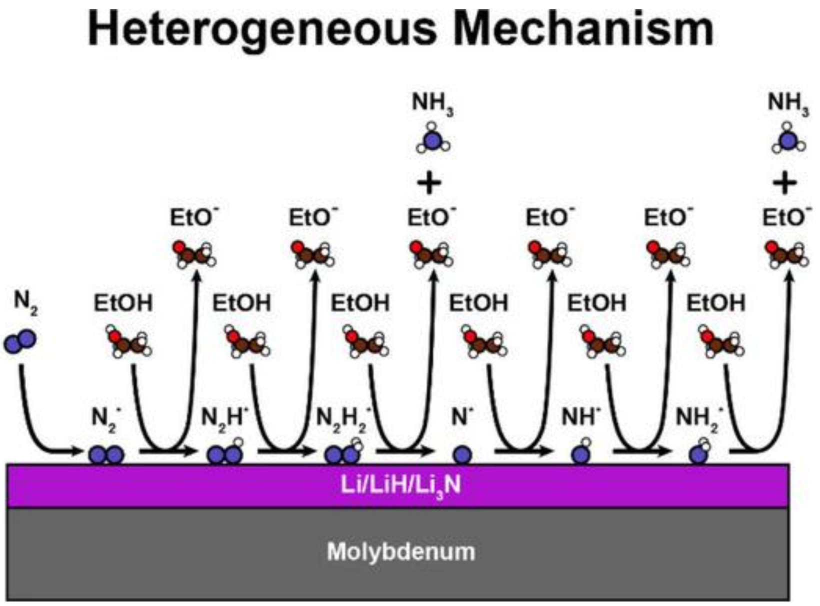

Figure 2.17 A possible heterogeneous mechanism, where there always remains certain amount of metallic Li in the electrode. (Reproduced with permission.[72] Copyright 2020, Wiley)

Based on the former study, as shown in Figure 2.18, Andersen et al.[68] proposed a more general kinetic model to describe the Li-mediated process to further increase the FE. The model considers that the process is made up of many elementary steps, including mass transportation from the bulk solution to the electrode surface, formation of the Li active site, and catalytic formation of H_2 and NH_3. They consider that the diffusion process is likely to be slow, the electrochemical process is expected to be very fast due to the extreme reducing potential as the driving force. According to Singh et al.,[72] the dissociative N_2 chemical adsorption on Li active site is calculated to have a low kinetic barrier. Based on the model, FE can be predicted as a function of nitrogen ratio over lithium and proton to lithium (Figure 2.18a). It could be observed that the domain of high FE was in the area where r_H/r_{Li} and r_{N2}/r_{Li} is large. Thus, besides increasing the concentration of ethanol and nitrogen to increase the r_H and r_{N2}, decreasing the r_{Li} can also make the system reach a high FE (Figure 2.18b). Thus, potential cycling was proposed to reduce the Li plating rate by regular Li plating and rest. Consequently, based on the insight, the FE of the system was improved significantly to 37.1±1.3%.

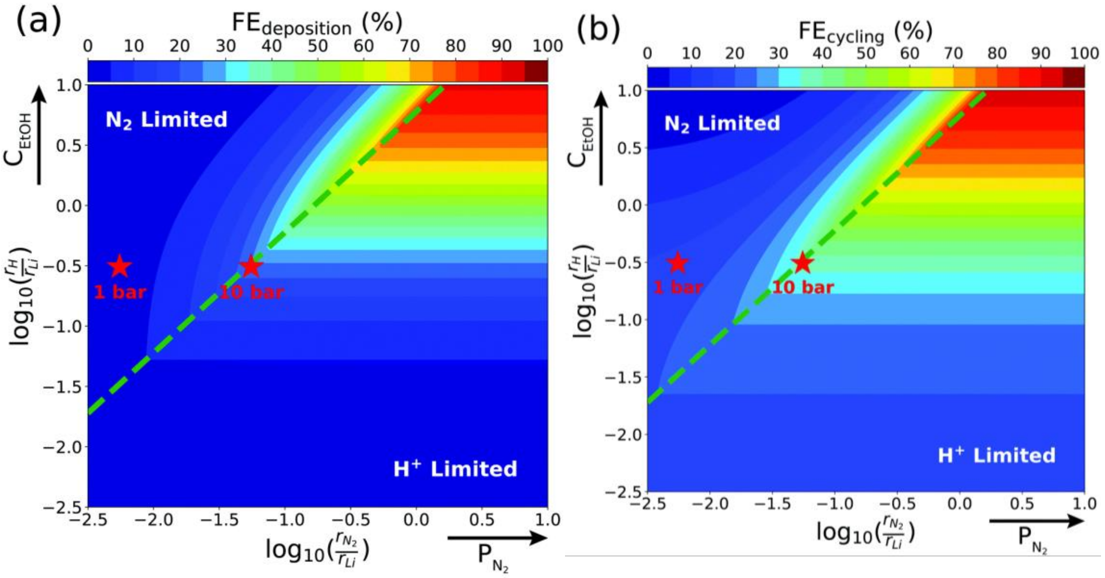

Figure 2.18 Heatmap of the predicted FE as a function of the ratio of nitrogen to lithium (x-axis) and proton to lithium (y-axis) diffusion rates. (a) shows the FE during continuous Li plating, and (b) shows the FE during potential cycling. (Reproduced with permission.[68] Copyright 2020, Royal Society of Chemistry)

c) Gas diffusion electrode

Through deeply exploring the possible mechanism, high FE can be obtained by optimizing the operating parameters and conditions. According to Andersen's model, it could be concluded that the limited mass transport of reactant gas (N_2 and H_2) to the electrode could hamper the ammonia production performance of the Li-mediated system. To solve it, Lazouski et al. proposed a novel gas diffusion electrode (GDE, Figure 2.19) method. The GDE combines the feature of the gas tube and electrode, thus directly inputting gas to the reaction surface of the electrode. It solved the transportation limiting issues due to low solubility. Consequently, the ammonia partial current density can reach 8.8 ± 1.4 mA cm^{-2} and FE of 35 ± 6%.

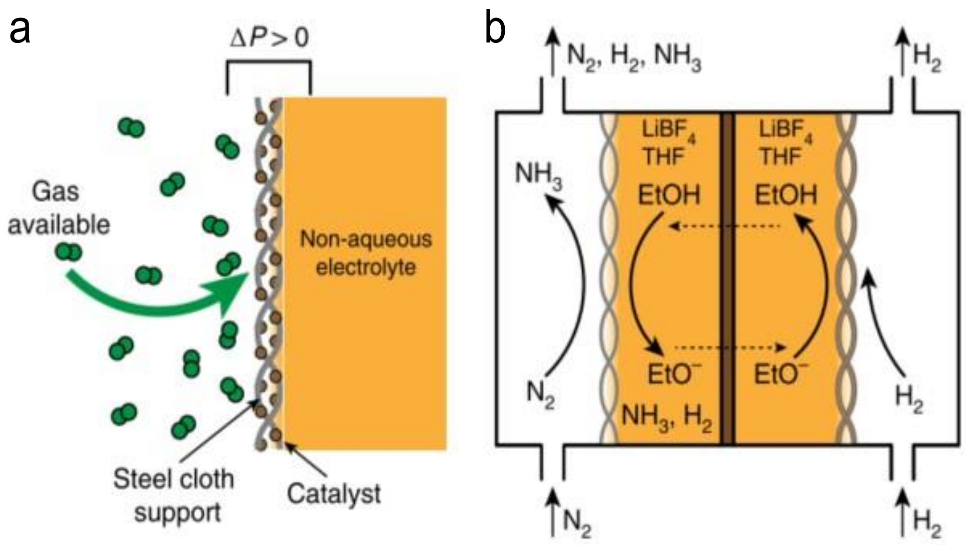

Figure 2.19 a) structure of a GDE, with a catalyst coated on steel cloth; b) structure of proton donor-cycling cell based on GDE. (Reproduced with permission.[73] Copyright 2020, Springer Nature)

d) Proton shuttle carrier

Although introducing GDE into the Li-meditated system can provide a high yielding rate performance with abundant protons, the sacrifice protons source, ethanol still serves as the medium to transport protons between anode and cathode. Recent research has pointed out that ethanol can be unstable in shuttling protons, and its vulnerability to oxidation at the anode is potentially a significant issue, limiting the system's lifetime.[68] To realize the longevity of the Li-mediated system, a stable protons shuttle is required to be completely recycled in the cell without consumption. Based on the situation, as exhibited in Figure 2.20, Suryanto et al. reported a phosphonium salt,[12] as a proton shuttle, with high stability and high ionic conductivity, enabling a continuous operation for more than three days. Furthermore, the system also possesses a high production rate of 53 ± 1 nmol cm^{-2} s^{-1} and FE of 69 ± 1% in 20-hour experiments under 0.05 MPa of H_2 and 1.95 MPa of N_2.

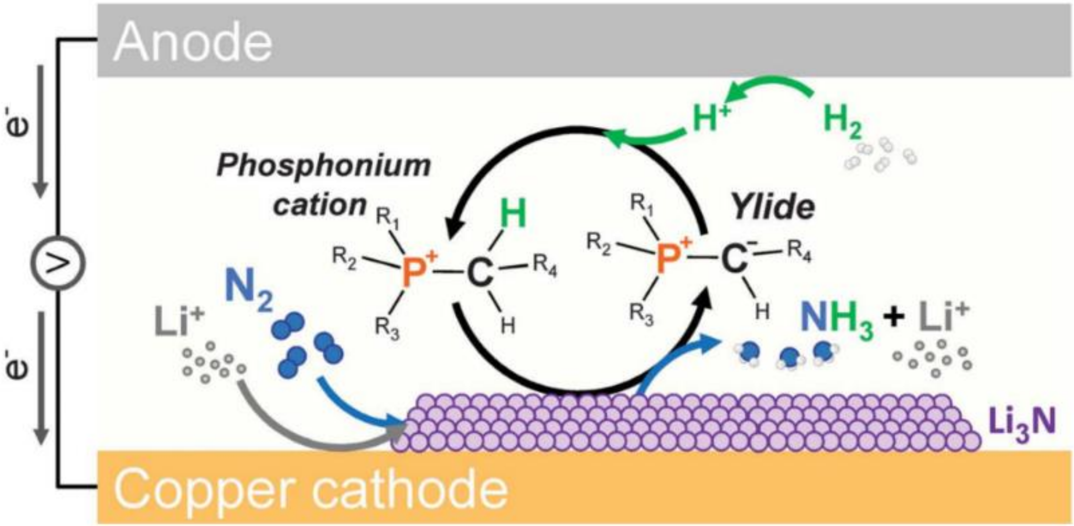

Figure 2.20 Schematic illustration of sustainable Li-mediated method for ammonia from H_2 and N_2 based on phosphonium cation as a new proton carrier. (Reproduced with permission.[12] (Copyright 2021, American Association for the Advancement of Science)

e) Trace O_2 addition

Another strategy to improve the performance of the Li-mediated method is based on an interesting finding that the addition of a trace amount of oxygen into the N_2 feeding gas will significantly improve the FE as well as the stability of the system, as reported by Li.[74] Through adding 0.6 to 0.8 mol% oxygen in 2 MPa N_2, the system tends to exhibit a high FE of 78.0 ± 1.3% at a high current of -4 mA cm^{-2}. According to Singh's model, it is believed that the addition of little oxygen can modify the composition of the SEI layer, thus reducing Li^+ conductivity for high FE.

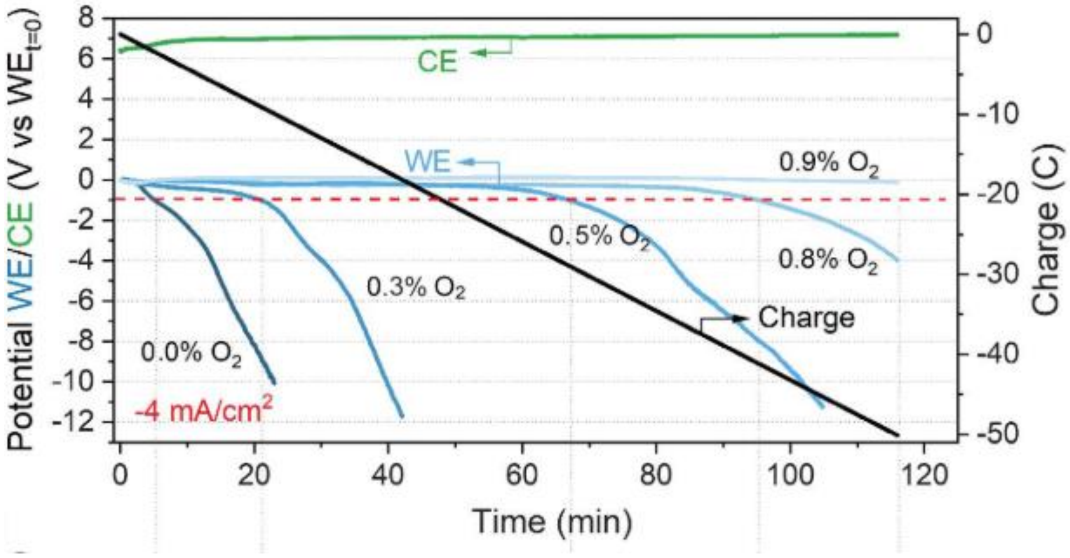

Figure 2.21 the stability performance of the Li-mediated ammonia synthesis versus the content of oxygen in the N_2. (Reproduced with permission.[74] Copyright 2021, American Association for the Advancement of Science)

Table 2-4 Selected performance of continuous Li-mediated ammonia synthesis.

ref	Proton source	N_2 pressure (MPa)	Voltage (V)	Current (mA cm^{-2})	Rate (nmol s^{-1} cm^{-2})	Time (h)	FE (%)
[68]	1% vol. EtOH	1	-6	-2	0.7	~50	37.00
[73]	0.1 M EtOH	0.1	30	-25	30	0.08	35 ± 6
			>20	-20	13	2.17	18.90
[67]	0.1 M EtOH	0.1	15	-8	5.12 ± 0.81	0.25	18.5 ± 2.9
[70]	1% vol. EtOH	0.1	-	-2	-	-	8.40
[75]	1% vol EtOH	0.1	8	-	0.75	0.5	34.00
[16]	1% vol. EtOH	0.1	9	2-3 mA	7.5	-	7.5
[72]	2 vol. % EtOH	0.1	4	-1.1	-	2	5.00
[74]	1 vol. % EtOH	2	~7	-4	11.09	<2	78.00
[12]	0.05 MPa H_2	1.95	5	-22.5	53 ± 1	20	69 ± 7
			6.5-8	-24	42	2	50.00

2.4.2.3 Challenge and opportunity

Despite the advances, the system is not ideal with regard to Li. Firstly, metallic lithium does not necessarily react only with the dinitrogen in the solution to form the nitride. It can react directly with the proton source to form hydrogen, an undesired side product, lowering the Faradaic efficiency. Furthermore, during ammonia production, the electrolyte will undergo severe reduction at the surface of Li, and the by-product will be accumulated, resulting in growing resistance and overpotential. Furthermore, the continuous consumption of limited electrolytes and continuous growth of overpotential finally destroys the system.[68] That is also why the continuous Li-mediated system can only produce ammonia in limited operating life, as shown in Table 2-4. Thus, a deep mechanism should be explored to improve the continuous method further, and SEI modification could provide a possible solution.

2.4.3 Stepwise Li-mediated method

Despite the high selectivity and conversion in the continuous Li-mediated system, it is challenging to continuously reduce N_2 molecules through high reactive Li metal under extremely reductive potential in the environment of proton and organic electrolytes. The stepwise strategy possibly provides a solution for the system by separating the active Li deposition from the simultaneous nitridation and protonation reaction. Each step is an independent unit. Compared to the non-aqueous system, the stepwise one can even directly utilize sustainable water as the protic source due to the separation of Li deposition from protonation.

In the stepwise Li-mediated method, metallic Li was directly exposed to N_2, forming Li_3N, followed by the protonation to produce ammonia. In the cycle, because the nitridation and hydrolysis are chemically spontaneous reactions under ambient conditions, the only challenge lies in the step of Li plating, electro-reducing Li^+ to metallic Li. To accomplish the target, several methods were proposed to plate Li, including molten salt electrolysis and the membrane method for separation.

2.4.3.1 Molten salt electrolysis

Nørskov's group firstly proposed this stepwise Li-mediated pathway for ammonia synthesis.[20] The demonstrated strategy, as shown in Figure 2.22, is composed of 3 steps including Li deposition by molten salt electrolysis of LiOH, nitridation of Li metal with N_2 gas, followed by water protonation. The process is sustainable in both energy input and feedstocks without any harmful product, in which Li and LiOH serve as a medium and can be reused. The system can reach a remarkable FE of 88.5% due to high efficiency in individual steps. However, the cycle contains a step of molten salt electrolysis under a high operating temperature of 400-500℃. Furthermore, LiCl has been added to decrease the melting point of the system, which may cause Cl_2 evolution and can damage the device during long-time operation. The high operating temperature and a particular requirement on equipment will hamper its practical application in a distributed manner.

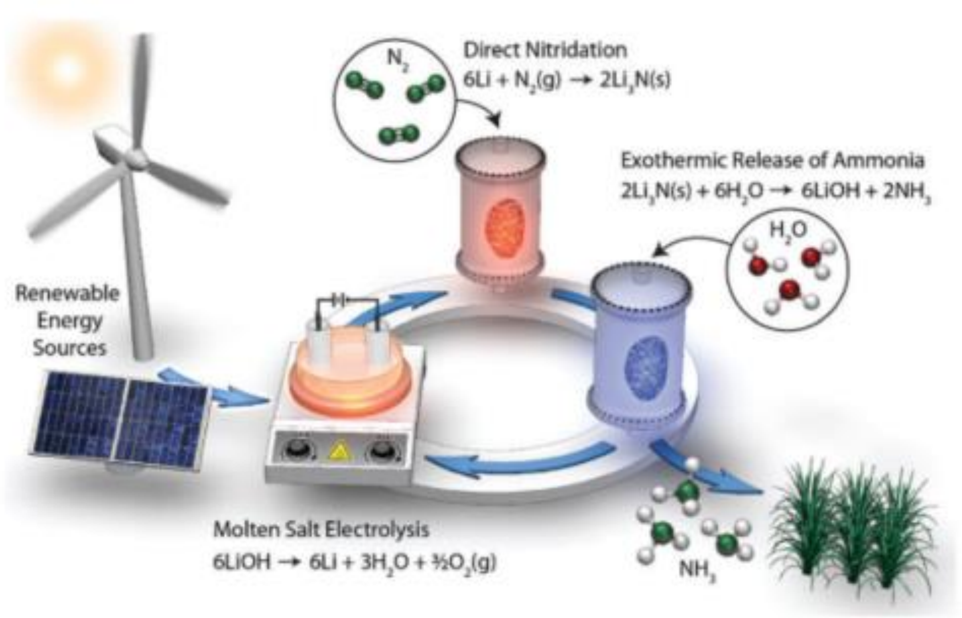

Figure 2.22 Conceptual stepwise Li-mediated method by Nørskov's group in 2017. (Reproduced with permission.[20] Copyright 2017, Royal Society of Chemistry)

2.4.3.2 Physical separation

Lim et al.[21] proposed a new approach to deposit Li metal using a lithium-ion conducting glass-ceramics (LISICON) membrane to obtain room-temperature Li deposits, as depicted in Figure 2.23. This membrane makes it feasible to obtain metallic Li from an aqueous Li salt solution with electric energy under ambient conditions. Such a system can yield a high FE of 52.3%. Based on the system, another work was proposed to improve the Li plating efficiency through the additive of $CsClO_4$, used in the Li battery to modify the Li metal anode. Based on changing the electrolyte composition, such a LISICON-based system can reach a high FE of 82.3%.[66]

Even though applying the LISICON membrane can contribute to ambient Li deposition, the following factors hamper the application of such a system. Firstly, the LISICON membrane has relatively minor Li^+ conductivity and will cause a higher overpotential for a high deposition rate. High operating voltage (>6V) makes the system unstable during long-time operations. Furthermore, the LISICON membrane is usually expensive, and it is challenging to fabricate it into a large membrane for a large amount of Li deposition. Moreover, there remains a doubt whether the membrane can separate the highly reactive Li from water solution for a long time.

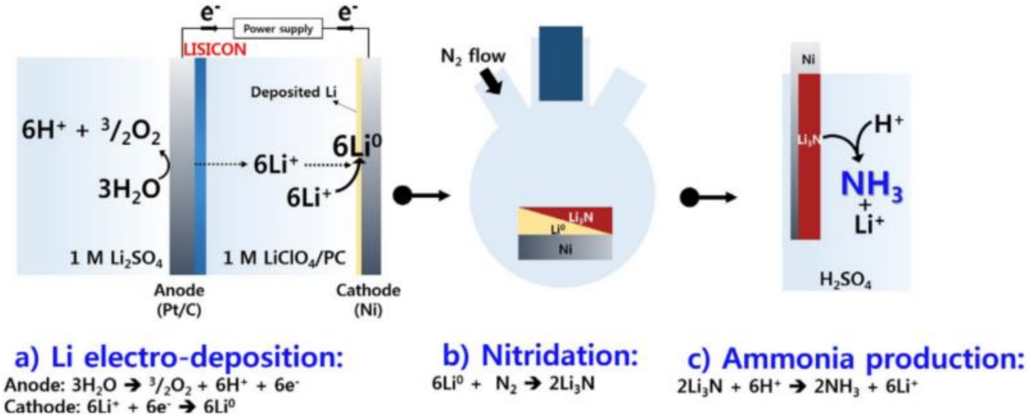

Figure 2.23 Stepwise Li-eNRR based LISICON membrane. (Reproduced with permission.[21] Copyright 2017, Wiley)

To explore a membrane to separate the aqueous Li solution from an organic electrolyte to deposit Li metal, as shown in Figure 2.24, Kim et al. developed an immiscible aqueous/organic hybrid electrolyte system by utilizing their immiscible property to produce metallic Li under lower voltage (5.3 V at 5 mA cm^{-2}) without LISICON.[19] Such an approach exhibits a FE of 57.2% and a production rate of 1.21 nmol cm^{-2} s^{-1} for producing ammonia. However, such a system can be dangerous in practical application due to a lack of physical separation, and it is also challenging to maintain a water-free state for the organic electrolyte in direct contact with water for a long time.

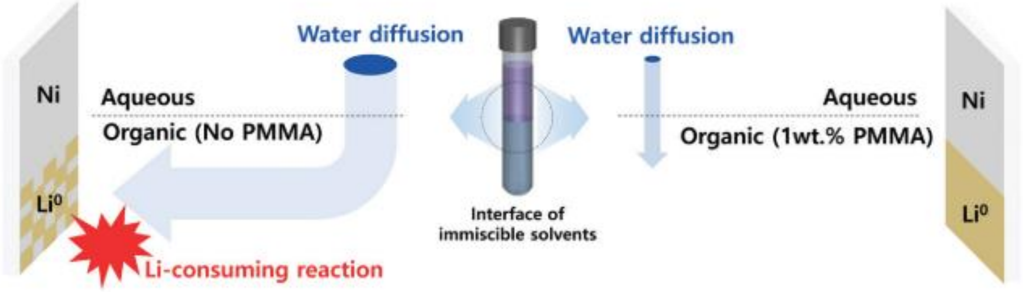

Figure 2.24 A diagram depicting water diffusion via the interface between the immiscible solvents and the resulting Li-consuming side reaction. (Reproduced with permission.[19] Copyright 2019, Royal Society of Chemistry)

2.4.3.3 Challenge and opportunity

Compared to the continuous method, the stepwise method could provide a higher value of FE due to the isolation of Li plating from the other steps, thus protecting the reactive Li for efficient ammonia production. However, due to the high reactivity of metallic Li, only a limited method was proposed to plate Li. Furthermore, some of them need to be operated under high temperatures. Moreover, the membrane method's long-term stability of the Li plating system is questionable. Thus, a possible alternative method should be explored for efficient and stable Li plating.

2.5 Proposal of LMB-mimic system to plate Li from LiOH

For Li plating by electric energy, the Li^+ is required to move towards the electrode to receive electrons. After combined with electrons, the Li^+ can be reduced to metallic Li. However, in the ambient Li-mediated cycle, the Li^+ source is the LiOH aqueous solution. The Li^+ can move freely in the water solution under ambient conditions. When applying the electric energy, the widespread protons in water prefer receiving the electrons compared to the Li^+. Furthermore, even though metallic Li is successfully plated, since metallic Li is chemically reactive toward almost all known chemicals upon immediate contact, it is almost impossible to protect the products from being consumed by parasite reactions, leading to a poor FE towards NH_3 production. Thus, it is required to plate Li in a Li-friendly system, combined with continuously moving the Li^+ from the LiOH solution into the system.

In this context, the concept of rechargeable lithium metal battery (LMB) offers a Li-friendly system for Li plating.[18, 76, 77] In the LMB, during charging, Li^+ will be de-intercalated from the cathode and released into the organic electrolyte, and flow to the anode, driven by the electric field. Moreover, in the meanwhile, electrons move from a high-potential cathode through the external circuit to a low-potential anode to combine lithium-ion for Li plating. Because of the strong reactivity of the Li products, insoluble byproducts are formed on the surface of Li metal, commonly denoted the solid-electrolyte interphase (SEI), constituting a passivation layer. Such a layer could effectively avoid further chemical reactions between the Li metal and the electrolyte.[78] And the amount of Li consumed for forming SEI is neglected, and usually, its thickness is only several nanometers.[3] Thus, the LMB system could be a promising candidate for stable and efficient Li plating.

Another problem is moving the Li^+ from the aqueous solution to the LMB system. In this regard, a spontaneous reaction between Li-deficient electrode materials and the LiOH aqueous solution is introduced here (Eq. 2-10).[79] It is reported that the Li-deficient spinel lithium manganese oxide (MnO_2) can spontaneously extract Li^+ from LiOH aqueous solution under specific conditions by intercalating Li^+ into the crystal lattice of MnO_2, forming less Li-deficient spinel oxide, $Li_yMn_2O_4$ ($0<y<1$). In this thesis, the spontaneous Li recovery reaction has been further extended. It has been confirmed thermodynamically and experimentally in this work that, the Li-deficient electrode, $Li_{1-x}Mn_2O_4$, ($0<x<1$) can fully lithiated to $LiMn_2O_4$ in 0.1M LiOH. Based on the extended reaction (Eq. 2-11), Li^+ can be moved from an aqueous LiOH solution to the LMB system.

$$\mathrm{MnO_2 + LiOH \rightarrow Li_yMn_2O_4 + H_2O + O_2} \qquad \text{2-10}$$

$$\mathrm{Li_{1-x}Mn_2O_4 + LiOH \rightarrow LiMn_2O_4 + H_2O + O_2} \qquad \text{2-11}$$

Based on the spontaneous Li recovery reaction and the Li-friendly LMB system, a novel Li plating method, the LMB-mimic system, is therefore proposed in this thesis, as illustrated in Figure 2.25 The LMB-mimic system is comprised of two steps in each cycle, including Li recovery and Li plating in LMB. In the Li recovery step, the free-standing Li-recovery electrode, FS-L_{1-X}MO, consisted of $\mathrm{Li_{1-x}Mn_2O_4}$, will spontaneously extract Li^+ from the LiOH aqueous solution, forming $LiMn_2O_4$. Followed by that, in the Li plating step, metallic Li will be plated in the LMB system by the Li^+ de-intercalated from $LiMn_2O_4$, regenerating $Li_{1-x}Mn_2O_4$.

It has been reported that $LiMn_2O_4$ has excellent stability toward Li^+ de-intercalation/intercalation in both organic systems and aqueous solutions.[80-82] Thus, it is believed that the spinel oxide can be used for multiple cycles of Li recovery and plating. Consequently, the LMB-mimic system can be a promising method for stable and efficient Li plating from an aqueous LiOH solution. Furthermore, the Li-mediated ammonia synthesis based on the LMB-mimic system can be operated continuously to produce ammonia from sustainable feedstocks and energy under ambient conditions.

In this study, an LMB-mimic system was proposed and designed to continuously plate metallic Li from the LiOH solution, to support the cyclic Li-mediated ammonia synthesis. Through the Li recovery step, Li^+ will be spontaneously extracted from LiOH into the electrode, FS-L_{1-X}MO, generating FS-LMO. Followed by the Li plating in LMB system, the electrode will release the Li^+ in Li-friendly system. After accepting electrons, Li+ could be plated into metallic Li. Considering the protective SEI layer would protective further consumption of Li deposits, thus both the Li plating and Li products are stable. Thus, it is believed to stably and efficiently to plate Li metal from LiOH aqueous solution. Considering the stability of FS-LMO for Li+ de-/intercalation, it is believed that the LMB-mimic system could operate for multiple cycles of Li recovery and plating. Consequently, it is predicted that the Li-mediated method, based on the LMB-mimic system, could produce ammonia efficiently and stably in a cyclic manner

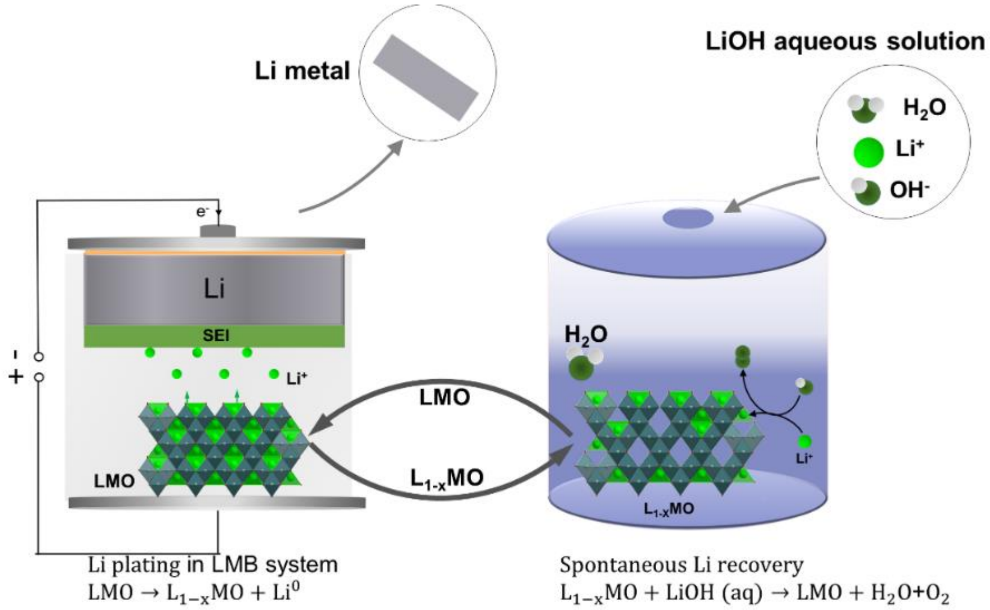

Figure 2.25 LMB-mimic system to plate Li metal from Li.

Chapter 3 Experimental Section

3.1 Materials

The chemical reagents and laboratory equipment used in this work are shown in Tables 3-1 and 3-2.

Table 3-1 Materials used in the experiments

Item	Formula	Grade	Supplier
Polyvinylidene fluoride	$-(C_2H_2F_2)_n-$	Tech	MTI
Cu Foil	Cu	Tech	MTI
Dimethyl Carbonate	$(CH_3O)_2CO$	AR	Dodo chem
1-Methyl-2-pyrrolidinone	C_5H_9NO	AR	Sigma-Aldrich
Separator [Celgard 2500]			Celgard
Battery shell [CR2016]	Tech		MTI
Li foil	Li	Tech	MTI
Lithium Hydroxide	LiOH	AR	Sigma-Aldrich
Ethyl alcohol	CH_3CH_2OH	AR	Sigma-Aldrich
Lithium Manganate	$LiMn_2O_4$	AR	MTI
Carbon Black, Acetylene	C		Alfa
Electrolyte [LB005]	1.0M $LiPF_6$ in EC: EMC=3:7 Vol%	Tech	Dodo chem
Nitrogen gas		99.99%	Linde
Sodium Hydroxide	NaOH	AR	Sigma-Aldrich
Sodium salicylate	$C_7H_6O_3 \cdot Na$	AR	Sigma-Aldrich
Potassium sodium tartrate tetrahydrate	$C_4H_4O_6KNa \cdot 4H_2O$	AR	Sigma-Aldrich
Sodium nitroferricyanide dihydrate	$C_5FeN_6Na_2O \cdot 2H_2O$	AR	Sigma-Aldrich
Sodium hypochlorite solution	NaClO	AR,6-14% Cl_2	Sigma-Aldrich
Ammonia standard solution	NH_4Cl	1000ppm	Aladdin

Table 3-2 Equipment used in the experiments

Item	**Type**	**Supplier**
Analytical balance	SECURA324-1OIN	Sartorius
Stirring hotplates	SP88857104	Thermo-Scientific
Ultrasonic cleaner	MB-200MOD	Branson
Precision disc cutting machine	MSK-T10	MTI
Vacuum drying oven	DZF-6000	MTI
Desktop tablet press	DY-20	Strandhill
Glove box	MB-200MOD	M.Braun
Coin cell assembly machine	MSK-110D	Strandhill
Doctor blade	SZQ5-20-4	MTI
Blast drying oven	DHG-9015A	Strandhill

3.2 Design of the LMB-mimic system

This thesis aims to plate metallic Li from LiOH aqueous solution. This process is challenging because the target product, metallic Li, is chemically reactive and can be easily consumed by the water solution. To facilitate effective metallic Li deposition, the LMB-mimic system is designed and prepared to isolate the Li deposition from the water environment, as illustrated in Figure 2.25. The LMB-mimic system can be divided into two main parts: the LMB system spontaneous Li-recovery electrode, which will be explained in more details subsequently. In the LMB-mimic system, when the spontaneous Li-recovery electrode, FS-L_{1-x}MO, was immersed in the LiOH aqueous solution, Li^+ would be inserted into the electrode based on the reported spontaneous reaction, producing FS-LMO.[83] This electrode then serves as the cathode in the nonaqueous LMB system. Under the applied electric energy, Li^+ stored in the Li-recovery electrode will be released into the LMB system for efficient Li metal production.

3.2.1 Design of LMB system

LMB system is designed to provide a stable environment for the Li plating process and metallic Li. In this design, the coin cell is used as the model setup for the LMB system due to its excellent sealing property and easy fabrication. Furthermore, the coin cell is also widely used as the model device for evaluating the electrochemical performance of lithium metal batteries. For the assembly of the coin cell, the detailed procedures are shown as follows:

1. Punch the Celgard 2500 separator into a 19-mm-diameter disc.
2. Before assembling the battery, the separators discs and the coin cell caps should be washed with ethanol and thoroughly dried at 60 ℃ in the vacuum oven at ~0.1kPa overnight.
3. The components are transferred into the Ar-filled glovebox for assembly.
4. Put the $LiMn_2O_4$ electrode into the cathode caps and add two drops of electrolyte (1.0 M $LiPF_6$ in EC: EMC=3:7 vol.%) on it and then place one layer of separator on the top. Add another two drops of electrolyte, put the commercial 15.6-mm-diameter Li foil on the separator, and centralize it.
5. Put the spacer and the spring, centralize them, and then close the coin cell with the anode caps.

6. Crimp the coin cell with the crimping machine.

It is worth noting that, during the assembly operation, the H_2O and O_2 content inside the glovebox should be kept to less than 0.5 ppm. Furthermore, before testing, the coin cell should rest for 12 hours after assembly for aging.

3.2.2 Design and preparation of Li-recovery electrode

3.2.2.1 Electrochemical performance of $LiMn_2O_4$

a) Fabrication of $LiMn_2O_4$ electrode

The $LiMn_2O_4$ material samples were fabricated into electrodes by the following protocol:

1. Prepare a binder solution by dissolving polyvinylidene fluoride (PVDF) in N-Methyl-2-pyrrolidone (NMP) with the weight ratio being 1:20.
2. Weigh $LiMn_2O_4$, acetylene black, and PVDF binder solution (calculated by effective PVDF) to have a composition with a weight ratio being 8:1:1, and thoroughly mix them to form a slurry.
3. Spread the slurry onto the Al foil using a razor blade to form a uniform thin film coating.
4. Dry the slurry coating in an ordinary oven at 80°C for 1 hour to remove most of the solvent, and then transfer it to a vacuum oven (~0.1kPa) to dry at 60°C overnight.
5. Punch the dried coating into discs of 10 mm diameter, and then press them using a hydraulic compressor under ~15 MPa.
6. Transfer the electrodes into the glove box and then weigh them inside.
7. The weight of the Al foil substrate was calculated by averaging five blank Al foils. weight of the Al foil and other inert materials was subtracted to determine the active material loading in each electrode.

b) Charge-discharge Measurement

The electrochemical performance was evaluated using the assembled coin cells on the LAND-2001A battery tester at room temperature. The procedure of assembling the coin cell was almost the same but with 15.6-mm-diameter Li-foil as the anode. For the constant Li extraction capacity cycling test, the assembled coin cells were charged at a 0.2 C rate (1C=148 mA g^{-1}) for the different duration (3.5, 3.75, and 4 hours) and then discharged to the cut-off voltage of 3.0 V in the initial four cycles. After the activation, the rate is increased to 0.5C for different duration (1.4, 1.5, and 1.6 hours) and then discharged to 3.0V in the following cycling tests till the battery stops. For the constant cut-off voltage cycling, the assembled cells were galvanostatically cycled at different current rates between 3.0 and 4.3 V. To fully activate the electrochemical activity, the cell was charged and discharged at 0.2C for four cycles before being cycled at the rate of 0.5 C.

3.2.2.2 Preparation of free-standing $LiMn_2O_4$ electrode, FS-LMO

A free-standing lithium manganese oxide composite electrode, FS-LMO, was primarily designed as follows:

1. Weigh 2.000 g of $LiMn_2O_4$ and 0.250 g of acetylene carbon black and grind them with 10 mL of ethanol in the agate mortar until they are fully dispersed.
2. Add 0.416 g PTFE dispersion (60wt.% PTFE dispersed in water) dropwise into the mixture and grind them for 1 hour.
3. Transfer the slurry into the oven to dry at 80 ℃ for 1 hour to remove the ethanol.
4. Collect the LMO composite and press it into a film under the pressure of 40 MPa with the hydraulic compressor.
5. Cut the FS-LMO film into round disks with a diameter of 10 mm.
6. Finally, the FS-LMO electrode will be thoroughly dried under 80 ℃ in a vacuum oven at ~0.1kPa overnight.

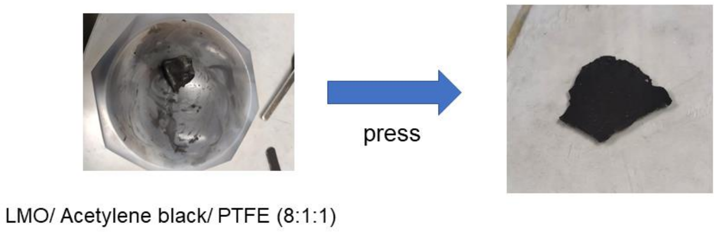

Figure 3.1 Fabrication of free-standing $LiMn_2O_4$ electrode

3.2.2.3 Electrochemical performance of FS-LMO

Electrochemical performances of FS-LMO were evaluated in the coin cell with Li foil as the anode and the FS-LMO as the cathode. The coin cell was assembled in the same steps as the previous part. Galvanostatic charge-discharge profiles of Li/FS-LMO cell cycling between 3V and 4.3V at 0.5C after the initial four cycles at 0.2 C for activation, the assembled cells were galvanostatically charged and discharged at different current rates between 3.0 and 4.3 V. For fully activation of the electrochemical cell, it was cycled at 0.2C for four cycles before charging and discharging at the rate of 0.5 C at the fifth cycle.

3.2.2.4 Preparation of Li-recovery electrode, FS-L_{1-x}MO

FS-L_{1-x}MO was prepared from the FS-LMO by electrochemical removal of lithium-ions in the coin-cell setup. For the coin cell assembly, the procedures are the same as in the LMB system. The electrochemical preparation of FS-L_{1-x}MO from FS-LMO was controlled by the Land 2001A Battery Testing System. In detail, a constant areal current density of 0.75 mA cm^{-2} was applied to the coin cell until the cut-off voltage, 4.3V, is reached. A constant voltage of 4.3 V was applied until the current reached 0.03C (1C=148 mAh g^{-1}). After fully delithiated at 4.3V, the Li recovery electrode, FS-L_{1-x}MO, can be obtained by dissembling the coin cell with the dissembling machine in the glove box. Then the FS-L_{1-x}MO was taken out from the coin cell and washed with DMC solvent three times to carefully remove the electrolyte inside the electrode and then put into the oven to remove DMC at 80 °C.

3.2.2.5 Li recovery performance of FS-L_{1-x}MO

FS-L_{1-x}MO electrodes weighing 4-5 mg cm^{-2} were selected for the Li recovery kinetics performance. The spontaneous Li recovery reaction between $Li_{1-x}Mn_2O_4$ and LiOH solution was reported to be a solid-liquid reaction.[83] To reduce the possible influence of solute concentration variation during the reaction, an excess amount of LiOH was provided by a 500-mL of 0.1M LiOH solution. Due to the limited amount of Li that can be recovered by the FS-L_{1-x}MO electrode, the concentration of the solution can be taken as unchanged. To keep a stable concentration near the electrode, the solution was stirred during the reaction to reduce the possible influence of concentration gradient caused by localized LiOH consumed near the electrode. Moreover, the detailed steps for the Li recovery kinetic curve are described as follows:

1. Before the Li recovery reaction, the FS-L_{1-x}MO electrode was kept in the de-ionized water for at least 30 min for wettability.
2. The electrode was held by a tweezer and immersed in the LiOH solution stirred at 100 rpm. Once the electrode was immersed, timing started.

3. Keep the electrode immersed in the solution for various duration (0, 0.5, 1, 2, 4, 8, 16, 20, 30, and 60min). It could be observed that during Li recovery, some bubbles were produced quickly on the surface of the electrode.
4. After the targeted Li recovery duration, remove the electrode from the LiOH quickly and end the reaction by immersing it in the de-ionized water under stirring.
5. Wash the electrodes after Li recovery three times with the de-ionized water, dry them at 80 ℃ for 4 hours, and then transfer them to the vacuum oven for further drying at 60 ℃ and ~0.1kPa overnight.
6. Assemble the coin cell as the steps in the previous LMB system section, charging the cell under 0.05 C till 4.3V.
7. Li plating capacity after Li recovery was plotted against the recovery duration.

3.3 Li plating by the LMB-mimic system

3.3.1 Li recovery from LiOH solution

The spontaneous Li-recovery electrode, FS-L_{1-x}MO, with different mass loadings of $Li_{1-x}Mn_2O_4$, was immersed in 500 mL of 0.1 M LiOH for 30 min to ensure the electrode was fully lithiated. After Li^+ intercalated, the obtained FS-LMO was washed with distilled water three times to remove the possible LiOH on the surface. After being washed, the electrode will be dry in an oven at 80 ℃ for 1 hour to remove most of the water. Then the electrode will be thoroughly dried in a vacuum oven at 70 ℃ and at ~0.1kPa overnight. Then the electrode serves as the cathode and is fabricated into a coin cell according to the steps in the LMB system.

Spontaneous Li recovery can be described as:

$$\mathrm{FS-L_{1-x}MO(s) + LiOH(aq) \rightarrow FS-LMO(s){+}H_2O(l) + O_2(g)} \qquad 3\text{-}1$$

3.3.2 Li plating for metallic Li production

Metallic Li can be obtained by dissembling the coin cell with the dissembling machine in the glove box. To obtain the metallic Li, a constant areal current density of 0.75 mA cm^{-2} was applied to the coin cell until the cut-off voltage reached the value of

4.3 V. Following that, a constant voltage of 4.3 V was applied until the current reached 0.03 mA to ensure the electrode was entirely delithiated in this voltage state. Then the lithium-deposited Cu foil was taken out from the coin cell and washed with DMC solvent three times to carefully remove the electrolyte and then put into the oven under 80 ℃ to remove DMC. The FS-L_{1-x}MO will also be washed with DMC and dried for the next Li recovery-plating cycle.

Li plating: $$\mathrm{FS-LMO(s)} \overset{e^-}{\rightarrow} \mathrm{FS{-}L_{1-x}MO(s)} + \mathrm{Li^0(s)} \tag{3-2}$$

3.3.3 Li recovery-plating cycling performance

For the Li recovery-plating cycle test, an FS-L_{1-x}MO electrode with active mass loading of 20 mg was reused to repeat the cycle 20 times. Both the operation conditions of the Li recovery and plating are the same in this part. It is worth noting that during the cycles, few bulges will be exhibited on the surface of the bulk free-standing electrode due to the gas production in the Li extraction process. An additional pressing procedure with 10 MPa is required to compact the electrode.

3.4 Nitridation of Li

A homemade tube reactor was designed to accurately control the nitridation temperature and avoid possible exposure to air. The reactor mainly consists of a flange-sealed tube (Figure 3.2), flowmeter (0-200 sccm), heating coil, pump oil bottle, and gas tube.

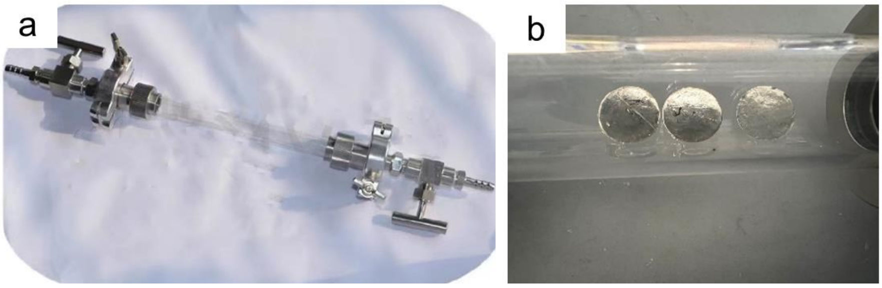

Figure 3.2 (a) flange-sealed tube (b) commercial Li foil under nitridation

The details of the nitridation of Li are described as follows:

1. Before nitridation, gas leakage detection should be simply operated, and the flange-sealed tube should be dried at 80 ℃ in the oven overnight to remove

possible absorbed water.

2. Connect the input gas tube to the N_2 bottle and open the gas bottle valve for at least 30 min to remove the possible air inside the equipment before reaction.
3. Transfer the flange-sealed tube into the Ar-filled glovebox and put the Li sample into the tube. Before being taken out from the glove box, the input and outlet valves should be closed.
4. Connect the flange-sealed tube to the gas and put it into the oven. Set the target temperature by the temperature controlling system of the oven.
5. After heating for at least 30min, open the two valves of the flange-sealed tube to make the nitrogen gas flow through the whole system, then start recording the reaction time. In the present study, the N_2 gas supply is kept at a constant flow rate of 100 sccm.
6. During the process, the output gas tube should be placed beneath the pump oil surface to isolate the reactor from the ambient atmosphere.

3.4.1 Nitridation of commercial Li foil

The designed reactor used commercial Li foil (10mm in diameter, ~30 mg) to react with nitrogen gas (99.999 %). Nitridation of different Li foils was carried out at several temperature levels (25, 50, 75, and 100 °C) in an N_2 atmosphere for 1 hour. And then, new Li foils were used to perform nitridation at 100 °C for several durations (0, 30, 40, 50, 80, 90, and 120 min). From the experimental result, the nitridation at 100°C shows the most considerable conversion rate from Li to Li_3N.

3.4.2 Nitridation of Li deposits from LMB-mimic system

The Li deposits, plated by the LMB system, were also tested in the flange-sealed tube for nitridation outside the glovebox, with the same procedures as nitridation of commercial Li metal in Section 3.4. Li deposits with different theoretical areal deposited capacities (>10mAh cm^{-2}) were obtained by the Li recovery-plating in the LMB-mimic system. The deposits were put into the designed nitridation reaction at 100°C for 4 hours for full nitridation. Li deposits at the theoretical areal capacity of 20 mAh cm^{-2} were used for nitridation at 100°C for several duration to study the kinetics. Because nitridation product, Li_3N, is easy to react with H_2O in air. After nitridation, all the products should be transferred and kept in the glove box to avoid possible contact with the ambient air.

3.5 NH_3 formation

Li_3N reacting with H_2O is a rapid but non-violent reaction, producing water-soluble ammonia, $Li_3N+H_2O \rightarrow NH_3+LiOH$. For the ammonia formation, take the nitride out of the glovebox and put it into a glass bottle (100 mL in volume) containing 50 mL of de-ionized water. Seal the bottle till the reaction disappeared. Then transfer the product solution into a 250 mL volumetric flask and dilute it till the mark line. Each time before putting the nitride into the volume flask, 10 mL of de-ionized H_2O was taken out from the flask as a bare reference for the following quantification. Moreover, the final concentration of ammonia was calculated by removing the part from the blank reference.

3.6 Ammonia quantitation

To reliably detect and quantify the ammonia, a modified version of the indophenol colorimetric test based on salicylate is employed, which has been used in many reports of ammonia synthesis.[20, 84, 85] The salicylate method has the advantage of avoiding toxic reagents (such as phenol in the Indophenol method, and mercury salts in the Nessler Method) and also does not generate toxic fumes (such as ortho-chlorophenol produced by the Indophenol method).[86] Furthermore, it is reported that the result of salicylate method is also stable when quantifying the ammonia in alkaline solution.[84] Since the sample ammonia solution mainly containing (LiOH, NH_3) after hydrolysis, the salicylate method is suitable for quantifying the ammonia concentration in the present study without any pH adjustment.

The salicylate method is one of the available colorimetric ammonia quantification techniques based on the Berthelot reaction (Eq. 3-3).[87] It involves the interaction of ammonia with phenol and hypochlorite in an alkaline solution to produce a blue-colored indophenol product. These indophenol-like products will turn from green to blue color with the increasing sample ammonia concentration, and strongly absorb visible light between 630 nm and 720 nm. The maximum absorbance of the indophenol product (located at ~655 nm.) by the UV-Vis spectroscopy has a linear relationship with its concentration, which allows ammonia quantification to sub-ppm levels using ultraviolet-visible (UV-Vis) spectroscopy. Typically, in the salicylate method, sample ammonia concentration is determined by comparing with the ammonia standard curves, plotted by the UV absorbance with the known ammonia concentration. It has been reported the salicylate method is accurate for ammonia quantification above 0.2 mg L^{-1}.[85]

$$2C_7H_5O_3^- + NH_3 + 3ClO^- \xrightarrow{\text{catalyst}} C_{14}H_8O_6N^- + 2H_2O + OH^- \qquad 3\text{-}3$$

(a) Operation steps for salicylate method

For the spectrophotometric analysis, three reagents were prepared:

Coloring solution: 5 g of potassium sodium tartrate and 5 g of sodium salicylate dissolved in 100 mL of 1 M NaOH.

Oxidation solution: 5.83 mL of sodium hypochlorite (available chlorine 6-10%) was added into 100 mL of de-ionized water.

Catalyst solution: 0.2 g of sodium nitroferricyanide was diluted to 20 mL of de-ionized water.

The 4 mL coloring solution was added to the 4 mL ammonia-containing solution. Then, 400 uL of catalyst solution and 2 mL of oxidation solution were successively added to the above solution. Shake the mixture solution gently to make the solution well mixed. After the solution stand still for 2 hours, absorbance measurements were performed in a 10 mm quartz cuvette at a wavelength of ~655 nm. The same procedure was applied for several standard solutions (0, 0.5, 1, 2, 3, 4 ppm) to create a calibration curve. It is worth noting that the NH_3 concentration should be well situated in the range of the standard curve and large than 0.2 ppm for more accurate qualification. Moreover, each result was obtained by removing the absorbance value of background de-ionized water.

(b) Standards curves

To build up the standard curve, ammonia standard solution with known concertation (0,0.5,1,2,3,4 mg L^{-1}) were treated with the salicylate method. It can be observed from the inset graph in Figure 3.3b, with the increasing ammonia concentration of standard solution, the color of product solution became bluer from green, which indicated that more indophenol products were produced. And in the meanwhile, as illustrated in Figure 3.3a, the UV-absorbing curves exhibited the maximum absorbance in the same characteristic position of 655.5 nm, which belonged to the indophenol product.[86]

In details, when the ammonia concentration equal to zero, there is nearly no UV absorbance. When the concentration increased from 0 to 4 mg L^{-1}, the value of absorbance would increase gradually. Thus, it can be confirmed, the indophenol products were derived from the ammonia through salicylate method and the UV absorbance of the product is related to the concentration of ammonia. By plotting the relationship curve of the maximum absorbance and the standard ammonia concentration, (Figure 3.3b), these two variables exhibited a linear relationship, and by linear fitting, it can be observed the absorbance and the ammonia concentration obey the typical linear relationship with a R^2=0.99978 close to 1, which is consistent with the report.[85] Thus, the linear relationship can be used for quantifying the sample ammonia under the similar condition to the standard solution, by the salicylate method. And for an accurate result, the sample ammonia concentration should be within 0.2-4 mg L^{-1}.

$$\text{Absorbance} = 0.536 * [\text{ammonia concentration}] + 0.001$$

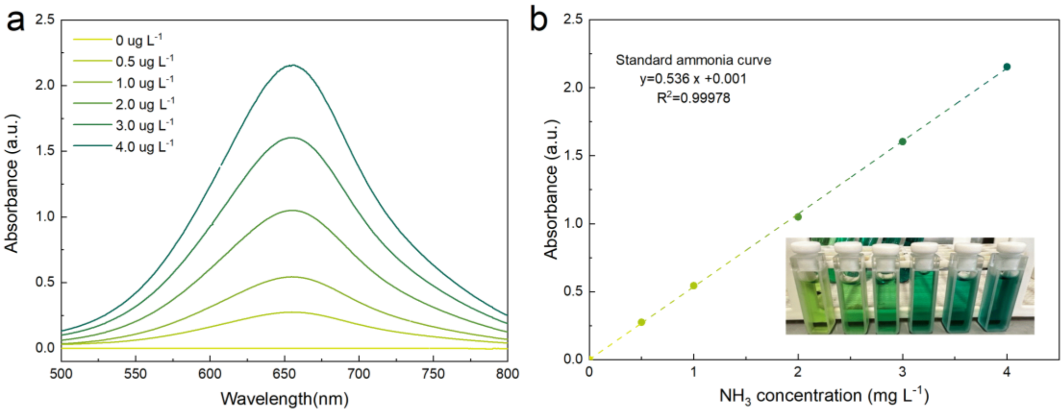

Figure 3.3 (a) UV-vis absorption spectra and (b) corresponding calibration curves for colorimetric NH_3 assay using the indophenol blue method.

3.7 Analytical methods

3.7.1 Ultraviolet-visible (UV-Vis) spectroscopy

Ultraviolet-visible spectrometry is employed to identify, characterize, and quantify a remarkable wide range of molecular compounds. When a material is irradiated with light, absorption occurs when the energy of incident light is equal to the energy difference (ΔE) between a molecule's ground and excited states， as demonstrated in Figure 3.4.

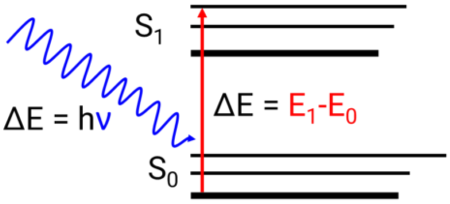

Figure 3.4 Excitation of an electron from the ground state (S_0) to the excited state (S_1).

Absorbance measurements are frequently used to quantify an unknown sample's concentration by exploiting the Beer-Lambert Law, which describes how light is attenuated based on the materials it passes through. The transmittance and absorbance are directly proportional to the concentration of samples, c, molar absorptivity, ε, and cuvette pathlength, l.

$$A = \varepsilon\ c\ l \tag{3-4}$$

Consequently, the amount of light absorbed by the sample depends on the number of molecules interacting with it. The more concentrated a sample is, the more molecules are present and the higher the absorbance. In this thesis, a beam with a broad wavelength from 500 nm to 800 nm will pass through the solution for absorbance measurements. In this process, the molecules in the sample will absorb the light, and the electrons will be excited. At ~655 nm, the energy of incident light equals the energy difference (ΔE) of the blue-color product from the salicylate method. Thus, the absorbance at the position could reach its highest value. Moreover, the absorbance at this location is directly proportional to a sample’s concentration, which equals to the concentration of ammonia in the sample. Thus, ultraviolet-visible absorption can be used to quantify ammonia with the salicylate method.

3.7.2 X-ray diffraction diffractometer (XRD)

The crystal structural information of samples in this study was identified using an X-ray diffraction diffractometer (XRD, Rigaku SmartLab) equipped with a Cu Ka radiation source (wavelength of 1.540562 Å) and graphite monochromator. The applied current and voltage were 20 mA and 45V during the XRD test. The scanning range (2θ) varies from 10 to 70˚. The scanning time and step size were two and 0.05˚ seconds, respectively. The obtained spectra were analyzed by the Joint Committee on Powder

Diffraction Standards (JCPDS) cards defined by the International Center for Diffraction Data. Due to high reactivity to some components in the air (e.g., H_2O, O_2, N_2, etc.), the samples (Li, Li_3N, LiOH) should be isolated from the air during XRD scanning. Herein, an in-situ XRD setup (Figure 3.5), sealed with a Be window, was used for routine XRD test of those air-sensitive samples due to its excellent sealing property and good X-ray transmission.

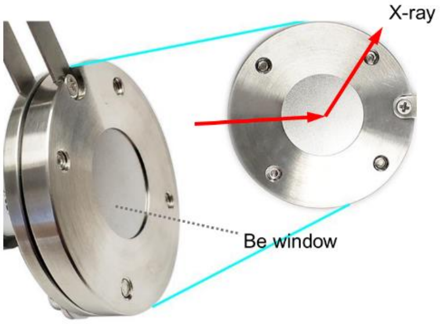

Figure 3.5 in-situ XRD setup sealed with a Be window

3.7.3 Scanning electron microscopy (SEM)

The scanning electron microscopy (SEM) technique adopts a focused, high-energy electron beam to measure the surface morphology and chemical composition samples. In this dissertation, SEM (Tescan VEGA3) was used to observe the morphology of samples in surface and cross-section. To transfer some reactive samples (e.g., Li metal, Li_3N) from glovebox for SEM test, a homemade vacuum transfer box was used to isolate them from the atmosphere. The gold coating was required to enhance the conductivity of the samples for high quality imaging.

3.7.4 X-Ray Photoelectron Spectroscopy (XPS)

XPS is one of the most widely used surface analysis techniques to provide information about the elemental composition and speciation of the near-surface region (1-10 nm) of any solid substrate [88] During operation, the sample is irradiated with incident X-rays under ultra-high vacuum, leading to the emission of inner shell electrons (Figure 3.6). These emitted photoelectrons possess binding energies specified to the elements they originated from and their chemical states. Consequently, XPS allows quantitative analysis of the surface composition, different oxidation states, and chemical environments.

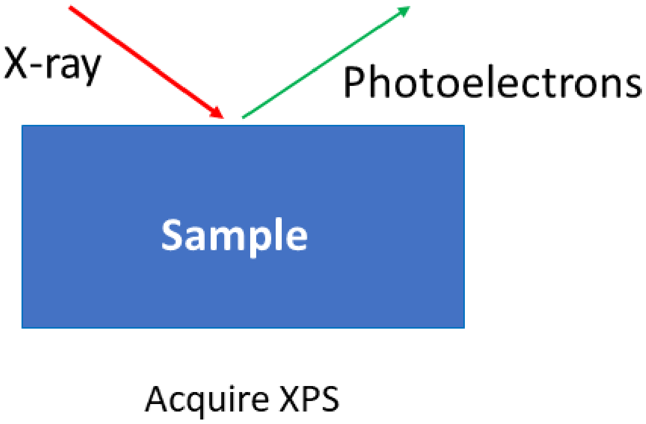

Figure 3.6 Schematic XPS measurement on the surface of sample.

The in-depth XPS profiling is a characterization technique to obtain the bulk composition information near the surface. It can be regarded as the combination of fundamental XPS measurement and the sputtering. During its operation, as illustrated in Figure 3.7, the equipment uses a bunch of ion beam (usually Ar^+ beam) to etch the surface layers and remove them. Following that, the XPS spectrum will be acquired to record the composition information of the new exposed surface. Combining multiple cycles of ion beam etching and XPS measurement, the bulk information near the surface of the original sample could be obtained. These sequences of etching and acquiring XPS spectra would be repeated until the profiling has reached the target depth. During the profiling, the target depth was set with the reference of some substrates (usually Si, SiO_2, and TaO_2, etc..) with known profiling information. These substrates have repeated and reliable etching depth with the same etching condition. Thus, during XPS profiling of the sample, the target depth can be presumed with these substrates as the references. Usually, the target depth is set by controlling the etching time and etching speed (depth/time), with the reference to these known substrates.

In this study, all the XPS data were obtained by X-ray photoelectron spectroscopy (XPS, Thermo Scientific Nexsa) using a monochromatic Al K(alpha) X-ray source calibrated with respect to carbon (284.8 eV) at 15 kV. The chamber pressure was kept $<1.33\times10^{-6}$ Pa during all measurements. Before characterizing the electrode dissembled from LMB, the electrode should be rinsed with DMC solvent three times to remove the residual Li salt, followed by drying in the glovebox for 12 h at room temperature to remove the solvent residual. The X-ray photoelectron spectra (XPS) depth profiles were conducted to study the composition of SEI on deposited Li by applying different sputtering times of 0 min, 2 min, and 4 min (50nm min^{-1} relative to TaO_2), respectively. Peak fitting was performed using XPSPEAK 4.1 software. For transferring the air-sensitive samples, a vacuum transfer module was used.

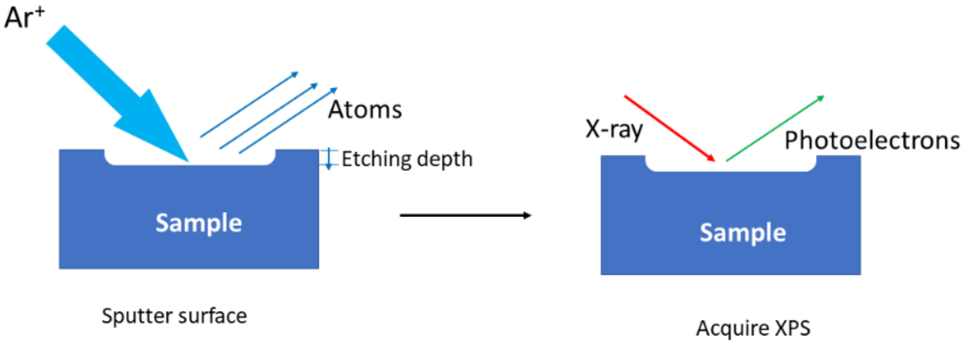

Figure 3.7 Schematic process of in-depth XPS profiling on measuring sample.

Chapter 4 Result and Discussion

4.1 Introduction

The motivation for developing the LMB-mimic strategy is to continuously produce ammonia from N_2 and H_2O under ambient temperature and atmospheric pressure. As demonstrated in Figure 4.1, in the Li-mediated ammonia synthesis, metallic Li is used to provide a highly reactive surface to spontaneously split the stubborn N_2, forming a high-energy precursor, lithium nitride. And then, Li_3N readily reacts with water to produce ammonia. In the meanwhile, LiOH will be formed. To continuously produce ammonia under ambient conditions, a cyclic LMB-mimic strategy is proposed to plate Li metal from the LiOH aqueous solution. In the LMB-mimic system, Li^+ in the LiOH aqueous solution will be first spontaneously extracted by FS-L_{1-x}MO, forming FS-LMO. After Li recovery, the FS-LMO will serve as the cathode of lithium-ion battery. With the electric energy applied, Li^+ will be released as Li metal upon charging of the battery. Finally, FS-LMO will be regenerated to form FS-L_{1-x}MO for another cycle.

To continuously produce ammonia in the Li-mediated ammonia synthesis, the LMB-mimic system should be stable for Li recovery and plating cycles. In the present design, the condition of the LMB system and LiOH aqueous solution are unchanged. Therefore, the Li-recovery electrode containing LMO should be well designed for stable and efficient Li plating. Based on the designed Li-recovery electrode, optimal Li plating parameters will be tuned for high Li plating efficiency. After exploring the optimal parameters, both commercial Li foil and Li plated by LMB-mimic system will be used for ammonia production.

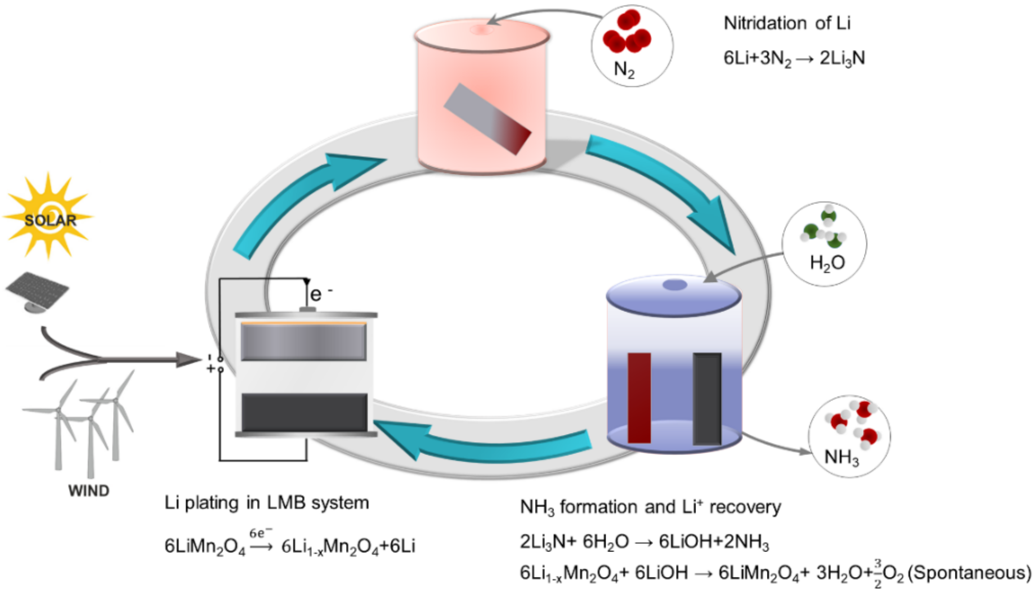

Figure 4.1 Illustrations of sustainable Li-mediated ammonia production by our LMB-mimic strategy.

4.2 Design of Li-recovery electrode

4.2.1 Thermodynamic study of the spontaneous Li recovery by $Li_{1-x}Mn_2O_4$

Although the spontaneous Li recovery has been reported in literature,[83, 89, 90] it is still unclear whether $Li_{1-x}Mn_2O_4$ could be fully converted to $LiMn_2O_4$. Thus, based on the early reports, a thermodynamic study will first be carried out on the spontaneous Li-recovery reaction.

Following Dahn's study, the voltage, V (x), of the Li/Li_x (host) intercalation cell is

$$V(x) = -\frac{1}{e}(\mu_{Li}^{int}(x) - \mu_{Li}^{0}) \qquad 4\text{-}1$$

Where e is the magnitude of the electron charge, μ_{Li}^{int} (x) is the chemical potential of Li interacted in the LICs, and $\mu_{Li}^{0}$is the chemical potential of Li in Li. The LICs are placed in the LiOH aqueous solution. Assuming that there are so many compounds relative to the solution that x does not change significantly when the compound reacts with O_2 or H_2O, hence, $\mu_{Li}^{int}(x)$ does not vary. In equilibrium,

$$Li^{+} + OH^{-} \leftrightarrow Li\ (\text{interacted}) + \frac{1}{2}H_2O + \frac{1}{4}O_2 \qquad 4\text{-}2$$

It is presumed that during Li interaction, few bubbles of O_2 will evolve over the surface of Li_x(host), so the state of O_2 should be under near 1-atmosphere pressure, in its standard state. Thus,

$$\mu_{Li^{+}} + \mu_{OH^{-}} = \mu_{Li}^{int}(x)_{eq} + \frac{1}{2}\mu_{H_2O}^{0} + \frac{1}{4}\mu_{O_2}^{0} \qquad 4\text{-}3$$

$\mu_{H_2O}^{0}$ and $\mu_{O_2}^{0}$ are the chemical potential of water and O_2 in its standard state, $\mu_{Li^{+}}$and $\mu_{OH^{-}}$ are the chemical potentials of Li^+ and OH^- in solution, respectively. In the solution, charge conservation requires that

$$[Li^{+}] + [H^{+}] = [OH^{-}] \qquad 4\text{-}4$$

$[Li^+]$ and $[H^+]$ are the concentration of Li^+, H^+ in the LiOH aqueous solution. Because the solution is alkaline, one can assume

$$[Li^{+}] = [OH^{-}] >> [H^{+}] \qquad 4\text{-}5$$

The chemical potential of OH^- and Li^+ can be obtained by the Nernst equation assuming the complete dissociation of LiOH in water

$$\mu_{Li^+} = \mu^0_{Li^+} + kT\ln[Li^+] \qquad 4\text{-}6$$

$$\mu_{OH^-} = \mu^0_{OH^-} + kT\ln[OH^-] \qquad 4\text{-}7$$

Where $\mu^0_{Li^+}$ and $\mu^0_{OH^-}$ are the chemical potentials of Li^+ and OH^- in standard state in 1M LiOH solution. k is Boltzmann's constant, and T is the temperature in Kelvin. Combining the above equations, the voltage of the electrode where the spontaneous Li recovery reach equilibrium,

$$V(x)_{eq} = \frac{1}{e}\left\{\mu^0_{Li} + \frac{1}{2}\mu^0_{H_2O} + \frac{1}{4}\mu^0_{O_2} - \mu^0_{Li^+} - \mu^0_{OH^-} - kT\ln[Li^+] - kT\ln[OH^-]\right\} \qquad 4\text{-}8$$

In the equation, $\mu^0_{Li} + \frac{1}{2}\mu^0_{H_2O} + \frac{1}{4}\mu^0_{O_2} - \mu^0_{Li^+} - \mu^0_{OH^-}$ is minus the partial molar free energy change for the reaction, $Li^+ + OH^- = Li^0 + \frac{1}{2}H_2O + \frac{1}{4}O_2$, and the value is -3.446 eV/atom. Thus,

$$V(x)_{eq} = \frac{1}{e}\{3.446 - kT\ln[Li^+] - kT\ln[OH^-]\} \qquad 4\text{-}9$$

In the present case, the concentration of LiOH is 0.1M. Thus $[Li^+] = [OH^-]$=0.1 M. And at room temperature, kT =0.026 eV. Thus, the electrode potential when the spontaneous Li recovery reaches equilibrium,

$$V(x)_{eq} = (3.446 - 2kT\ln 0.1)\ V = 3.565\ V \qquad 4\text{-}10$$

As illustrated in Figure 4.2, for any $Li_{1-x}Mn_2O_4$ (0<x<1), its theoretical Li intercalation potential, V(x), is always larger than $V(x)_{eq}$. That is, V(x)> $V(x)_{eq}$, from Eq. 4-1,

$$\mu^{int}_{Li}(x) < \mu^{int}_{Li}(x)_{eq}$$

Combining with 4-3 and 4-11,

$$\mu_{Li^+} + \mu_{OH^-} > \mu^{int}_{Li}(x) + \frac{1}{2}\mu^0_{H_2O} + \frac{1}{4}\mu^0_{O_2}$$

Then, for any $Li_{1-x}Mn_2O_4$ (0<x<1), the Gibbs free energy for the Li recovery,

$$\Delta_r G_m = \mu^{int}_{Li}(x) + \frac{1}{2}\mu^0_{H_2O} + \frac{1}{4}\mu^0_{O_2} - (\mu_{Li^+} + \mu_{OH^-}) < 0 \qquad 4\text{-}11$$

Therefore, the $Li_{1-x}Mn_2O_4$ (0<x<1) will spontaneously extract Li^+ from solution until fully converted to $LiMn_2O_4$.

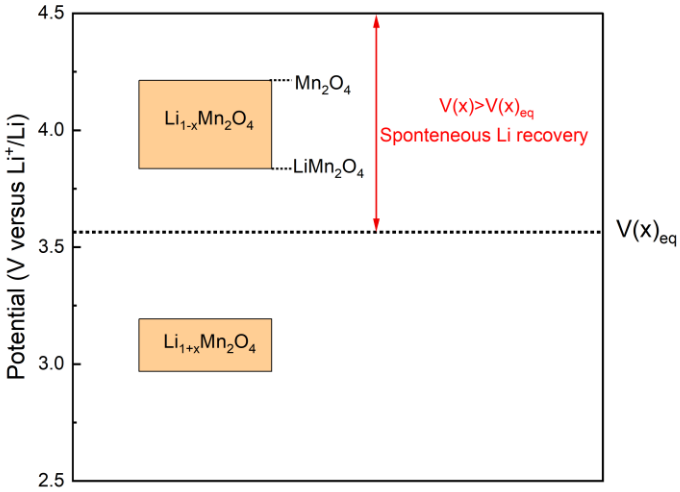

Figure 4.2 The theoretical Li^+ intercalation potential of $LiMn_2O_4$ electrodes and the electrode potential where Li^+ is spontaneously extracted. (Adapted with permission.[91] Copyright 2010, Springer Nature)

4.2.2 Exploration of reversible x in $Li_{1-x}Mn_2O_4$

From the previous thermodynamic study, in the Li recovery process, $LiMn_2O_4$ can be formed from $Li_{1-x}Mn_2O_4$ by intercalating x Li^+ into the tetrahedral sites of the spinel manganese oxide. Moreover, in the Li plating process, Li metal will be produced by de-intercalating xLi^+ from the tetrahedral sites of $LiMn_2O_4$, forming $Li_{1-x}Mn_2O_4$. Therefore, to stably plate Li metal through the LMB-mimic system, $LiMn_2O_4$ should deliver a reversible Li^+ intercalated/de-intercalated capacity of x. And because the reversible capacity of xLi^+ is also related to the amount of Li metal plated through the Li recovery-plating cycle, the value of x should be as large as possible in order to plate as much as possible metallic lithium per cycle. Therefore, to efficiently and stably plate Li metal through the LMB-mimic system, it is required to find the upper limit of x value for a reversible and stable xLi^+ release from $Li_{1-x}Mn_2O_4$.

4.2.2.1 Constant Li extraction capacity cycling

To evaluate the reversible capacity of $LiMn_2O_4$, a constant Li extraction capacity cycling test of the Li/ $LiMn_2O_4$ cell will be carried out. This test is composed of continuous multiple cycles of charging and discharging process in Li/ $LiMn_2O_4$ cell with constant charging capacity. In the charging process of the test, a constant amount of x Li^+ will be de-intercalated from the tetrahedral sites of $LiMn_2O_4$.The Li^+

intercalation into $LiMn_2O_4$ in charging is the same as the one in Li plating step of the LMB-mimic system. And in the discharging process, Li^+ will be intercalated back into the tetrahedral sites, which is the same as the one in Li recovery step. Therefore, it is reasonable to use the constant Li extraction capacity cycling in the Li/ $LiMn_2O_4$ cell to evaluate the reversible Li^+ de-/intercalation capacity of the Li-recovery electrode.

The constant Li extraction capacity cycling performance of $LiMn_2O_4$ is implemented in the Li metal half-cell with a $LiMn_2O_4$ composites electrode as the cathode. In lab-scale research, the Li metal half-cell is frequently utilized for evaluating the electrochemical performance of cathode material,[92] including cycling performance. Because the reversible Li^+ in $LiMn_2O_4$ only involves the Li^+ intercalation/de-intercalation in the tetrahedral sites, the lower cut-off voltage is therefore set at 3V as reported.[93] Therefore, the constant Li extraction capacity cycling is performed in the Li half-cell by selecting different Li extraction capacities of x=0.7, 0.75, and 0.8. This is based on the theoretical capacity of ~148 mA h g^{-1} in $LiMn_2O_4$. In detail, the half-cell is cycled by charging until the cut-off Li extraction capacity of x=0.7, 0.75, 0.8 and then discharging them to 3.0 V. If the electrode has excellent reversibility and stability for xLi^+, it should have a value of discharging capacity closed to the set constant charging capacity for as many cycling as possible. For a more direct result, Coulombic efficiency (CE) can also be obtained to evaluate its reversibility in each cycle because CE is equal to the ratio of discharging capacity over charging capacity. If the battery can hold a high CE close to 1 for as many cycles as possible, then the electrode possesses good reversibility and stability.

As illustrated in Figure 4.3, the CE and discharging capacity of $LiMn_2O_4$ with various constant Li extraction capacity cycling of x=0.7, 0.75, and 0.8 are compared for 200 cycles. In the first several cycles, the CE and discharging capacity of these electrodes with different x will increase gradually to a relatively stable value because during the activation under a small current, the Li^+ pathway will be gradually built up, and the Li^+ in the system begin to participate in the intercalation/de-intercalation process. For x=0.8 (charging capacity, cc=118.4 mAh g^{-1}), the electrode exhibits a stable CE of ~97.5% and discharging capacity of 115 mAh g^{-1} from the 5th to 27th cycles. In the following cycling, the CE gradually decreases with discharging capacity. Even in the final several cycles, the value increases a little again. And the battery fails and stops at the 47th cycle. For x=0.75 (cc=111 mAh g^{-1}), a stable CE around 99.13%

and discharging capacity of 109.9 mAh g^{-1} for around 150 cycles (from 5th -155th cycles), and then both values will decline gradually until they are stopped. And for the electrode of x=0.70 (cc=103.6 mAh g^{-1}), throughout the 200 cycles after activation (around 195 cycles), it delivers a highly stable CE of 99.56% and discharging capacity of 103.52 mAh g^{-1} and never shows any decrease. Because of the increased charging capacity, the electrode will become more unstable, and a possible side reaction will occur if x is beyond a certain value.[94] Therefore, to design a stable electrode for Li^+ intercalation/de-intercalation for over 150 cycles, the constant Li extraction capacity, x, cannot be larger than 0.75. Consequently, for designing a stable and efficient Li-recovery electrode in the present LMB-mimic system, the maximum Li extraction capacity from $LiMn_2O_4$ is set less than 0.75 Li^+.

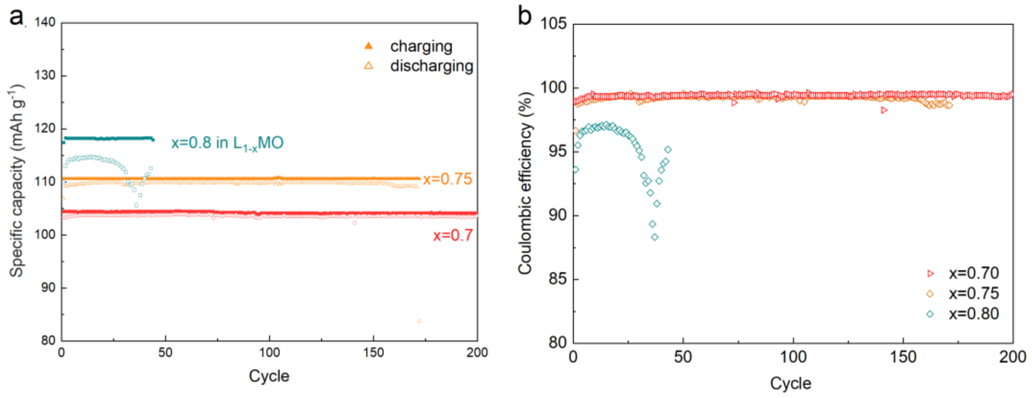

Figure 4.3 (a) Cycling performance of Li/ $LiMn_2O_4$ cell in 200 cycles under constant Li extraction capacity of x in $Li_{1-x}Mn_2O_4$ from 3.0 V at 0.5C after the initial 4 cycles at 0.2C for activation and (b) the Coulombic efficiency ($mLiMn_2O_4$=1.5 mg cm^{-2}).

4.2.2.2 Constant cut-off voltage cycling

Constant cut-off voltage cycling is another electrochemical performance test mode to evaluate electrode material's stability and reversible capacity. It is more commonly used than the constant Li extraction capacity cycling in practical lab-scale electrochemical performance evaluation. The test is also operated by charging and discharging the Li/ $LiMn_2O_4$ cell for long cycles. Hence, it also can be utilized to evaluate the maximum amount of x for reversible Li^+ de-/intercalation of $LiMn_2O_4$, as the test of Li extraction capacity cycling does. Furthermore, for battery performance tests, it is much simpler to directly set the cut-off voltage than the Li extraction capacity calculated from the active mass inside the electrode.

Therefore, if the electrode can deliver a large reversible capacity, in the constant cut-off cycling test, it should have a CE close to 1 for every cycle, and in each cycle, both the charging and discharging capacity (cc, dc) should be maintained at high values. Because CE= cc/dc and the cc directly determines the amount of Li plating, the charging capacity should be maintained at a large value for cycles. Referring to the reported research,[95], the commonly used upper cut-off voltage is 4.3 V, and the Li^+ is intercalated/de-intercalated in the tetrahedral sites above 3V. Thus, the cut-off voltage ranges from 3V to 4.3V. Consequently, if the electrode can exhibit a CE~1 and large charging capacity in every charging/ discharging cycle in the range of 3-4.3V, the electrode will have an excellent large reversible capacity.

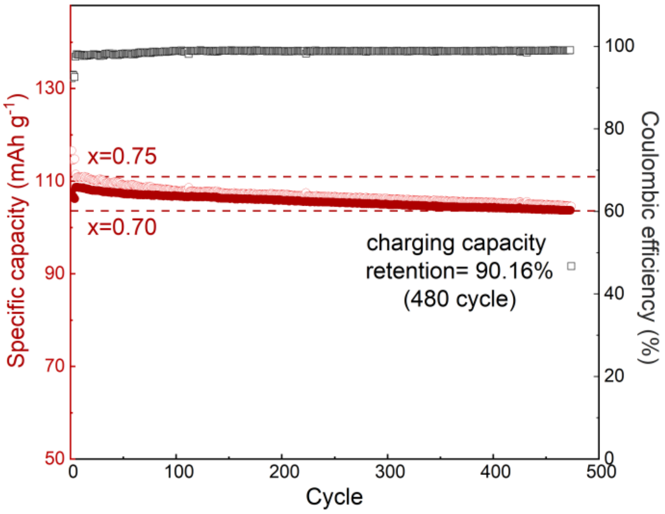

Figure 4.4 Long-term cycling performance and the corresponding coulombic efficiency of Li/ $LiMn_2O_4$ cell under the cut-off voltage of 3-4.3V during 470 cycles at 0.5 C after the initial four cycles at 0.2C for activation ($mLiMn_2O_4$=1.5 mg cm^{-2})

The cycling performance of the Li/ $LiMn_2O_4$ cell with the constant cut-off voltage from 3V to 4.3V at 0.5 C is illustrated in Figure 4.4. After the activation process in the first several cycles, the electrode exhibits a stable CE value of above 99% from 5th cycle to 470th cycle. And charging capacity of $LiMn_2O_4$ slowly decreases from 0.753Li^+ (111.5mAh g^{-1}) in the 5th to 0.710 Li^+ (105.2mAh g^{-1}) in the 470th cycle, with a decrease rate of 9.25×10^{-5} Li^+ per cycle. The high CE of over 99% in every cycle means the electrode can deliver excellent Li^+ intercalation/de-intercalation reversibility. The charging capacity can be maintained in the range of 0.71-0.75 Li^+ for more than 465 cycles, which means $LiMn_2O_4$ has a large and reversible Li intercalation/de-intercalation capacity under the constant cut-off voltage cycling. Hence, the constant cut-off voltage (3-4.3V) can be used stably and reversibly for a large xLi^+. Consequently, the constant cut-off voltage (3-4.3V) will be adopted for stable and efficient Li plating in subsequent LMB-mimic system tests.

4.2.3 Fabrication of Li-recovery electrode from $LiMn_2O_4$

4.2.3.1 Free-standing Li-recovery electrode

In the previous section, to evaluate the electrochemical performance of $LiMn_2O_4$, a thin electrode with a small loading of $LiMn_2O_4$ (~1.5 mg cm^{-2}) is fabricated by the industrial slurry-casting method. Typically, the electrode is prepared by mixing active materials, conductive carbon, and the binder in a solvent to form a slurry, which is then cast onto a current collector, followed by a drying process. In the present LMB-mimic system, for efficiently plate Li metal, it is expected to increase the active loading of $Li_{1-x}Mn_2O_4$ to extract more Li^+ in each Li recovery-plating cycle. Nevertheless, the slurry-casting method is not suitable for obtaining a high-loading electrode. In order to prepare a homogeneous slurry for the slurry-casting method, PVDF as the binder should first be dissolved in NMP solvent, then mixed with active material and the conductive carbon. Moreover, the binder could migrate and concentrate at the surface with solvent evaporation in the drying process. After drying, the inhomogeneous distribution of binder will form in the electrode.[96] For large-loading electrode fabrication, the slurry for drying will be even thicker. And the inhomogeneous distribution will become more severe, causing delamination of active materials from the current collector and breakdown of the electrode. Therefore, it is important to explore an alternative method to fabricate electrodes with a high loading of $LiMn_2O_4$.

Instead of the traditional soluble binder, a fibrillizable polymer, PTFE, will be used to make a high-loading electrode. Under high shear, PTFE can be stretched to form fiber and act as a net to support active material and conductive additives. It has been reported that PTFE can be the binder for cathode fabrication in both aqueous and organic LIB.[97, 98] furthermore, the PTFE-based electrode fabrication has been commercialized by Maxwell Technologies and is compatible with the current commercial LIB production line.[99] Since the present LMB-mimic system is expected to plate Li metal on a large scale, the free-standing PTFE electrode with a simple fabrication method is adopted after some modification from the reported work.[91]

4.2.3.2 Characterization

To characterize the crystal structure of pristine $LiMn_2O_4$ before and after fabrication into FS-LMO and FS-L$_{1-x}$MO, the XRD patterns of the selected samples are shown in Figure 4.5a. Both pristine $LiMn_2O_4$ powder and the FS-LMO correspond well to JCPDS data No. 35-0782, having spinel structure with Fd-3m (227) space group. It can also be apparently seen from the graph that the structure of the electrodes prepared using a PTFE binder does not denature the crystalline structure of $LiMn_2O_4$. As observed from the digital image in Figure 4.5 b, $LiMn_2O_4$ was fabricated into a piece of an integral membrane of the free-standing electrode, FS-LMO. The XRD pattern of FS-L$_{1-x}$MO also matches well to the cubic spinel $LiMn_2O_4$ structure, but all peaks shifted to a higher 2 Theta value compared with those of $LiMn_2O_4$ due to the change of the lattice structure caused by the electrochemical removal of Li^+ ions. There is no significant change in the number and relative intensities of characteristic diffraction peaks, indicating that the FS-L$_{1-x}$MO retains the cubic spinel $LiMn_2O_4$.

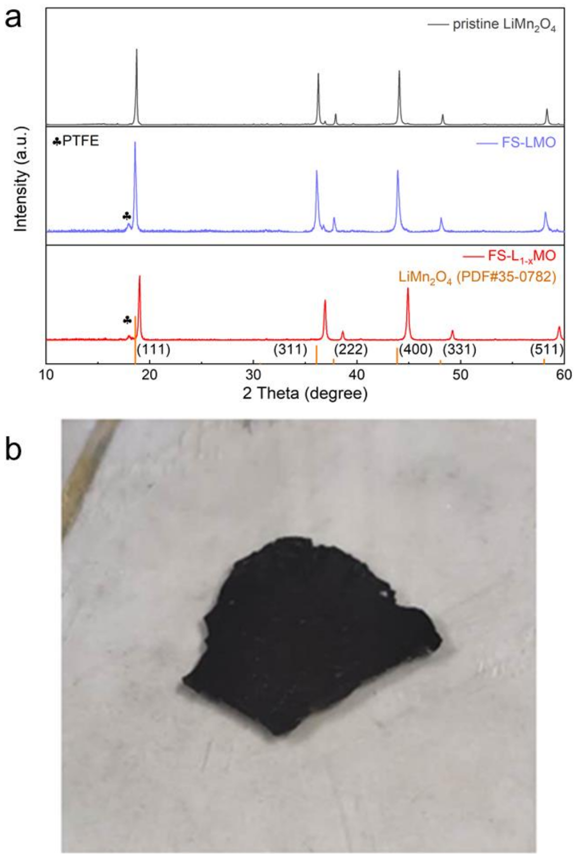

Figure 4.5 (a) XRD patterns of pristine $LiMn_2O_4$, the free-standing electrode (FS-LMO), and FS-L$_{1-x}$MO (b) A digital image of the free-standing FS-LMO electrode.

4.2.3.3 Electrochemical performance

To confirm whether the high-loading FS-LMO can be used to deliver a large and reversible capacity of Li^+, the constant cut-off voltage test is performed by charging/ discharging the Li metal half-cell, Li/FS-LMO in the range of 3-4.3V. If the cell can deliver a large charging/discharging capacity to the Li/LMO cell, as well as CE~1, then FS-LMO can serve as Li recovery electrode. As illustrated in Figure 4.6a, the charging/discharging curves for the 1st and 5th cycle were obtained in terms of voltage versus specific capacity. The cell delivered a charging and discharging capacity of 112.01 (0.757 Li^+) and 109.72 (0.741 Li^+) mAh g^{-1}, respectively, with initial CE=97.97%. After the initial 4 cycles of activation at 0.2C, in the 5th cycle at 0.5C, the cell exhibits deliver a charging and discharging capacity of 111.696 (0.754 Li^+) and 111.176 mAh g^{-1} (0.751 Li^+), respectively, with an initial CE=99.52%. The high-loading electrode shows a comparable Li^+ intercalation/de-intercalation capacity to the small loading electrode. And CE in the initial cycle is even larger than the that observed from Li/LMO cell (~94%), which means the Li^+ intercalation/de-intercalation is even more reversible in the FS-LMO electrode. Thus, the FS-LMO can be used for the Li recovery electrode.

The charging and discharging curves are now further analyzed to explore the Li^+ intercalation/de-intercalation behavior inside the FS-LMO. For the first cycle at 0.2C, the curve shows two distinct charging plateaus consistent with the two peaks in its dQ/dV curve (Figure 4.6). At a potential higher than 3.9 V, the FS-LMO shows the typical behavior of lithium de-intercalation from the $LiMn_2O_4$ cubic spinel phase to the same phase of $Li_xMn_2O_4$ (between 3.9 and 4.1 V, delithiation). Following that, the phase transition rapidly enters the second stage, and spinel $Li_xMn_2O_4$ begins to convert to cubic λ-MnO_2 at the plateau around 4.15 V. In the discharging curve, two typical plateaus are also detected during the reductive lithiation plateaus, indicating reversible Li^+ intercalation/de-intercalation of $LiMn_2O_4$ in FS-LMO electrode. For the fifth cycle at the higher rate of 0.5C, the FS-LMO also clearly exhibits two reversible plateaus in the charging/discharging curves. The potential drop between the charge and the discharge process is only changing from 21 mV at 0.2C to 57 mV at 0.5C, indicating the fast kinetics of the system.

To further confirm that the capacity is only sourced from the Li^+ intercalation/de-intercalation of $LiMn_2O_4$ in FS-LMO, a differential capacity plot (dQ/dV curve) can be obtained from the charging/discharging curve. In the dQ/dV curve, the peak will be produced where a large capacity is delivered in a small voltage range, corresponding to an electrochemical reaction. In the present case, if the dQ/dV curve can demonstrate reduction/ oxidation peaks in pairs and the peaks only match the reported $LiMn_2O_4$ electrode, then the FS-LMO can be proved to deliver a reversible capacity from $LiMn_2O_4$.

Herein, a dQ/dV curve of the first cycle is illustrated in Figure 4.6b. Two pairs of symmetrical redox peaks appear at 3.98 /4.01 V and 4.11 /4.15V, which are characteristic of reversible Li^+ intercalation/de-intercalation from the $LixMn_2O_4$ lattice.[82, 95] The oxidation peaks at 3.98 and 4.11 V (vs. Li^+/Li) are associated with the two-stage conversion of the $LiMn_2O_4$ phase to the λ-MnO_2 ($0 < x < 1$) phase, whereas the reduction peaks at 4.01 and 4.15 V (vs. Li^+/Li) are associated with the reversible insertion of Li ions into the λ-MnO_2 phase with the formation of $LiMn_2O_4$. All the peaks belong to the Li^+ intercalation/de-intercalation of $LiMn_2O_4$ in the FS-LMO electrode. Thus, during charging and discharging, only $LiMn_2O_4$ inside the FS-LMO electrode can deliver Li^+ capacity by Li^+ intercalation/de-intercalation from the $LiMn_2O_4$ lattice. Consequently, FS-LMO can be used to deliver a large and reversible capacity from $LiMn_2O_4$ in the present LMB-mimic system.

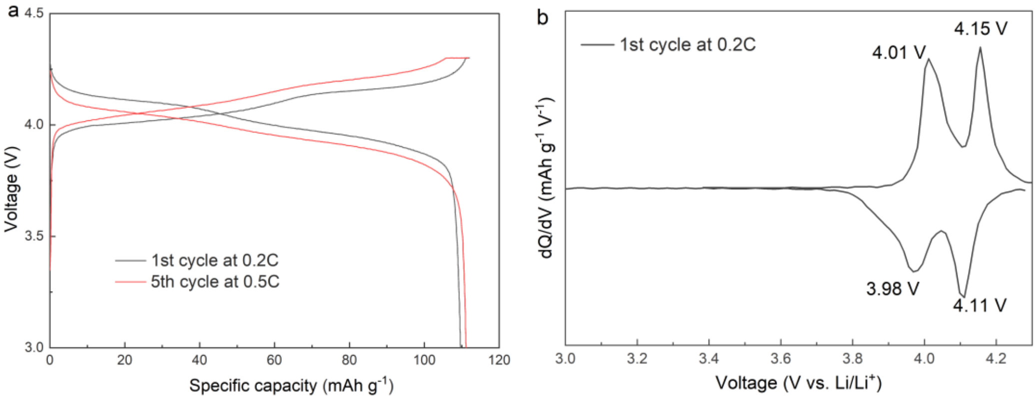

Figure 4.6 (a) Galvanostatic charge-discharge profiles of Li/FS-LMO cell cycling between 3V and 4.3V at 0.5C after the initial four cycles at 0.2 C for activation, and (b) the corresponding differential capacity (dQ/dV) plots. (The active mass of the FS-LMO electrode, $mLiMn_2O_4$=35.41 mg cm^{-2})

4.3 Li plating by LMB-mimic system

4.3.1 Spontaneous Li recovery FS-L_{1-x}MO from LiOH aqueous solution

In the LMB-mimic system, the FS-L_{1-x}MO will serve as the Li recovery electrode to extract Li^+ from the LiOH solution through the spontaneous reaction. Then the electrode will be used to plate Li in the LMB system. To investigate the Li recovery performance of FS-L_{1-x}MO, the electrode was immersed in 0.1M LiOH solution for several duration. The Li plating capacity directly shows the Li recovery performance after FS-L_{1-x}MO was immersed in 0.1M LiOH for a different time. In the Li recovery experiment, the FS-L_{1-x}MO electrodes with similar mass loading of 4-5 mg cm^{-2} were prepared by charging the Cu/FS-LMO cell at 0.2C until 4.3V, then keeping at the voltage until the current to 0.05C, making this FS-L_{1-x}MO reaching the delithiated state of 4.3V. And in the Li recovery process, these FS-L_{1-x}MO were immersed into 1L of 0.1M LiOH solution under stirring, providing constant concertation for Li recovery. After recovery and dried fully, the FS-L_{1-x}MO was assembled into Cu/ LMO battery and charged at 0.05C until the delithiated state of 4.3V. In theory, the Li plating capacity should be equal to the Li^+ recovered amount by FS-L_{1-x}MO.

4.3.1.1 Kinetic curve of spontaneous Li recovery

The Li recovery performance of FS-L_{1-x}MO is demonstrated in Figure 4.7 by the curve of Li plating capacity over immersing time. The FS-L_{1-x}MO exhibits two-stage Li^+ extraction behavior. In the first stage ranging from 0 to 2 min, the Li plating capacity increases quickly from 4 to 70 mAh g^{-1}. At 0 min, the electrode was not immersed in the LiOH aqueous solution, yet. It can also deliver a few capacities around 4 mAh g^{-1} because the FS-L_{1-x}MO was prepared by charging FS-LMO at 0.2C, and at such a large current, the Li^+ cannot be fully de-intercalated due to polarization inside the electrode. And under 0.05C, the polarization will decrease, and the electrode will release the remaining Li^+. Thus, it can be calculated theoretically that about 0.44 Li^+ were intercalated into FS-L_{1-x}MO in the first 2 min. After 2 min, the Li extraction of FS-L_{1-X}MO goes into the other stage, where the Li plating capacity increases more slowly. Until the immersing time reaches 18 min, the Li recovery electrode delivers the maximum Li plating capacity of ~120 mAh g^{-1}. Afterward, the Li plating capacity keeps almost constant with extending immersing time in LiOH. It can be calculated that the equilibrium Li plating capacity after Li recovery can reach ~0.78 Li^+, which is even a little larger than the charging capacity when fabricated FS-L_{1-X}MO. Considering the possible influence of mass loading, it is reasonable to believe that the FS-L_{1-X}MO can be fully converted into FS-LMO by the spontaneous Li recovery reaction. This result is also consistent with the thermodynamic result.

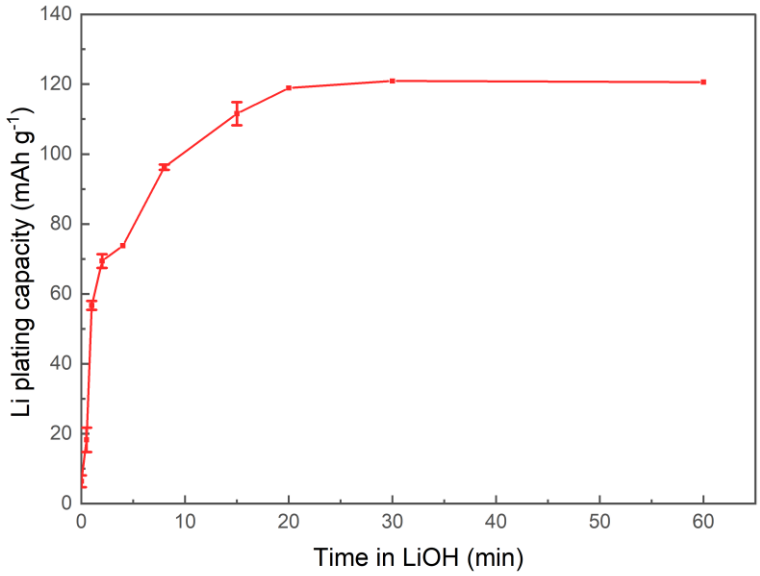

Figure 4.7 Effect of immersing time of FS-L_{1-x}MO in 0.1M LiOH solution on the theoretical Li-recovery amount. ($mLiMn_2O_4$=4~5 mg cm^{-2})

4.3.1.2 Li^+ intercalation into Li recovery electrode

To further elucidate the Li^+ extraction mechanism with FS-L_{1-x}MO, ex-situ XRD can be used to track its structure evolution during the spontaneous Li recovery. The spontaneous Li recovery was reported to be realized by the Li^+ intercalation into the tetrahedral sites in the lattice of cubic spinel $LiMn_2O_4$. With the intercalation of Li^+, the lattice parameter would change, and a possible phase transition would occur. Ex-situ XRD is a powerful tool to detect the phase transition and the lattice parameters changes inside the electrode by specifying the characteristic diffraction peaks and tracking their shifts. In this study, the ex-situ XRD was performed by collecting the XRD spectrum of FS-L_{1-X}MO electrode after every minute it was immersed in LiOH solution. And the setup for the ex-situ XRD is the same as the standard powder sample holder. To make these spectra comparable, the optical and sample alignment was performed only once at the beginning of the 1st spectrum measurement to keep the X-ray path unchanged.

The results of the ex-situ XRD spectra are presented as waterfall plots, as demonstrated in Figure 4.8. The invariant peaks at 29.5° belong to $LiOH·H_2O$, which was induced because the FS-L_{1-X}MO were directly measured without further washed after being immersed in LiOH solution, and possible solute residuals were left inside the electrode. It can be obviously seen that (111), (311), (222), (400), and (331) peaks shifted to the lower angles in the Li recovery reaction, which means that in the Li recovery process with FS-L_{1-X}MO, only the spinel manganese oxide was involved in the Li^+ extraction and Li accomplished the process intercalated into its lattice, thus causing an increase of lattice parameters. Interestingly, the peak position shift was separated into two linear regions by a clear phase transition turning point (dashed circle at t=5-6min). That means the Li^+ intercalation in Li recovery is accomplished by a phase transition from λ-MnO_2 to $LiMn_2O_4$ inside the electrode, the same as the reported in-situ XRD result of discharging process of the Li/ $LiMn_2O_4$ battery.[100, 101] Combining with the two-stage behavior in Li-recovery curves in Figure 4.7, it is reasonable to believe that, in the Li recovery process, the behaviors of Li^+ intercalated into FS-L_{1-X}MO are the same as in the discharging.

In the first stage (stage I), x Li^+ will be intercalated into the lattice with the two-phase transition process from the λ-MnO_2 phase to the $Li_xMn_2O_4$ phase. Because of the distinct differences in lattice parameters of these two phases, the phase transition turning point will usually be detected, as shown in the dashed circle in Figure 4.8.[101]. Upon further intercalation of lithium ions into the host $Li_xMn_2O_4$ structure (stage II), $Li_xMn_2O_4$ gradually accommodates extra (1-x) mole Li^+ per formula unit, and finally, $LiMn_2O_4$ will be regenerated. Nevertheless, the phase transition from $Li_xMn_2O_4$ to $LiMn_2O_4$ is challenging to be distinguished because of the similar lattice parameters.[101] That is why for this phase transition, the position of the peak shift slowly in a long and linear manner in the ex-situ XRD result. Thus, it can be concluded that in the Li recovery, Li^+ will be intercalated into the tetrahedral sites of spinel $LiMn_2O_4$ in FS-L_{1-X}MO in two stages, as shown in the following equations:

Stage I $$\lambda - \mathrm{MnO_2} + \mathrm{xLi^+} \rightarrow \mathrm{Li_xMn_2O_4}$$

Stage II $$\mathrm{Li_xMn_2O_4} + (1-\mathrm{x})\mathrm{Li^+} \rightarrow \mathrm{LiMn_2O_4}$$

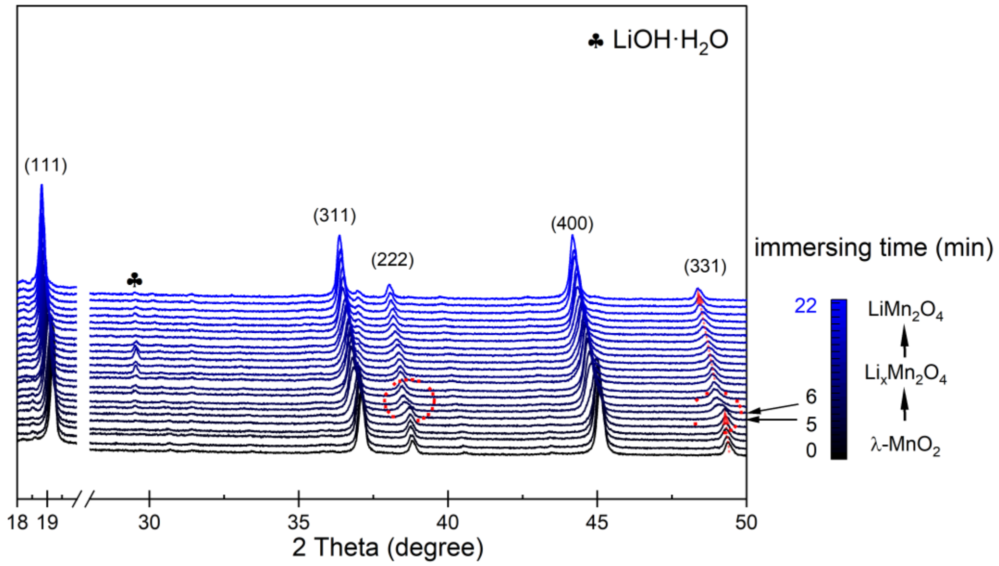

Figure 4.8 Ex-situ XRD patterns of the FS-L$_{1-x}$MO electrode for a different immersing time in 0.1M LiOH aqueous solution. Each curve was obtained every 1 min until the bubbles stopped on the electrode's surface. (mLiMn$_2$O$_4$=25.3 mg cm^{-2})

4.3.2 Li plating in the LMB system

4.3.2.1 Li$^+$ de-intercalation from Li recovery electrode

In the Li recovery process, ex-situ XRD was implemented on the Li recovery electrode to track its phase transition upon Li recovery. The Li recovery from LiOH by FS-L$_{1-x}$MO was found to be realized by a two-stage phase transition of the spinel manganese oxide. After the spontaneous Li recovery from LiOH aqueous solution by FS-L$_{1-x}$MO, the regenerated FS-LMO will be used to plate Li metal in the LMB system. To further explore the reversibility of the structure of the Li recovery electrode in the LMB-mimic system, the structural evolution of the regenerated FS-LMO upon Li plating was also investigated by the in-operando XRD. The in-operando XRD is usually used to characterize the phase transition inside the electrode during charging/discharging in the battery. The homemade setup for in-operando XRD measurement of FS-LMO during Li plating is illustrated in Figure 4.9a. The operando XRD spectra were obtained by continuously multiple XRD measurements while charging the Cu/FS-LMO cell at the current density of 0.75mA cm^{-2} until 4.3V.

During in-operando XRD measurement, the charging curve exhibits two typical plateaus of LiMn$_2$O$_4$ as shown in Li/ LiMn$_2$O$_4$ cells, as demonstrated in Figure 4.9b.

The in-operando XRD spectra of the regenerated FS-LMO are presented as Contour plots. In the operando XRD spectra of FS-LMO cathodes, all the characteristic peaks correspond to the cubic spinel $LiMn_2O_4$ structure. In the charging process, these peaks shifted to the higher 2 Theta value together, which means that in the Li plating process, only the spinel manganese oxide inside FS-LMO was involved in the Li^+ extraction, and the process was accomplished by Li de-intercalated from the lattice, thus causing a decrease of lattice parameters. To clearly analyze the phase transition in the process, herein, the position shift of (400) peaks in $LiMn_2O_4$ will be focused. It is obviously seen that there remain two-phase transition turning points. Li^+ de-intercalation is accomplished by phase transitions from $LiMn_2O_4$ to λ-MnO_2 inside the electrode, as indicated by the dashed circle and rectangle, the same as the reported in-situ XRD result of the charging process of Li/ $LiMn_2O_4$ battery.[95, 102]

From previous reports,[103, 104] in the charging process of Li/$LiMn_2O_4$ cell, three phases inside $LiMn_2O_4$ electrode are involved in the phase transition, including a single-phase $LiMn_2O_4$, the mixed phases of $LiMn_2O_4$/$Li_xMn_2O_4$ and the mixed phases of $Li_xMn_2O_4$/λ-MnO_2. Thus, in the Li plating process, for the 1st charging state, Li^+ will be firstly de-intercalated from the tetrahedral sites of $LiMn_2O_4$ to form a $Li_xMn_2O_4$ in the mixed phases of $LiMn_2O_4$/ $Li_xMn_2O_4$. And the phase transition turning point occurs where the dominant component in the mixed phase changes from $LiMn_2O_4$ to $LixMn_2O_4$, as shown in the dashed rectangle of (400) peak in Figure 4.9b. Upon further de-intercalation, Li^+ will be de-intercalated from $LixMn_2O_4$ to form λ-MnO_2. At a high state of charge, with more and more Li^+ removed from the lattice, λ-MnO_2 will start to dominate in the mixed phase of $Li_xMn_2O_4$/λ-MnO_2 where the dashed cycle reveals. The high diffraction intensity of λ-MnO_2 can also be noticed at the end of charge. Thus, it can be concluded that during the Li plating, Li^+ will be de-intercalated from the tetrahedral sites of spinel $LiMn_2O_4$ in FS-LMO in two stages (I and II), and the behavior of Li^+ of the Li recovery electrode in the plating is reversible as the one in Li recovery process.

Stage I $$\mathrm{LiMn_2O_4} - (1-\mathrm{x})\mathrm{Li^+} \rightarrow \mathrm{Li_xMn_2O_4}$$

Stage II $$\mathrm{Li_xMn_2O_4} - \mathrm{xLi^+} \rightarrow \lambda - \mathrm{MnO_2}$$

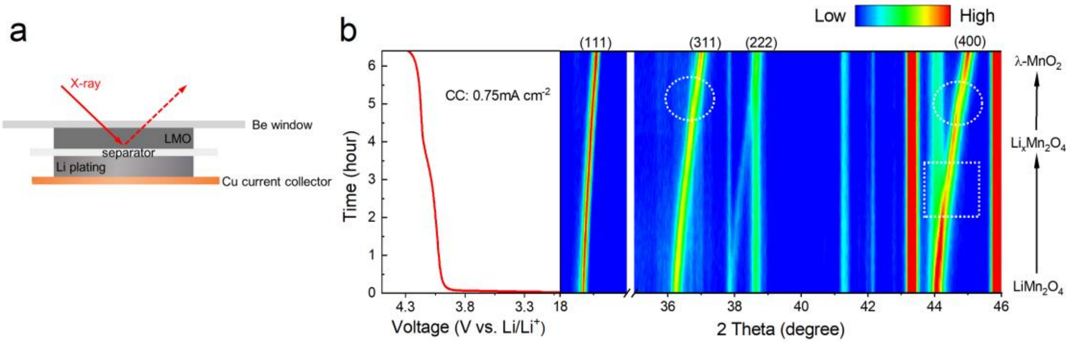

Figure 4.9 (a) Structure of cell for in-situ XRD measurement of Li-recovery electrode during Li plating (b) Contour plot of the in operando XRD patterns of the Li-recovery electrode in the Li plating process in the range of 3-4.3 V (vs. Li^+/Li) at 0.75mA cm^{-2}

4.3.2.2 Metallic Li deposition

To confirm that the Li^+ de-intercalated from the FS-LMO will be stably deposited into metallic lithium in the LMB system, in-operando XRD measurement was also implemented on the Li deposition side. The setup for this in-operando measurement is illustrated in Figure 4.10a. To accurately measure the XRD signal of Li, in this test, the Be window will serve as the anode for metallic Li plating. Because before Li plating, no Li metal remains in the LMB system. Thus, at the beginning of Li plating, there will be no XRD signal. And if in the Li plating process, Li^+ de-intercalated from FS-LMO will be continuously deposited into metallic Li. There will be some diffraction signal of accumulated Li metals in the in-operando XRD result. As demonstrated in Figure 4.10b, the in-operando XRD of Li during Li plating by FS-LMO and the corresponding charging curve were obtained. As shown in the charging curve, it delivered a typical two plateaus performance of Li de-intercalated from spinel $LiMn_2O_4$. And it can be observed that at the beginning of Li plating, no Li peaks are detected in the Contour plot. With the proceeding of Li plating, the characteristic peak of Li located at 36.2° corresponding to Li (110) (PDF#15-0401) exhibited measurable diffraction intensity. The Li peak intensity increases with the increase in Li plating time. Consequently, it can be confirmed that Li^+ de-intercalated from the Li recovery electrode will be plated into Li metal in the Li plating process. Furthermore, the LMB system can provide a stable environment for Li plating.

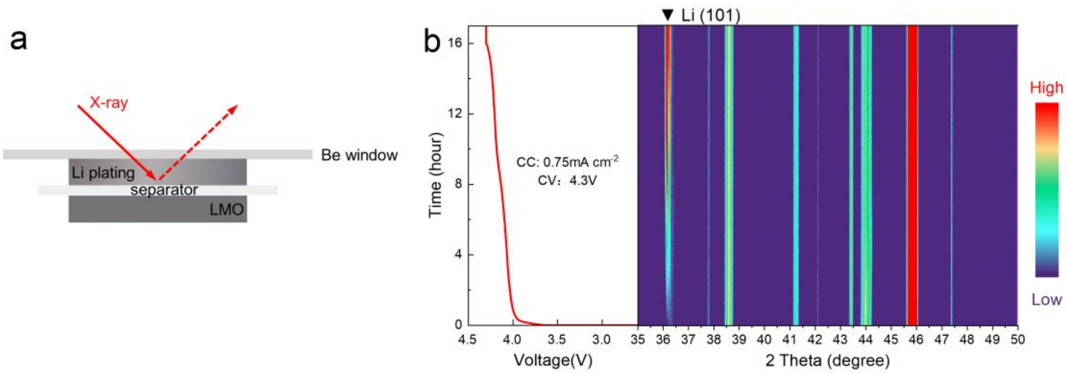

Figure 4.10 (a) Illustration of cell structure for in-situ XRD measurement of the plated Li during the Li plating process (b) Contour plot of the in-situ XRD patterns of the plated Li in the Li plating process in the range of 3-4.3 V (vs. Li^+/Li) at 0.75mA cm^{-2}.

4.3.3 Stability of LMB-mimic system for Li plating

In the previous section, it has been proved experimentally that the LMB-mimic system can be used for Li plating from LiOH aqueous solution. In the LMB-mimic system, Li^+ will be extracted from LiOH by Li recovery process with the recovery electrode, converting FS-L_{1-X}MO to FS-LMO, and then be plated into metallic Li by Li plating process, converting FS-LMO to FS-L_{1-X}MO. The Li recovery and plating cycles have been realized by the Li^+ intercalation/de-intercalation into/from the tetrahedral sites of $LiMn_2O_4$ inside the Li recovery electrode. It was found that totally reversible phase changes of $LiMn_2O_4$ accomplished the Li^+ intercalation/de-intercalation in the Li recovery electrode. Such reversible phase changes are the same as the ones in the charging/discharging process in Li/LMO cells. Considering the excellent charging and discharging cycling performance of $LiMn_2O_4$ in Li/LMO cells, it is reasonable to believe that the Li recovery electrode can be reused for multiple cycles of Li recovery and plating.

4.3.3.1 20-cycle performance of Li plating

Herein, to further confirm the stability of the Li recovery electrode in the system, the electrode is tested in the Li recovery-plating cycles. For the test, the Li recovery electrode was used to extract Li^+ from the LiOH solution and then served as the cathode to plate Li on the Cu anode by charging the Cu/LMO battery. After Li plating, the battery was disassembled, and the Li recovery electrode was reused in repeated Li recovery-plating cycles. If the electrode can deliver a stable Li plating capacity over cycles, it could be stably used for Li plating in the LMB-mimic system. In this study, the Li recovery and plating cycle have been repeated for 20 times with the same Li recovery electrode. And the results of Li plating capacity over cycles are shown in Figure 4.11. As shown in Figure 4.11, over the 20 cycles of Li recovery and plating, the Li recovery electrode delivered a stable Li plating capacity of around 112 mAh g^{-1}, corresponding to 0.756 Li^+. The retention rate of the Li plating capacity in 20 cycles is 99.73 %, which means the Li recovery electrode can extract Li^+ from LiOH and plate Li stably for at least 20 cycles. The process is therefore can be taken as stable at least as a proof of concept for the initial evaluation. Of course, if there is sufficient time, data with more cycles would be preferred. However, if the LiOH solution and the status of the FS-LMO are similar, one would expect similar results for prolonged cycling.

For a closer look at the stability of the Li electrode recovery over cycles, the selected charging curves for 1st, 5th, 10th, 20th cycle were obtained, as illustrated in Figure 4.12a. And their corresponding dQ/dV data are presented in Figure 4.12b. As shown in Figure 4.12, during these cycles, the charging curves exhibit typical two-stage behavior of Li^+ de-intercalation from the tetrahedral sites of $LiMn_2O_4$, which is consistent with the result of dQ/dV in Figure 4.12b, the two characteristic peaks of Li^+ de-intercalation from $LiMn_2O_4$ are distributed in almost the same position in different cycles. That means that the Li plating capacity of various cycles was delivered from the tetrahedral sites of $LiMn_2O_4$ with the same phase transitions. Furthermore, the charging curves from different cycles almost completely overlapped. It means both phase transitions of $LiMn_2O_4$ and their corresponding Li capacity after Li plating can be totally recovered by the Li recovery process. Thus, the phase transitions for Li^+ intercalation/de-intercalation in the Li plating-recovery cycles are entirely reversible. That is why the Li recovery electrode can deliver a stable Li plating performance in the 20 cycles of Li recovery and plating.

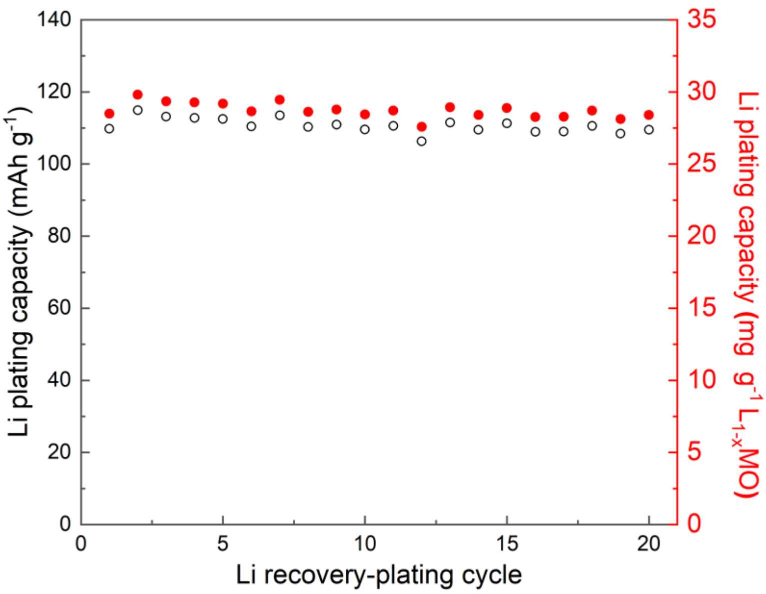

Figure 4.11 Li recovery-plating cycling performance of Li-recovery electrode for 20 cycles. (m$LiMn_2O_4$=20 mg cm^{-2})

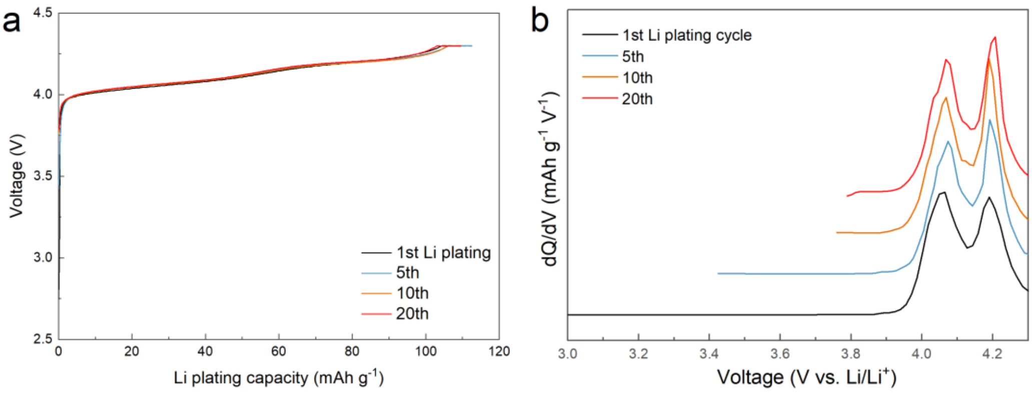

Figure 4.12 (a) 1st, 5th, 10th, and 20th Li plating by the galvanostatic charge of Cu/LMO cell till the upper cut-off voltage of 4.3V at 0.5C, and (b) the corresponding differential capacity (dQ/dV) plots. (m$LiMn_2O_4$=20 mg cm^{-2})

4.3.3.2 Structural reversibility of Li recovery electrode

To characterize the structural reversibility of the Li recovery electrode in the 20 cycles, the XRD patterns of the electrode before and after Li recovery in the 1st and 20th cycles were obtained, Figure 4.13. It can be seen from the graph that the crystalline structure of the Li recovery electrode before the 1st and 20th cycles, and after the 1st and 20th cycles looks similar, consistent with that of $LiMn_2O_4$. The Li recovery electrode is fabricated by electrochemical removal of Li^+ from $LiMn_2O_4$. The shift of the peaks to a higher 2 Theta value in the first cycle (also in the 20th cycle) is resulted from the change of the lattice structure because of delithiation, which is consistent with the in-operando XRD result in Figure 4.9b. After Li recovery, these peaks of the electrode in the first cycle shifted back to a lower 2 Theta and matched well to the cubic spinel $LiMn_2O_4$ structure. Thus, in the first cycle, the shift of characteristic peaks of $LiMn_2O_4$ is reversible. Combining the result of the in-operando XRD for Li plating and ex-situ XRD in Figure 4.8 for Li recovery, it can be concluded that the reversible shift of these peaks before and after Li recovery is accompanied by reversible phase transitions. The data for the 20th cycle are similar to those observed for the 1st cycle, which show that the Li recovery electrode has an excellent structural reversibility, at least for 20 cycles of Li plating and recovery.

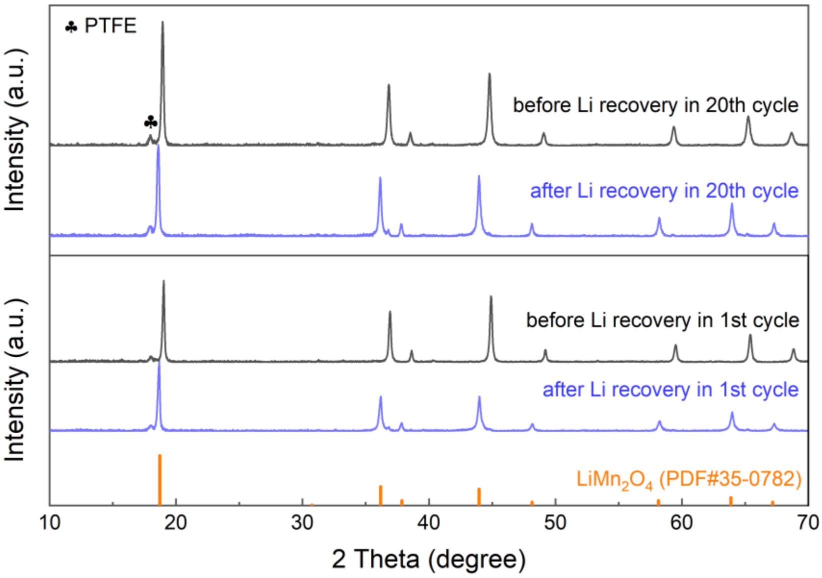

Figure 4.13 The X-ray diffraction pattern of the Li-recovery electrode before and after 1st, 20th Li plating.

4.4 Li plating efficiency of LMB-mimic system

4.4.1 Li plating efficiencies at various plating capacities

In the previous section, the LMB-mimic system has been theoretically and experimentally proved to convert the Li^+ in LiOH aqueous solution into Li metal. Through the reversible Li^+ intercalation/de-intercalation in the Li recovery electrode, the system can deliver a large Li metal plating capacity of ~0.75 Li per $LiMn_2O_4$ in the LMB system. Ideally, all the plated Li metal is “live” and can be used to provide the reactive surface for Li-mediated ammonia synthesis. However, because of the extremely low standard redox potential of Li (-3.04 V versus the standard hydrogen electrode),[105] even in the Li-friendly LMB system, the plated Li would inevitably react with the organic electrolyte upon contact and be partially consumed, forming a solid-electrolyte interface (SEI). The SEI formed during the Li plating was usually a passivating layer and cannot serve as the reactive surface for Li-mediated ammonia synthesis. Thus, to produce ammonia efficiently, increasing the ratio of "live" Li inside the Li deposits is required.

To evaluate the ratio of “live” Li inside the Li deposits, the concept of Li plating efficiency is examined in this part of study, as in previous reports.[19, 21, 66] First, the Li plating efficiency of the LMB-mimic system was calculated by dividing the Li stripping capacity over the previous Li plating capacity in the Cu/$LiMn_2O_4$ cell. The Li plating efficiency can then be used to evaluate the "live" Li ratio in the deposits because after Li is plated on the Cu in the system, by discharging the cell, only "live" Li inside the Li products can be stripped from the Li deposits and then re-intercalated into $LiMn_2O_4$. Consequently, a large value of Li plating efficiency is essential for Li plating by the LMB-mimic system to produce ammonia efficiently by the Li-mediated ammonia synthesis.

$$\begin{aligned}\text{Li plating efficiency } &= \frac{\text{Li stripping capacity}}{\text{Li plating capacity}}\\ &= \frac{\text{amount of Li}^{+}\text{can be stripped reversibly from Li deposits a}}{\text{theoretical amount of Li in the deposits}}\\ &\approx \frac{\text{amount of "live" Li in the deposits}}{\text{theoretical amount of Li in the deposits}}\end{aligned}$$

Even though the formation of SEI will consume a certain amount of “live” Li, another fact about SEI should also not be neglected. The built-up SEI will form a dense and passivating layer on the surface of Li metal. Such a layer can effectively prevent further physical contact between Li and the solvent, making Li dynamically stable in the organic solvents.[106] Consequently, only a limited thickness of SEI will be formed on the surface of Li metal, which is also why Li metal can continuously serve as the anode in the LMB system for long-term cycling.[106] Based on the protective function of the SEI, if we continuously plate more Li metal in the LMB system, the ratio of Li consumption will theoretically further decrease, and the ratio of "live" Li undoubtedly increases. Thus, a large Li plating efficiency could be obtained without further treatment or operation.

To test the above-mentioned hypothesis, the influence of Li plating capacity on the plating efficiency will be explored in the LMB-mimic system. To obtain different Li plating capacities, FS-L_{1-x}MO with different active mass loading of $LiMn_2O_4$ would be utilized as the Li recovery electrode to recover Li^+ and then plate Li metal in the LMB system. After charging the Cu/$LiMn_2O_4$ battery at 0.75mA cm^{-2} to 4.3 V for different Li plating capacities, the discharging operation will be implemented on the battery at the same current density to 2.8V for the Li stripping capacities. The Li plating efficiency was calculated by dividing the Li striping capacity over the Li plating capacity.

The Li plating/stripping curve in the LMB system is presented in Figure 4.14a. It can be observed from the charging curves these Cu/$LiMn_2O_4$ batteries exhibit various Li plating capacities ranging from 2.90 to 12.65 mAh cm^{-2}. All the charging curves showed two typical plateaus of Li de-intercalation from the tetrahedral sites of $LiMn_2O_4$, which means the $LiMn_2O_4$ accomplished the Li plating. The discharging curves also exhibit two stages, and the capacities from the first discharging stage are almost equal to the one in the second charging stage, which indicates the order of Li^+ intercalated back into the lattice of $LiMn_2O_4$ in the Li stripping process. With the increased Li plating capacities, the second discharging plateaus would become longer and deliver more capacities. Thus, in the discharging process, it can be concluded that Li^+ will be stripped from the plated Li and intercalated into $LiMn_2O_4$. To clearly present the relationship between Li plating capacity and plating efficiency, the Li plating efficiencies were calculated and plotted over the Li plating capacities, as shown in

Figure 4.14b. As observed from the curve, when the Li plating capacity is located below 6 mAh cm^{-2}, it only delivers a small plating efficiency of ~50%, which means that at such a small plating capacity, in the Li plating products, only about half of it was composed of "live" Li. This result at low plating capacities is similar to the previous reports.[21] Such low value is believed to be caused by the Li consumption by forming SEI during Li plating. With the increasing Li plating capacities, the plating efficiencies will increase dramatically. When the capacity reaches over 12.65 mAh cm^{-2}, the efficiency can reach a value of over 95%. After 12.65 mAh cm^{-2}, the Li plating efficiency begins to increase more slowly. It could be predicted that, with further increase in capacity, this value of Li plating efficiency could approach its theoretical limits of 100%. This experimental result indirectly proves the hypothesis. Consequently, to efficiently plate Li for the Li-mediated ammonia synthesis, it is better to control the areal plating capacity over 12.65 mAh cm^{-2}.

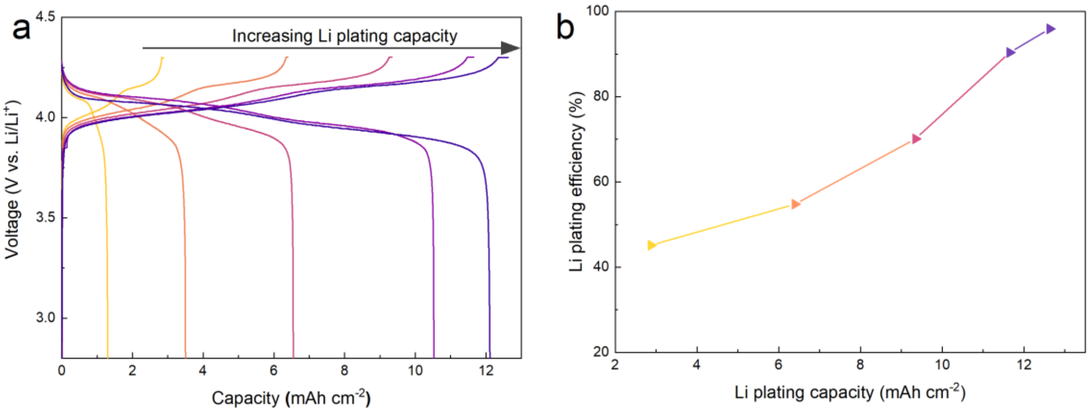

Figure 4.14 (a) Voltage profiles during Li plating and Li stripping for various Li plating capacities of 2.90, 6.40, 9.35, 11.60, and 12.60 mAh cm^{-2} and (b) the effect of Li plating capacity on the Li plating efficiency. The Li plating efficiency was calculated by dividing the total charges passed during stripping by the total charges passed during the previous plating. The current density during plating/stripping was 0.75 mA cm^{-2}.

4.4.2 Effects of Li plating capacity on plating efficiency

4.4.2.1 Morphology evolution

From the experimental results, it has been confirmed that as the Li plating capacity increased, the plating efficiency approaching unity would be obtained. Specifically, when the plating capacity reaches the value of 12.65 mAh cm^{-2}, the value reaches 95.79%. According to the definition of Li plating efficiency, it was reasonable to believe that the increase of this value should be directly related to the decreasing ratio of the consumed Li in the Li deposits. In the LMB system, the parasite Li-consuming reaction would happen when the new surface of Li deposits is exposed to the electrolyte, and the surface exposure directly depends on the morphology evolution of the Li deposits. Therefore, to gain insight into how the Li plating capacity influences Li plating efficiency in the LMB system, it is required first to figure out how the morphology evolved with the increase of Li plating capacity. In this regard, morphologies of Li deposits with different plating capacities were visualized and scrutinized through SEM analysis. Four representative Li plating capacities, 0.75, 3.75, 7.50, and 15.00 mAh cm^{-2}, were obtained by Li plating in the LMB-mimic system at a constant charging current density of 0.75mA cm^{-2}.

As demonstrated in Figure 4.15a, at 0.75 mAh cm^{-2}, Li plated on the Cu foil surface in the form of thin film dotted with obviously uncovered Cu domains. When it increased to 3.75 mAh cm^{-2} (Figure 4.15b), these uncovered domains would be filled by the newly plated Li, only leaving small voids on the surface. As the Li plating capacities increased from 3.75 to 15.00 mAh cm^{-2} (Figure 4.15b-d), these voids would gradually shrink and finally disappear. Furthermore, the surface of Li deposits would become more closely packed and smoother. For a more apparent observation, it can be seen from Figure 4.15e that at a low Li plating capacity of 0.75 mAh cm^{-2}, the thin Li film was composed of both individual whisker-like Li particles and nodule-like particles. And the Li particles were distributed in the folded and crawling state inside the plated Li film. When the plating capacities further increased to 3.75 mAh cm^{-2} (Figure 4.15 f), the bare domains of Cu foil would also be filled by the newly plated Li, with the Li deposits being nodule-like and porous. With the growth of the newly plated Li (at 3.75 mAh cm^{-2} in Figure 4.15g), the surface 5 of the plated Li becomes more densified, with only a few tiny pores distributed. At 1.00 mAh cm^{-2} (Figure 4.15 h, m), the Li deposits become notably closely-packed on the surface, with the deposits forming nearly perfect columnar structures, similar to the reported low-porosity Li deposits.[107] Thus, with the further increase in plating capacity, the Li deposits become denser. The cross-section evolution was even more noticeable (Figure 4.15i-m). When the Li plating capacity was doubled from 7.5 to 15 mAh cm^{-2}, the thickness of Li deposits just increased from ~52 mm to ~60 mm, which means a significant improvement in densifying the Li deposits.

Eliminating the porosity of Li is crucial for minimizing surface exposure to liquid electrolytes, preventing extra parasitic reactions that would consume "live" Li. Consequently, with the increasing Li plating capacity, the porosity of the Li deposits will decrease. Thus, it was believed that with the increasing Li plating capacity, the elimination of porosity inside the Li deposits improved the plating efficiency.

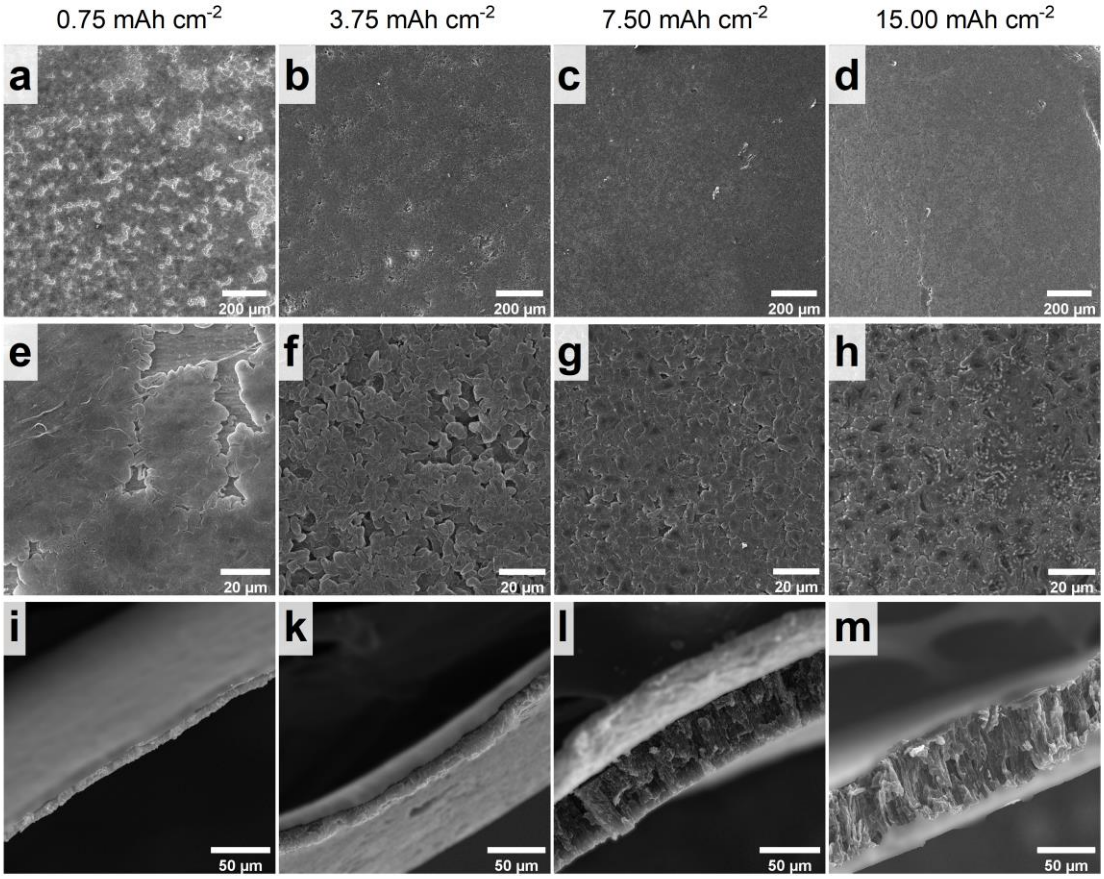

Figure 4.15 Microstructures of Li plated by the LMB-mimic system imaged by SEM. The SEM top-view (a-h) and cross-sectional view (i-m) images of deposited Li films on Cu foil. Each column represents a different Li plating capacity: 0.75 mAh cm^{-2} (a, e, i); 3.75 mAh cm^{-2} (b, f, k); 7.50 mAh cm^{-2} (c, g, i); or 15.00 mAh cm^{-2} (d, h, m).

4.4.2.2 Protective SEI layer on the surface of Li deposits

From the SEM results, it is found that eliminating porosity inside Li deposits would decrease the consumption of Li, thus improving Li plating efficiency. Such a conclusion was built on an essential prerequisite assumption: upon Li deposits contacting with electrolyte, only a limited amount of Li on the surface would be consumed to form an SEI layer, and the formed SEI would protect the inner Li deposits from further consumption. It was reported that SEI was the insoluble product of the parasitic reactions between Li and electrolyte and covered the surface of metallic Li. Since the reduction potential of organic solvent is less than 1.0 V (vs. Li^+ /Li), whenever bare Li contacts the electrolyte, rapid reactions between Li and electrolyte species occur in milliseconds or less, creating further SEI.[108] Thus, to double confirm the assumption above, a direct quantitative prove is required to show that only negligible-thickness SEI will cover the surface of Li deposits after Li plating. In this case, as demonstrated in Figure 4.15 e-h, the Li deposits are comprised of individual Li particles, and during Li plating, the growing Li particles are directly exposed to the electrolyte. Thus, the SEI would cover the surface of each Li particle. In this regard, in-depth X-ray photoelectron spectroscopy (XPS) profiling is frequently implemented in LMBs or LIBs study to characterize the thickness of the SEI.[106]

The in-depth XPS profiling is often composed of XPS measurement and surface sputter etching technique. In battery research, XPS is commonly used for SEI analysis by detecting the characteristic binding energy of elements (C, Li, F, O, P, etc.) at different compositions and chemical states.[109] It is a highly sensitive surface analysis method that probes the top ~10 nm of a film with a large area (e.g., 200×200 μm^2). Thus, only the chemical information of a thin surface layer can be obtained from XPS measurement.[109] By etching the surface with the sputtering technique for controllable durations, different-thickness into the surface layer will be removed from the deposits. And the chemical information of SEI from different depths could be revealed by XPS, forming the in-depth XPS profiles. Although the SEI layer in the thickness direction is not homogeneous, it is generally comprised of inorganic components, such as Li_2O, LiF, Li_2CO_3, and organic components, which are partial or complete reduction products of the solvent of the electrolyte, such as C-C/C-H, PEO and $(CH_2OCO_2Li)_2$.[106] The chemical information of SEI layer is distinct from that of Li metal (Li^0) beneath, which makes it possible to distinguish the SEI layer from the Li metal by the in-depth XPS profiles. Thus, by comparing the chemical information of different depths beneath the Li particle surfaces, the approximate thickness of SEI can be estimated from the in-depth XPS profile. In this study, the Li deposits of 15 mAh cm^{-2} were used for the in-depth XPS profile measurement due to its long plating duration of 20 hour. If after long-duration Li plating in the electrolyte, Li particles in the deposits could be only covered with a limited-thickness of SEI layer, it can confirm that this layer has limited consumption of Li.

The in-depth XPS profiles of Li1s, F1s, O1s, and C1s spectra are shown in Figure 4.17, and the characteristic binding energy utilized for peak fitting is listed in Table 4-1. The Li deposits are plated in the LMB system full of $LiPF_6$ and EC-based electrolytes. The C 1s spectra show that the SEI is comprised of four carbon-containing components: C-C/ C-H, poly (ethylene oxide) (PEO), Li_2CO_3, and $(CH_2OCO_2Li)_2$, which are the typical reduction products of EC.[110] The F 1s spectra show that the SEI contains two $LiPF_6$-derived reduction products: LiF and $Li_xPO_yF_z$.[111] For the Li1s spectrum, the peak in the range of ~53-56 eV can be deconvoluted into three components centered at ~55.7 eV, ~54.6 eV, and ~53.7 eV, which can be assigned to LiF, Li^0, and Li_2O, respectively.[112-115] The Li_2O may be a degradation product of Li_2CO_3 during Ar+ sputtering in the XPS experiment.[116] The O1s spectra are consistently comprised of several oxygen-containing species: PEO, Li_2O, poly (ethylene oxide) (PEO), and Li_2CO_3. The chemical species used for peak fitting have been reported to be the typical SEI components on Li metal in the $LiPF_6$ and EC-based electrolyte. And the distribution and evolution of chemical species have changed consistently in their elemental spectra, for example, with the increasing depth, the peak area of Li_2O increased in the Li1s spectrum together with the one in the O1s spectrum, which means the content of Li_2O increased with the depth in both spectra. All the evidence confirmed that the peak-fitting results from each spectrum are reasonable. Hence, the fitting results could be used to analyze the in-depth distributions of chemical species of SEI.

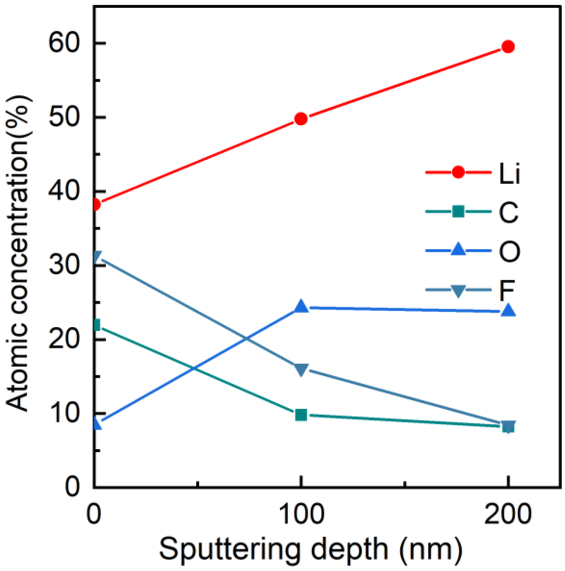

Figure 4.16 The relative composition of the atomic concentration of Li, F, O, C, and Li elements of the plating on Cu foil at 0.75 mA cm^{-2} for 15 mAh cm^{-2}.

The distribution of the chemical species is further confirmed by the atomic composition ratios in the SEI at different etching depths, as illustrated in Figure 4.16. The atomic ratio curve is also sourced from the in-depth XPS profiling and can quantify elemental information within the detection limit of about 1 atom%.[117] As shown in the plot, the C atomic signature at the surface (depth=0nm), as an indicator for organic components, is the highest among all the depths and decreases with the depth. Therefore, more organic species are observed in the outer layer of the SEI and decreased with the depth, which is consistent with the evolution of organic species in the peak-fitting results seen in Figure 4.17. With the increasing etching depth, the atomic ratio of F decreases quickly from 32% to 10%, caused by the disappearance of LiF. And the Li atomic ratio continuously increases with the depth, which is caused by the increase of Li_2O and the presence of Li metal in the deposits. Thus, the chemical information in various depths can be reliably used for estimating the thickness of SEI on the surface of Li particles.

As demonstrated in Figure 4.17, at the surface of Li deposits, both typical organic components (C-C/C-H, PEO, and $(CH_2OCO_2Li)_2$) and inorganic components (LiF, and $Li_xPO_yF_z$ and Li_2CO_3) can be distinguished from the elemental spectra. It can be observed that neither Li^0 nor Li_2O could be detected on the surface of Li deposits. When the etching depth increased to 100nm, the first occurrence of a significant Li^0 signal can be seen in the Li1s spectrum which indicates the gradual completion of the SEI layer. With further etching to 200nm, the Li^0 peaks become more evident. Thus, it can be evaluated that the thickness of the SEI layer should be in the range of 0-100nm. Comparing this value to the size of individual columnar Li particles (diameter: 5-10mm, length: ~ 50-60mm, evaluated from Figure 4.15h, m), it can be concluded that only a limited thickness of the SEI layer will cover the outer surface of Li particles. Thus, it can be confirmed that only a limited amount of Li will be consumed to form the protective SEI layer on the surface of Li particles.

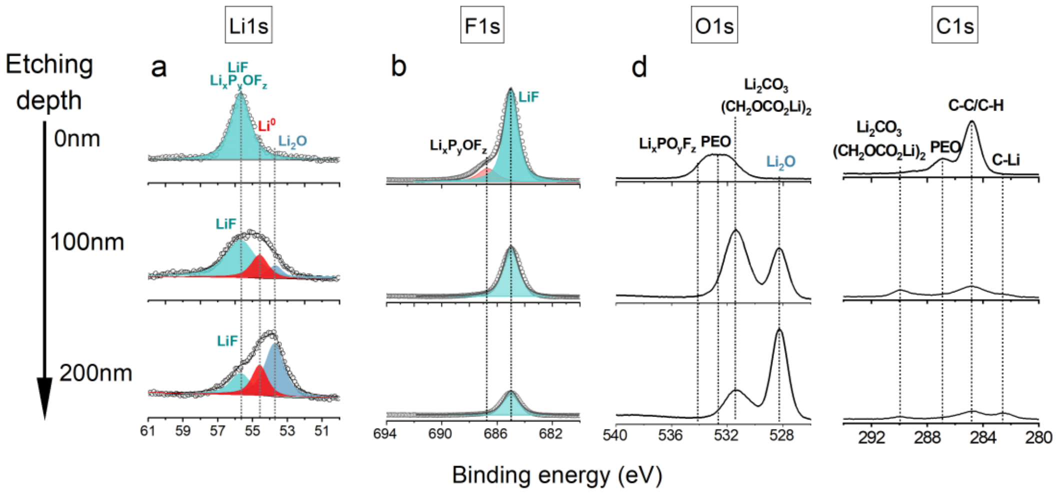

Figure 4.17 X-ray photoelectron spectroscopy (XPS) depth profiles of Li 1s, F 1s Li, O1s, and C1s spectra of Li plating on Cu foil at 0.75 mA cm^{-2} for 15 mAh cm^{-2}.

Table 4-1 XPS peak assignments and references for peak fitting in the XPS spectra.

	Binding energy (eV)			
SEI component	Li1s	F1s	O1s	C1s
Li^0	54.6[113]			
LiF	55.7[114, 118]	684.2[115]		
Li_2O	53.7[119, 120]		528.32[114, 121]	
Li_2CO_3			531.1	289.0[115]
$Li_xPO_yF_z$	55.7[115]	686.4[115]	534.0[115]	
$(CH_2OCO_2Li)_2$			531.1[115]	289.0[115]
C-C/ C-H				284.8[115]
PEO			532.5[115]	287.0[115]
C-Li				282.5[114]

4.5 Lithium nitridation and ammonia production

The motivation of this thesis is to continuously plate Li metal from LiOH to sustain the Li-mediated ammonia synthesis. In the Li-mediated ammonia synthesis, Li metal will be used to provide the reactive surface for breaking the stubborn N_2 molecules, forming Li_3N. Ammonia would be produced from Li_3N hydrolysis with the formation of LiOH. Since nitridation of metallic Li and the hydrolysis of Li_3N are spontaneous reactions under ambient condition, thus, to continuously produce ammonia under ambient condition, the continuous supply of Li from LiOH is the essential step. In this regard, the LMB-mimic system has been confirmed to be able to plate high-quality metallic Li from LiOH solution. The Li-mediated ammonia synthesis based on the LMB-mimic system can continuously produce ammonia under ambient condition. In this section, the ammonia production will be investigated experimentally with the Li deposits produced by the LMB-mimic system.

4.5.1 Effects of nitridation temperature

In the Li-mediated ammonia synthesis by the LMB-mimic system, both the Li plating and the hydrolysis of Li_3N can be operated quickly under the ambient condition. Thus, to efficiently produce the ammonia, it is required to explore the influence of the environmental factors (especially the temperature) on the nitridation of Lithium. In previous section, limited-thickness SEI layer was confirmed to cover Li deposits surface, and the SEI has been reported to interfere the diffusion of nitrogen gas to the Li surface.[19] To explore the intrinsic influence of temperature on nitridation, the commercial Li metal foil will be utilized for nitridation.

The Li foils (diameter:10mm, mass: ~30 mg) were exposed to the flowing of N_2 gas and held at temperatures between 25 and 100°C. The influence of temperature on the nitridation rate was reflected by the 1-hour conversion efficiency of Li to Li_3N. The conversion from Li to Li_3N was achieved by adding Li_3N to H_2O. The conversion efficiency is calculated according to Eq.4-22, by dividing the amount of ammonia detected over the theoretical amount of produced ammonia assuming the 100% Li metal utilization in the NH_3 synthesis. As demonstrated in Figure 4.18a, it can be observed that at 25°C, only negligible conversion efficiency was shown. When the temperature increased from 25 to 100°C, the value continuously increased, and at 100 °C, it reached the largest 1-hour conversion efficiency of 68.4%. That means the nitridation reaction rate increased with the temperature in the range of 25 to 100°C, which is consistent with the Arrhenius equation. At 100°C, it presented the largest nitridation rate among all temperatures. In present study, a reasonably higher temperature, 100°C, instead of room temperature, is set to accelerate the nitridation step.

$$\text{Conversion efficiency} = \frac{\text{amount of ammonia detected}}{\text{theoretical amount of } \mathrm{NH_3} \text{ produced from Li}} \qquad 4\text{-}12$$

To study the kinetic process of the nitridation of commercial Li foil at the optimal temperature, the Li foil (diameter:10mm, mass: ~30mg) was exposed to the flowing N_2 gas, with the temperature held at 100°C, and the curve of conversion efficiency over nitriding time was illustrated in Figure 4.18b. It could be observed that in the first 30 min of nitridation, almost no Li was converted to produce ammonia. After 30 min, the conversion efficiency reached an increasing zone over time. And at about 85 min after the Li foil exposed to nitrogen, the curve exhibited a turning point, and the conversion efficiency equals to ~100%. After that, the value would keep unchanged even with the increasing nitridation time. It can be concluded that the 30-mg Li foil was fully converted into Li_3N after ~85min. At 100°C, the nitridation rate of Li foil could be calculated to be 0.3529 mg Li min^{-1}.

Through nitridation and hydrolysis, the Li foil was confirmed to be fully utilized to produce NH_3. To further confirm that the ammonia was produced from the Li-mediated pathway of Li-Li_3N-NH_3, it is still required to confirm that Li_3N was the intermediated products in the Li-mediated ammonia synthesis. In this vein, XPS analysis was implemented on the surface of bared Li before and after nitridation. To make the Li foil fully nitrided, the Li foil was kept in the flowing N_2 gas at 100 °C for 2 hours. The N1s elemental spectrum from XPS characterization is demonstrated in Figure 4.19. Before nitridation, only messy background signal can be observed from the elemental spectrum. By contrast, the N1s spectrum from the Li after nitridation displayed an obvious Li_3N signal located at ~398.5 eV.[74] Thus, it can be concluded that by nitridation, the metallic lithium will be converted to Li_3N. Consequently, Li_3N is the intermediated product in the Li-mediated ammonia synthesis, and NH_3 is produced by the pathway of Li-Li_3N-NH_3.

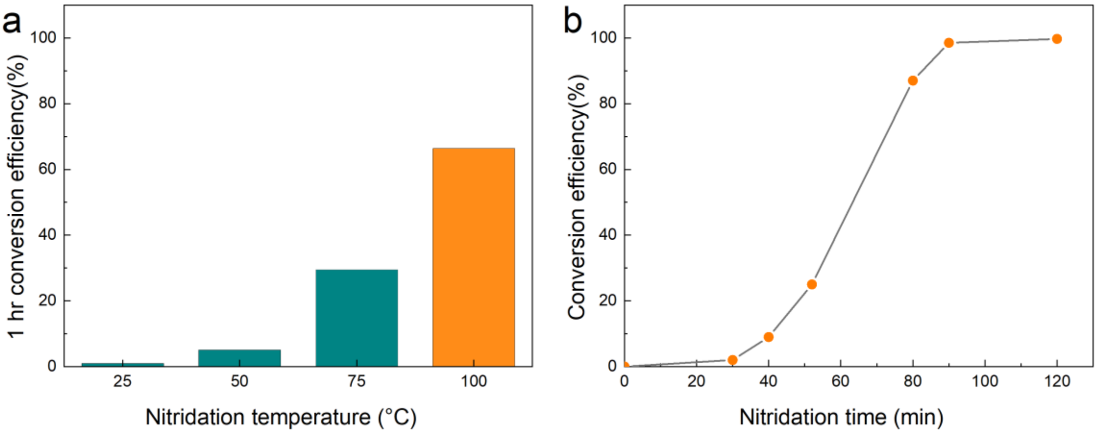

Figure 4.18 (a) The effects of temperature on the nitridation of commercial Li foils (b) conversion efficiency using commercial Li foil nitride at 100 °C over time. In the nitridation of Li, the commercial Li foils with a diameter of 10 mm and mass about 30 mg were used.

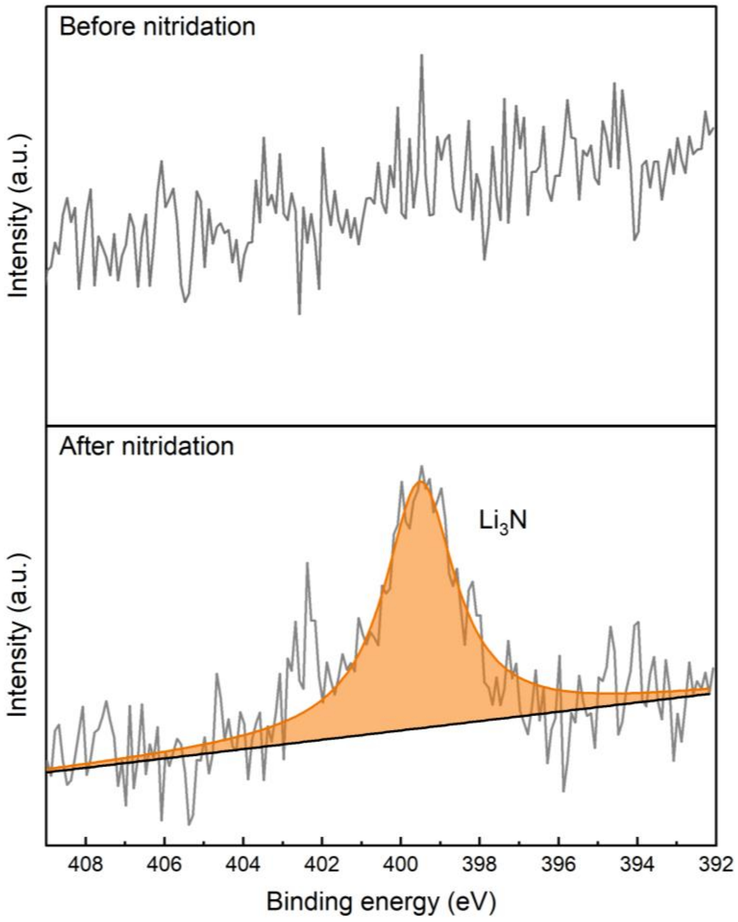

Figure 4.19 N1s XPS spectra of the commercial Li foil before and after nitridation.

4.5.2 Nitridation of Li deposits

After determining the optimal nitridation temperature, the Li deposits also were exposed to the N_2 atmosphere, to confirm the Li deposits from the LMB-mimic system could also be utilized for ammonia production. In previous section, the Li deposits have been confirmed to be mainly comprised of metallic Li. Considering the fact that commercial Li would be converted to NH_3 by the Li-Li_3N-NH_3 pathway, it can be assumed theoretically that the Li deposits could also be used for ammonia synthesis by the Li mediated pathway. Herein, to experimentally confirm this, the Li deposit will be utilized for nitridation to produce Li_3N. The XRD spectra will be obtained on the Li deposits before and after the nitridation, to characterize its crystal structure change by nitridation.

A Li deposit, with plating capacity of 20 mAh cm^{-2}, was first obtained by Li plating on the Cu foil in the LMB system. The Li was then exposed to the N_2 atmosphere for nitridation at 100 °C. In order to have a complete nitridation, the Li deposit was allowed to nitride for 4 hours based on the previous result of nitridation. Since both the Li deposit and its nitride were sensitive to the atmosphere components (H_2O, O_2, etc.), the XRD measurements were conducted by keeping the sample sealed in the in-situ XRD setup. The XRD spectra before and after complete nitridation are shown in Figure 4.20. Several strong interference peaks, ranging from 37° to 55°, are mainly derived from the comparts of the in-situ XRD setup (Be and BeO), as well as the Cu foil. From the XRD spectra before nitridation, it can be still observed that there are two obvious peaks located at the 2-theta value of ~36.21° and ~65.04°, corresponding well to the crystalline face of (110) and (211), respectively, of Li (PDF#15-0401-Li). The result is consistent with the in-operando XRD in the Li plating, which indicates that Li deposits are mainly comprised of metallic Li. After nitridation, the two characteristic peaks of Li are disappeared and four new peaks at 22.96°, 28.20°, 49.91° and 55.64° emerge in the XRD spectra, perfectly matching the four main crystalline faces of Li_3N (PDF#30-0759). Hence, after nitridation, the Li_3N is the main component in the sample. It could be concluded that by nitridation, the metallic Li in the deposits has been transformed into Li_3N. Thus, it can be confirmed that the Li deposits could be used for ammonia synthesis by the Li-mediated pathway.

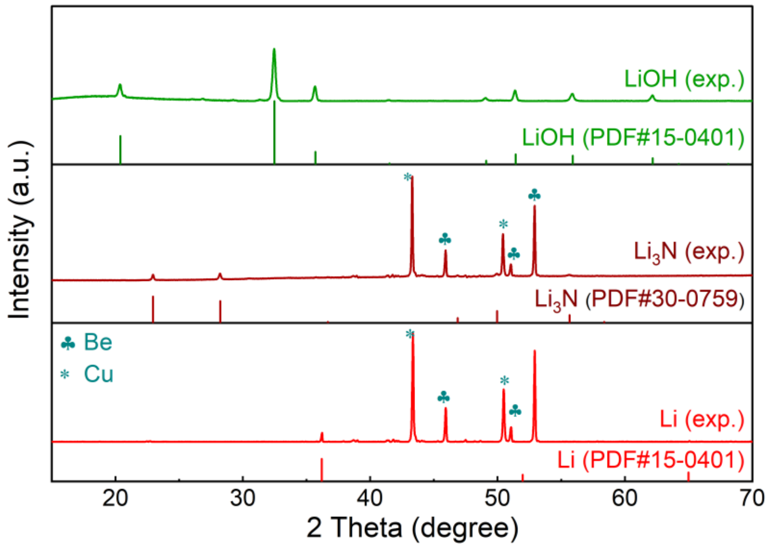

Figure 4.20 XRD patterns of Li deposits before and after complete nitridation at 100°C for 4 hours.

4.5.3 Ammonia production and recovery of LiOH

The Li deposits have been confirmed to be readily used for ammonia production by nitridation followed by hydrolysis. In fact, only “live” Li inside the Li deposits could serve as the reactive surface to reduce N_2. In previous section of Li plating, it has been concluded that the ratio of “live” Li, evaluated by Li plating efficiency, would increase with the plating capacity. Thus, for efficient ammonia synthesis, Li deposits with large capacity (>10 mAh cm^{-2}) were chosen for the Li-mediated pathway. To describe the overall efficiency in the Li-mediated ammonia synthesis, the concept of Faradic efficiency (FE) was introduced here as the reported research on Li-mediated ammonia synthesis,[12, 21] and calculated according to the following equation:

$$\mathrm{FE} = \frac{\text{effective amount of electrons for } \mathrm{NH_3} \text{ production}}{\text{total amount of electrons output}}$$

$$= \frac{\text{Amount of } \mathrm{NH_3}\ \text{(mol)} \times 96485\,\frac{\mathrm{C}}{\mathrm{mol\ e^-}}}{\text{Li plating capacity(mAh)} * \frac{3.6\mathrm{C}}{1\mathrm{mAh}} * \frac{1\mathrm{mol\ Li^0}}{1\mathrm{mol\ e^-}} * \frac{1\mathrm{mol\ NH_3}}{3\mathrm{mol\ Li^0}}} \qquad 4\text{-}13$$

To figure out the relationship between FE and Li plating capacity of deposits, Li deposits with different capacities (10-18 mAh cm^{-2}) were obtained from the LMB system and then nitrided for 4 hours for complete nitridation, followed by hydrolysis of Li_3N to release ammonia. The FE is calculated as Eq.4-18. The relationship plot between FE and plating capacity is shown in Figure 4.21. It can be observed that when Li plating capacities are more than 10 mAh cm^{-2}, FEs from all deposits exhibit a high value over 75%. With the increase of capacity, the FE gradually increases and at the plating capacity of 17.5 mAh cm^{-2}, the value even reaches more than 92%. The value reported here is one of the best performances in NH_3 electro-synthesis as listed in the Table 4-2. It can be predicted that with the further increase of Li plating capacity, the FE of the system can even be higher. Thus, the LMB-mimic system has the potential to produce ammonia efficiently by the Li-mediated pathway.

The FE of the stepwise Li-mediated process is calculated as the utilization efficiency of the input electrons to produce ammonia. The input electrons are utilized to produce Li deposits and stored in "live" Li. The "live" Li could dissociate N_2 molecules in the nitridation, producing Li_3N. Ammonia is formed from nitride by hydrolysis. The electron-transfer efficiency of nitridation and hydrolysis is 100%, and no other electrons are input in these two stages. The FE of the Li-mediated process is only related to the electron utilization efficiency of Li plating and depends on the ratio of "live" Li in the deposits. The larger the ratio of "live" Li in the deposits, the higher FE of the Li-mediated process would be.

The high FE values of the present Li-mediated process are ascribed to the high efficiency of producing "live" Li by the LMB-mimic system. Li plating is separated into two steps, Li^+ recovery and Li plating steps in the LMB system. Li^+ is extracted by the Li recovery electrode and released into the LMB system. This stepwise manner could effectively separate the electrons and the "live" Li from being consumed by water molecules. Furthermore, in the LMB system, Li^+ would be electro-plated into metallic Li in the organic electrolyte. At the very beginning, the Li deposits are reactive and would be consumed by the electrolyte, forming an SEI layer on the outer surface of the Li deposits. Such an SEI layer could protect the Li plating reaction and "live" Li products beneath the layer, thus ensuring high electron utilization efficiency. The LMB-mimic system's design and the SEI layer's protective function make it efficient to utilize the input electrons to produce "live" Li.

The increasing FE with Li plating capacity is thought to be caused by the increasing ratio of "live" Li in the deposits. During the Li plating step in present Li plating, electrons are supplied from the outer circuit, and Li^+ is released from the Li recovery electrode. The Li^+ from the electrode pass through the electrolyte and across the outer SEI layer, accepting electrons on the electrode to form "live" Li. The formed SEI is stable and could protect the inner electrons transfer and "live" Li from consumption. Thus, with the Li plating capacity increased, more "live" Li would accumulate beneath the protective SEI layer. Because the formation of the SEI layer only consumes a limited amount of "live" Li, the ratio of "live" Li in the deposits would increase significantly with the plating capacity. Thus, the FE could be greatly improved with increased Li plating capacity, as illustrated in Figure 4.20.

The slight loss in FE is believed to ascribe to the following reasons: (1) consumed by intrinsic SEI formation during Li plating, as well as the newly formed SEI during operation, for example, during the opening of the coin cells, the mechanical force was applied on the fragile SEI layer. Thus, fresh Li will be exposed to the electrolyte and consumed. (2) because of the poor adhesive force to the Cu foil, some Li deposits may be peeled off during operation. (3) the exposure of Li or Li_3N to the air, especially during the transfer of Li_3N for hydrolysis.

The NH_3 synthesis rate is calculated according to Eq.4-24.[19] Compared to the time for Li plating or nitridation, the hydrolysis duration can be neglected. Thus, in the equation, only duration of plating and nitridation are counted into the time. Herein, the Li deposits of 17.46 mAh cm^{-2}, are selected as an example for calculating the ammonia production rate. It was measured through the Li-mediated pathway, the deposit could be converted into 0.472 mmol of NH_3. Combined with the Li plating duration of 23.28 hours and the nitridation time of 23.28 hours, the NH_3 synthesis rate is calculated to be 6.12 nmol s^{-1} cm^{-2}. But this rate can be further enhanced by improving the three sub-processes simultaneously or separately, such as accelerating the nitridation process[122] or plating Li at higher current density.

NH_3 synthesis rate (mol s^{-1} cm^{-2}) =

$$\frac{\text{Amount of } \mathrm{NH_3} \text{ (mol)}}{\text{Working area (cm2)(Li plating time +nitridation time)(s)}} \qquad \text{4-14}$$

LiOH was recovered from the solution after ammonia formation to confirm and complete the Li-mediated cycle. The LiOH recovery was achieved by evaporating H_2O from the solution in a boat within the flowing N_2 atmosphere (120°C; 4 hours). (Figure 3.2a). XRD was then used to characterize the obtained LiOH recovery sample. As illustrated in Figure 4.20, the spectrum of the recovered LiOH corresponded well to the standard one of LiOH, and no other peaks could be observed. The result indicates that the recovered sample is mainly composed of LiOH. Consequently, by adding the LiOH back in the following Li-mediated process, we establish a cyclic Li-mediated ammonia electro-synthesis.

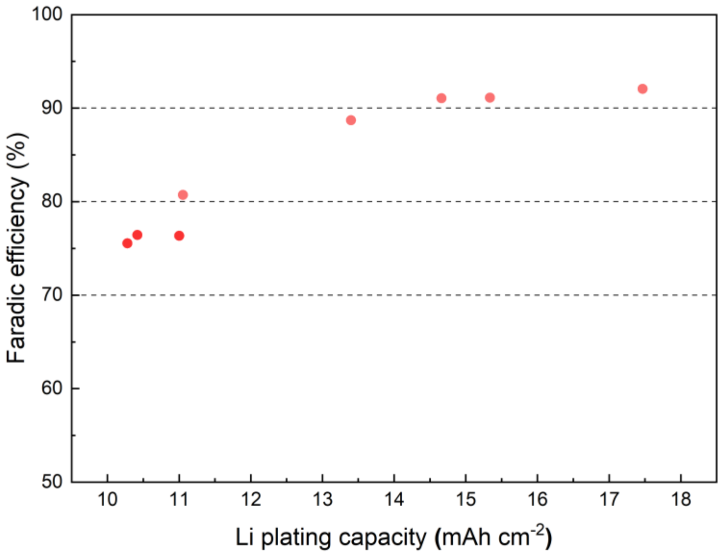

Figure 4.21 Faradaic efficiencies using Li deposits with various capacities

4.6 Control experiment

In this study, particular attention was paid to systematically prove that N_2 is the dominant nitrogen source for NH_3 synthesis.[16, 123] Several rigorous control and confirmatory experiments were carried out specifically in the stage of nitridation. As shown in Figure 4.22,the replacement of Li deposit under N_2 flow with Argon or no gas treatment resulted in negligible NH_3 synthesis. Only the exposure of N_2 to metallic Li led to NH_3 production, confirming that the formation of Li_3N is unquestionably attributed to the bulk reaction between metallic Li and N_2. Herein, the amount of NH_3 produced is in large amount of 0.18 mmol, compared to the control group. And because similar Li-mediated method has been widely proved to be reliable for ammonia,[16, 19, 21] no further isotope labelled quantification was implemented on our Li-mediated ammonia synthesis. Thus, all these stringent control experiments prove that, in the Li-mediated method based on our LMB-mimic system, the NH_3 is synthesized with N_2 as the only nitrogen source.

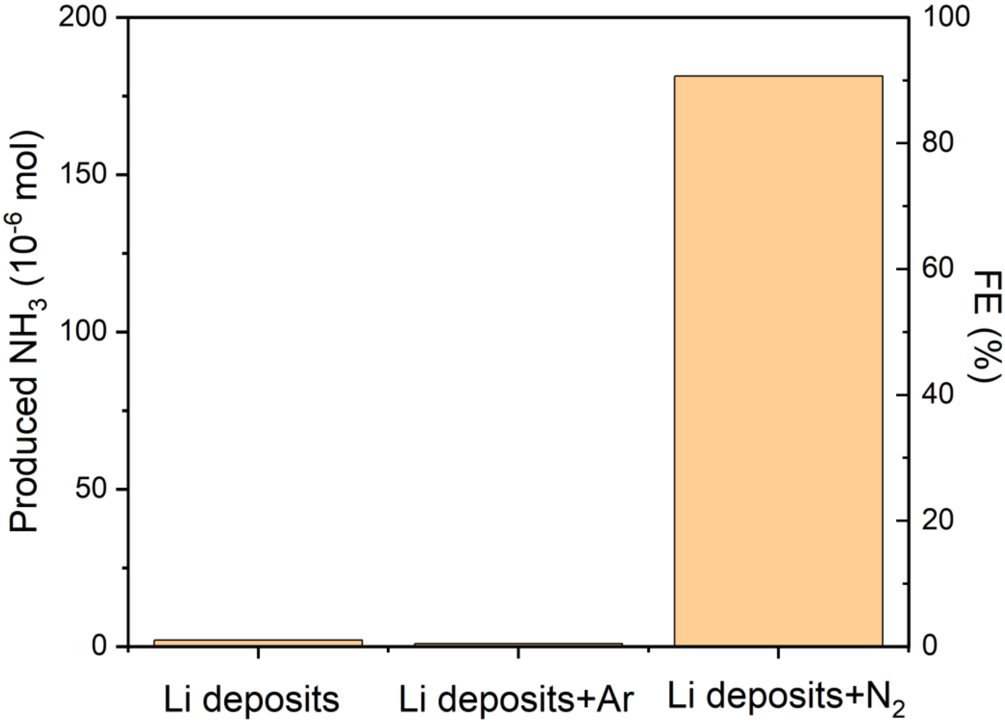

Figure 4.22 The amount of synthesized NH_3 and corresponding FEs of bare Li deposit, Li deposit reacted with Ar and N_2 under 100°C for 4 hours. (Li deposits from the LMB system with capacity of 20 mAh cm^{-2} for all cases.)

4.7 Performance comparison with relevant research

Li-mediated ammonia synthesis is a promising alternative to HBP process because of its sustainable process and mild operation conditions. Utilizing highly reactive metallic Li as the mediator, the Li-mediated method could easily split N_2 molecules under ambient conditions, producing Li_3N. Followed by reacting with protons, ammonia could be produced and Li^+ would be regenerated. The whole process is typically summarized as three sub-steps, including nitridation, protonation, as well as NH_3 formation. Ideally, the Li-mediated method could utilize sustainable electricity as the energy input and H_2O as the proton source. Herein, the Li-mediated ammonia synthesis, including both the continuous and stepwise ones, are summarized, and compared in Table 4-2.

In the continuous Li-mediated method, three steps occur in the same system simultaneously. Thus, to avoid the assumption of active Li, usually less reactive proton source, such as low-concentration ethanol in non-protic electrolyte, often serves as the protons source, instead of H_2O. Despite this, side reactions, between Li and electrolyte, still cannot be avoided and occur when the Li meets electrolyte, forming accumulated SEI layer. Thus, as illustrated in Table 4-2 most research on continuous Li-mediated methods shows a relatively low FE than the stepwise ones. In recent years, several novel strategies have been proposed to improve the FE with new electrolyte and SEI modification. Through these efforts, the FE could reach 69±7%. However, the continuous operation time for NH_3 production is typically short and some of them even can only be operated for several minutes. It has been reported that the short operation time was caused by the accumulation of SEI layer on electrode, increasing the polarization of the system and finally destroying it. Thus, future works on the SEI engineering is still required.

Table 4-2 Recent publications on Li-mediated ammonia synthesis (including both continuous and stepwise) (RT: room temperature)

	Ref.	Proton source	P_{N2} (MPa)	Plate /nitridation temperature (℃)	r_{NH3} (nmol s^{-1} cm^{-2})	Time (hour)	FE (%)
Continuous	2020[68]	1 vol.% EtOH	1	RT	0.7	~50	37.00
	2020[73]	0.1 M EtOH	0.1	RT	30	0.08	35±6
					13	2.17	18.90
	2019[67]	0.1 M EtOH	0.1	RT	5.12±0.81	0.25	18.5±2.9
	1993[70]	1 vol.% EtOH	0.1	RT	-	-	8.40
	2021[75]	1 vol.% EtOH	0.1	RT	0.75	0.5	34.00
	2019[16]	1 vol.% EtOH	0.1	RT	7.5	-	7.5
	2020[72]	2 vol.% EtOH	0.1	RT	-	2	5.00
	2022[74]	1 vol.% EtOH	2	RT	11.09	<2	78.00
	2022[12]	0.05 MPa H_2	1.95	RT	53±1	20	69±7
				RT	42	2	50.00
Stepwise	2017[20]	H_2O	0.1	450/100	9.2 *12hr nitridation*	0.278	88.5
	2019[19]	H_2O	0.1	RT/180	1.21	0.167	57.2
	2018[21]	H_2O	0.1	RT/220	1.88	0.111	49.93
	2018[66]	H_2O	0.1	RT/220	1.727 *estimated*	0.278	82.3
	This work	H_2O	0.1	RT/100	6.12 *4hr nitridation*	~23 ×20 cycle	92.12

Compared to the continuous Li-mediated method, the stepwise could directly use the sustainable H_2O as the protons source. And because the three steps were separated, Li would be less consumed by side reaction, thus the FE typically is larger. According to the table, most studies could obtain a high FE over 50%. In the Nørskov's study, this value could even reach 88.5%. In his study, the Li was plated under 450°C. Such high temperature will undoubtedly increase the energy consumption and improve the requirement on equipment, thus increasing the cost. In other stepwise research, even though the Li was plated from aqueous solution under room temperature, the system can only deliver a relatively low FE compared to Nørskov's research. And because the Li is highly reactive, the Li plating step is questionably stable, and all the research only operated for limited time (<0.5 hour).

In present study, based on the efficient and stable LMB-mimic system, the FE towards NH_3 could reach 92.12 %. Such high value shows the system could efficiently utilize the electric energy to produce ammonia. Furthermore, the system could be operated to plate Li metals for at least over 400 hours, which confirms the excellent stability of the system. Consequently, the Li-mediated method in the study, can electro-synthesize sustainable ammonia stably and efficiently in a sustainable way at atmospheric pressure and near ambient temperature (<100 °C), which is among the best reported results.

4.8 Conceptual Design of a Potential Cyclic Device

In the previous section, the Li-mediated process based on the LMB-mimic system has been confirmed theoretically and experimentally feasible for ammonia production. The conceptual device system based on the cyclic Li-mediated process was designed and proposed to confirm its practical feasibility, as illustrated in Figure 4.23. The system is composed of two reaction chambers and a vacuum oven. The Li plating steps and nitridation occur in Chamber I. Ammonia formation and Li^+ recovery would happen in Chamber II. The operation procedures in detail are listed as follows:

Li plating:
1. Assemble the Cu and LMO electrodes in Chamber I.
2. Open Valve 1 and pump enough electrolytes into the chamber.
3. Close Valve 1.
4. Connect the electrode to the power source and charge the cell chamber to 4.3V.
5. After Li plating, open Valve 2 to release the electrolyte out and store it.

Nitridation:
1. Open Valve 3&4.
2. Pump the nitrogen gas into the chamber. If needed, the nitrogen gas could be heated before pumping in. Keep the gas flowing during nitridation.
3. After nitridation, stop nitrogen pumping
4. Transfer the nitride electrode and $L_{1-x}MO$ to Chamber II.

Ammonia formation and Li^+ recovery:
1. Open Valve 1 and pump water into Chamber II. If needed, additional LiOH could be added.
2. After the reaction, transfer the electrode to the vacuum oven.

Electrode drying:
1. Dry the electrode in the vacuum oven under 100 °C.
2. The electrode could be used for Li plating in the next Li-mediated cycle.

By such a design, the Li plating process and Li deposits would be separated from the water solution. Thus, the conceptual device system could deliver an efficient ammonia production performance. Furthermore, after electrode drying, both the Cu electrode and LMO electrode are reusable and could be utilized for the next-cycle Li-mediated process. The device system could electro-synthesize ammonia from N_2 and H_2O in a cyclic manner.

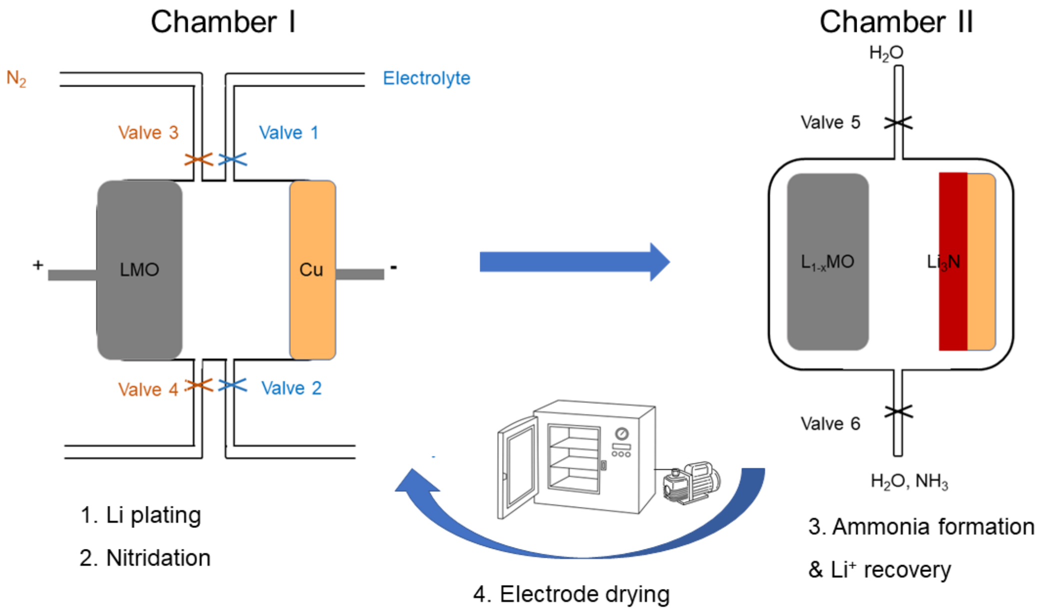

Figure 4.23 Conceptual design of the device for cyclic ammonia production

4.9 Summary

This chapter reports the LMB-mimic strategies for plate Li from LiOH under the ambient condition to sustain the cyclic Li-mediated ammonia electro-synthesis from N_2 and H_2O. Three major parts have been investigated: (1) designed and preparation of stable and reversible Li recovery electrode for the LMB-mimic system; (2) parameters optimization for efficient Li plating by the LMB-mimic system; (3) optimal conditions exploration for high-efficiency ammonia synthesis by the Li-mediated pathway.

In designing and preparing the Li recovery electrode, the free-standing Li recovery electrode, FS-L_{1-x}MO, has been designed and confirmed to be reversible and efficient for Li plating in the LMB-mimic system. Two conclusions can be drawn: Firstly, $Li_{1-x}Mn_2O_4$($0<x<1$) can be converted into $LiMn_2O_4$ in LiOH solution by Li^+ spontaneously intercalated into the lattice of $LiMn_2O_4$, confirmed by a thermodynamic evaluation. Secondly, $LiMn_2O_4$ can deliver a reversible and large Li^+ intercalation/de-intercalation capacity of around 0.75Li^+, which has been confirmed by the cycling performance of Li/$LiMn_2O_4$. Furthermore, fabricated from $LiMn_2O_4$, the free-standing electrode, FS-L_{1-x}MO, was confirmed experimentally can deliver an extensive and reversible Li plating by the reversible Li^+ intercalation/de-intercalation into/from $LiMn_2O_4$ in the LMB-mimic system.

By tuning the mass loading of $LiMn_2O_4$ in FS-L_{1-x}MO, different Li plating capacities can be obtained by the Li recovery-plating cycle with the LMB-mimic system. It was found that the plating efficiency can be continuously increased with the increasing Li plating capacity. When the Li plating capacity is over 12.65 mAh cm^{-2}, a high Li plating efficiency can be obtained. With the increase of Li plating capacity, the efficiency could reach its limit value of 100%. The phenomenon of Li plating efficiency increasing with capacity was caused by the decrease of porosity with increasing capacity and the protective function of the SEI layer, confirmed by the SEM images and In-depth XPS profiling.

For optimizing the Li-mediated ammonia synthesis, the influences of several essential parameters, including the nitridation temperature and Li plating capacity, are explored in this study. To find out the optimal temperature for nitridation, commercial Li foil was exposed to a flowing N_2 atmosphere under different temperatures of 25, 50, 75, and 100 °C. It was confirmed that under 100 °C, the nitridation rate is the largest among these temperatures. Under the optimized temperature, Li deposits, with different plating capacities, are utilized for ammonia production by the Li-mediated method. It was found that, the FEs of ammonia synthesis increase with the plating capacities of these Li deposits, similar to the trend of Li plating efficiency with capacity. When the plating efficiency was more than 15 mAh cm^{-2}, the FE could reach a high value of over 92%, which is among the best results in the reported literature.

To confirm the ammonia is produced solely from the supplied N_2, the control experiments are implemented in this study. It could be directly observed that only when the Li deposits react with N_2, the ammonia could be detected in large quantality, compared to the negligible results from deposit itself or from deposits with Ar. Thus, the ammonia is proved to be produced from the Li deposits reacting with N_2, rather than from the environmental N containments. Combined with the high FE value in present study, the Li-mediated approach based on our LMB-mimic system is confirmed to be efficient to produce ammonia from N_2.

Chapter 5 Conclusion

5.1 Contributions to Knowledge

Aiming to continuously synthesize ammonia by the Li-mediated pathway, a novel LMB-mimic system has been designed and prepared to plate metallic Li efficiently and stably from LiOH under ambient pressure. Based on the research findings, the following contributions to knowledge have been achieved:

1. The concept of using an LMB-mimic system was proved for efficient and stable Li plating from LiOH.
2. The LMB-mimic system was tested using the cheap and abundant manganese oxide as a free-standing cathode material, FS-LMO. Specially, $LiMn_2O_4$ can deliver a reversible and large Li^+ intercalation/de-intercalation capacity of around $0.75Li^+$. For a large value of Li plating efficiency, the plating capacity should be controlled and located above the value of 12.65 mAh cm^{-2}.
3. The lithium metal harvested from the LiOH solution was confirmed to be active in reacting with nitrogen to form Li_3N which can react with H_2O to produce NH_3 and LiOH. The SEI layer formed has significant effect.
4. The close loop from Li metal harness to ammonia production was examined in terms of Faradic efficiency for the electricity consumed. For the present system, 92% was found, when the plating capacity over 15 mAh cm^{-2} was applied.

5.2 Suggestions for Future Work

Based on the findings of the thesis, the following future work is suggested：

1. Exploring possible alternatives to $LiMn_2O_4$ for larger reversible Li^+ capacity

It was found that $LiMn_2O_4$ could be fabricated into an electrode to move the Li^+ from the LiOH solution to the LMB system. For a larger Li plating capacity, other cathode materials can be explored. For an ideal candidate, firstly, it is better to be stable in both aqueous and organic solutions for continuous Li recovery and plating. Secondly, it should have a large Li^+ intercalation/de-intercalation capacity. Meanwhile, its equilibrium potential for spontaneous Li recovery should be located below its electrochemical potential.

2. Electrolyte engineering for the LMB system

In this thesis, it was found that both the morphology and the SEI formation play an essential role during Li plating. It is believed that the surface exposure would increase the Li consumption, and the SEI layer formed should protect the inner metallic Li. Considering the recent developments on LMB, it is suggested that engineering the morphology and SEI layer could effectively optimize the Li plating process, thus improving the ammonia synthesis by the Li-mediated pathway. It is not clear if the formed SEI layer can be repeatedly utilized in the Li metal harvesting, or it should be removed from the system periodically for the efficient operation. This should be checked out carefully.

3. Mechanism understanding of Li plating and nitridation

In the LMB-mimic system, Li plating in the system is stable and efficient. For better operating the system, it is suggested here to elucidate the profound reason why it is suitable for Li plating. Furthermore, it could be found that in the Li-mediated ammonia synthesis, the nitridation process is slow and less understood. To better improve this process, the mechanism of Li splitting the N_2 molecules should be better explored so as to improve the step for efficient ammonia synthesis.

4. Device design for practical ammonia production

A novel conceptual system for ammonia production has been confirmed in this thesis. For the system to produce ammonia in large quantities, it is required to integrate the steps involved in the system for industrial ammonia production. This should be investigated in a pilot plant before practical implementation of the system to benefit the society.

REFERENCES

[1]. Nitrogen Cycle. https://www.sciencefacts.net/nitrogen-cycle.html (accessed January 27, 2023).

[2]. Kandemir, T.; Schuster, M. E.; Senyshyn, A.; Behrens, M.; Schlogl, R., The Haber-Bosch process revisited: on the real structure and stability of "ammonia iron" under working conditions. *Angewandte Chemie. International Edition in English* **2013,** *52* (48), 12723-6.

[3]. Cheng, X. B.; Zhang, R.; Zhao, C. Z.; Wei, F.; Zhang, J. G.; Zhang, Q., A Review of Solid Electrolyte Interphases on Lithium Metal Anode. *Advanced science (Weinheim, Baden-Württemberg, Germany)* **2016,** *3* (3), 1500213.

[4]. Smil, V., Detonator of the population explosion. *Nature* **1999,** *400* (6743), 415-415.

[5]. Erisman, J. W.; Sutton, M. A.; Galloway, J.; Klimont, Z.; Winiwarter, W., How a century of ammonia synthesis changed the world. *Nature Geoscience* **2008,** *1* (10), 636-639.

[6]. Qin, Q.; Oschatz, M., Overcoming chemical inertness under ambient conditions: a critical view on recent developments in ammonia synthesis via electrochemical N_2 reduction by asking five questions. *ChemElectroChem* **2020,** *7* (4), 878-889.

[7]. Bartels, J. R., *A feasibility study of implementing an Ammonia Economy*. Iowa State University: **2008**.

[8]. Renner, J. N.; Greenlee, L. F.; Ayres, K. E.; Herring, A. M., Electrochemical synthesis of ammonia: a low pressure, low temperature approach. *The Electrochemical Society Interface* **2015,** *24* (2), 51.

[9]. Lan, R.; Irvine, J. T.; Tao, S., Synthesis of ammonia directly from air and water at ambient temperature and pressure. *Scientific Reports* **2013,** *3* (1), 1145.

[10]. Secretariat, I., Aviation’s contribution to Climate Change. *BAN Ki-moon* **2010**.

[11]. Soloveichik, G., Electrochemical synthesis of ammonia as a potential alternative to the Haber-Bosch process. *Nature Catalysis* **2019,** *2* (5), 377-380.

[12]. Suryanto, B. H. R.; Matuszek, K.; Choi, J.; Hodgetts, R. Y.; Du, H. L.; Bakker, J. M.; Kang, C. S. M.; Cherepanov, P. V.; Simonov, A. N.; MacFarlane, D. R., Nitrogen reduction to ammonia at high efficiency and rates based on a phosphonium proton shuttle. *Science* **2021,** *372* (6547), 1187-1191.

[13]. Foster, S. L.; Bakovic, S. I. P.; Duda, R. D.; Maheshwari, S.; Milton, R. D.; Minteer, S. D.; Janik, M. J.; Renner, J. N.; Greenlee, L. F., Catalysts for nitrogen reduction to ammonia. *Nature Catalysis* **2018,** *1* (7), 490-500.

[14]. Chen, J. G.; Crooks, R. M.; Seefeldt, L. C.; Bren, K. L.; Bullock, R. M.; Darensbourg, M. Y.; Holland, P. L.; Hoffman, B.; Janik, M. J.; Jones, A. K.; Kanatzidis, M. G.; King, P.; Lancaster, K. M.; Lymar, S. V.; Pfromm, P.; Schneider, W. F.; Schrock, R. R., Beyond fossil fuel-driven nitrogen transformations. *Science* **2018,** *360* (6391).

[15]. Shi, L.; Yin, Y.; Wang, S.; Sun, H., Rational catalyst design for N_2 reduction under ambient conditions: strategies toward enhanced conversion efficiency. *ACS Catalysis* **2020,** *10* (12), 6870-6899.

[16]. Andersen, S. Z.; Colic, V.; Yang, S.; Schwalbe, J. A.; Nielander, A. C.; McEnaney, J. M.; Enemark-Rasmussen, K.; Baker, J. G.; Singh, A. R.; Rohr, B. A.; Statt, M. J.; Blair, S. J.; Mezzavilla, S.; Kibsgaard, J.; Vesborg, P. C. K.; Cargnello, M.; Bent, S. F.; Jaramillo, T. F.; Stephens, I. E. L.; Norskov, J. K.; Chorkendorff, I., A rigorous electrochemical ammonia synthesis protocol with quantitative isotope measurements. *Nature* **2019,** *570* (7762), 504-508.

[17]. Hu, L.; Xing, Z.; Feng, X. F., Understanding the Electrocatalytic Interface for Ambient Ammonia Synthesis. *ACS Energy Letters* **2020,** *5* (2), 430-+.

[18]. Ma, J. L.; Bao, D.; Shi, M. M.; Yan, J. M.; Zhang, X. B., Reversible Nitrogen Fixation Based on a Rechargeable Lithium-Nitrogen Battery for Energy Storage. *Chem* **2017,** *2* (4), 525-532.

[19]. Kim, K.; Chen, Y. F.; Han, J. I.; Yoon, H. C.; Li, W. Z., Lithium-mediated ammonia synthesis from water and nitrogen: a membrane-free approach enabled by an immiscible aqueous/organic hybrid electrolyte system. *Green Chemistry* **2019,** *21* (14), 3839-3845.

[20]. McEnaney, J. M.; Singh, A. R.; Schwalbe, J. A.; Kibsgaard, J.; Lin, J. C.; Cargnello, M.; Jaramillo, T. F.; Nørskov, J. K., Ammonia synthesis from N_2 and H_2O using a lithium cycling electrification strategy at atmospheric pressure. *Energy & Environmental Science* **2017,** *10* (7), 1621-1630.

[21]. Kim, K.; Lee, S. J.; Kim, D. Y.; Yoo, C. Y.; Choi, J. W.; Kim, J. N.; Woo, Y.; Yoon, H. C.; Han, J. I., Electrochemical Synthesis of Ammonia from Water and Nitrogen: A Lithium-Mediated Approach Using Lithium-Ion Conducting

Glass Ceramics. *ChemSusChem* **2018,** *11* (1), 120-124.

[22]. Smith, C.; Hill, A. K.; Torrente-Murciano, L., Current and future role of Haber-Bosch ammonia in a carbon-free energy landscape. *Energy & Environmental Science* **2020,** *13* (2), 331-344.

[23]. Valera-Medina, A.; Banares-Alcantara, R., *Techno-economic challenges of green ammonia as an energy vector*. Academic Press: **2020**.

[24]. Smil, V., *Enriching the earth: Fritz Haber, Carl Bosch, and the transformation of world food production*. MIT press: **2004**.

[25]. Bicer, Y.; Dincer, I.; Zamfirescu, C.; Vezina, G.; Raso, F., Comparative life cycle assessment of various ammonia production methods. *Journal of Cleaner Production* **2016,** *135*, 1379-1395.

[26]. Appl, M., Ammonia, 2. Production Processes. In *Ullmann's Encyclopedia of Industrial Chemistry*, 2011.

[27]. Rouwenhorst, K. H. R.; Engelmann, Y.; van 't Veer, K.; Postma, R. S.; Bogaerts, A.; Lefferts, L., Plasma-driven catalysis: green ammonia synthesis with intermittent electricity. *Green Chemistry* **2020,** *22* (19), 6258-6287.

[28]. Lim, J.; Fernandez, C. A.; Lee, S. W.; Hatzell, M. C., Ammonia and Nitric Acid Demands for Fertilizer Use in 2050. *ACS Energy Letters* **2021,** *6* (10), 3676-3685.

[29]. Giddey, S.; Badwal, S. P. S.; Munnings, C.; Dolan, M., Ammonia as a Renewable Energy Transportation Media. *ACS Sustainable Chemistry & Engineering* **2017,** *5* (11), 10231-10239.

[30]. Licht, S.; Cui, B.; Wang, B.; Li, F.-F.; Lau, J.; Liu, S., Ammonia synthesis by N_2 and steam electrolysis in molten hydroxide suspensions of nanoscale Fe_2O_3. *Science* **2014,** *345* (6197), 637-640.

[31]. van der Ham, C. J.; Koper, M. T.; Hetterscheid, D. G., Challenges in reduction of dinitrogen by proton and electron transfer. *Chemical Society Reviews* **2014,** *43* (15), 5183-91.

[32]. Nagaoka, K.; Eboshi, T.; Takeishi, Y.; Tasaki, R.; Honda, K.; Imamura, K.; Sato, K., Carbon-free H_2 production from ammonia triggered at room temperature with an acidic $RuO_2/\gamma\text{-}Al_2O_3$ catalyst. *Science advances* **2017,** *3* (4), e1602747.

[33]. Haber, F., The synthesis of ammonia from its elements. *Nobel Lecture* **1920,** *2*.

[34]. Ley, C.; Elvers, B.; Bellussi, G.; Bus, J.; Drauz, K.; Greim, H.; Hessel, V.; Kleemann, A.; Kutscher, B.; Meijer, G., *Ullmann's encyclopedia of industrial chemistry*. Wiley Online Library: **2010**.

[35]. Liu, H., *Ammonia synthesis catalysts: innovation and practice*. World Scientific: **2013**.

[36]. Ertl, G., Surface science and catalysis—studies on the mechanism of ammonia synthesis: the PH Emmett award address. *Catalysis Reviews Science and Engineering* **1980,** *21* (2), 201-223.

[37]. Boudart, M., Ammonia synthesis: the bellwether reaction in heterogeneous catalysis. *Topics in Catalysis* **1994,** *1* (3-4), 405-414.

[38]. Ozaki, A.; Taylor, H. S.; Boudart, M., Kinetics and mechanism of the ammonia synthesis. *Proceedings of the Royal Society of London. Series A. Mathematical and Physical Sciences* **1960,** *258* (1292), 47-62.

[39]. Mittasch, A.; Frankenburg, W., Early studies of multicomponent catalysts. In *Advances in Catalysis*, Elsevier: 1950; Vol. 2, pp 81-104.

[40]. Farber, E., From Chemistry to Philosophy: The Way of Alwin Mittasch (1869-1953). *Chymia* **1966,** *11*, 157-178.

[41]. Logadottir, A.; Rod, T. H.; Norskov, J. K.; Hammer, B.; Dahl, S.; Jacobsen, C. J. H., The Bronsted-Evans-Polanyi relation and the volcano plot for ammonia synthesis over transition metal catalysts. *Journal of Catalysis* **2001,** *197* (2), 229-231.

[42]. Jacobsen, C. J.; Dahl, S.; Clausen, B. S.; Bahn, S.; Logadottir, A.; Norskov, J. K., Catalyst design by interpolation in the periodic table: bimetallic ammonia synthesis catalysts. *Journal of the American Chemical Society* **2001,** *123* (34), 8404-5.

[43]. Wang, P.; Chang, F.; Gao, W.; Guo, J.; Wu, G.; He, T.; Chen, P., Breaking scaling relations to achieve low-temperature ammonia synthesis through LiH-mediated nitrogen transfer and hydrogenation. *Nature Chemistry* **2017,** *9* (1), 64-70.

[44]. Wang, M.; Liu, S.; Qian, T.; Liu, J.; Zhou, J.; Ji, H.; Xiong, J.; Zhong, J.; Yan, C., Over 56.55% Faradaic efficiency of ambient ammonia synthesis enabled by positively shifting the reaction potential. *Nature Communications* **2019,** *10* (1), 341.

[45]. Medford, A. J.; Vojvodic, A.; Hummelshoj, J. S.; Voss, J.; Abild-Pedersen, F.; Studt, F.; Bligaard, T.; Nilsson, A.; Norskov, J. K., From the Sabatier principle to a predictive theory of transition-metal heterogeneous catalysis. *Journal of Catalysis* **2015,** *328,* 36-42.

[46]. Smart, K., Review of Recent Progress in Green Ammonia Synthesis Decarbonisation of fertiliser and fuels via green synthesis. *Johnson Matthey Technology Review* **2022,** *66* (3), 230-244.

[47]. Qing, G.; Ghazfar, R.; Jackowski, S. T.; Habibzadeh, F.; Ashtiani, M. M.; Chen, C. P.; Smith, M. R., 3rd; Hamann, T. W., Recent Advances and Challenges of Electrocatalytic N_2 Reduction to Ammonia. *Chemical Reviews* **2020,** *120* (12), 5437-5516.

[48]. Janet, C.; Navaladian, S.; Viswanathan, B.; Varadarajan, T.; Viswanath, R., Heterogeneous wet chemical synthesis of superlattice-type hierarchical ZnO architectures for concurrent H_2 production and N_2 reduction. *The Journal of Physical Chemistry C* **2010,** *114* (6), 2622-2632.

[49]. Ying, Z.; Chen, S.; Zhang, S.; Peng, T.; Li, R., Efficiently enhanced N_2 photofixation performance of sea-urchin-like $W_{18}O_{49}$ microspheres with Mn-doping. *Applied Catalysis B: Environmental* **2019,** *254*, 351-359.

[50]. Zhang, N.; Li, L. G.; Shao, Q.; Zhu, T.; Huang, X. Q.; Xiao, X. H., Fe-Doped BiOCl Nanosheets with Light-Switchable Oxygen Vacancies for Photocatalytic Nitrogen Fixation. *ACS Applied Energy Materials* **2019,** *2* (12), 8394-8398.

[51]. Huang, Y. W.; Zhang, N.; Wu, Z. J.; Xie, X. Q., Artificial nitrogen fixation over bismuth-based photocatalysts: fundamentals and future perspectives. *Journal of Materials Chemistry A* **2020,** *8* (10), 4978-4995.

[52]. Cheng, M.; Xiao, C.; Xie, Y., Photocatalytic nitrogen fixation: the role of defects in photocatalysts. *Journal of Materials Chemistry A* **2019,** *7* (34), 19616-19633.

[53]. Guo, W.; Zhang, K.; Liang, Z.; Zou, R.; Xu, Q., Electrochemical nitrogen fixation and utilization: theories, advanced catalyst materials and system design. *Chemical Society Reviews* **2019,** *48* (24), 5658-5716.

[54]. Shipman, M. A.; Symes, M. D., Recent progress towards the electrosynthesis of ammonia from sustainable resources. *Catalysis Today* **2017,** *286*, 57-68.

[55]. Chen, S.; Liu, D.; Peng, T., Fundamentals and Recent Progress of

Photocatalytic Nitrogen-Fixation Reaction over Semiconductors. *Solar Rrl* **2021,** *5* (2), 2000487.

[56]. Ithisuphalap, K.; Zhang, H. G.; Guo, L.; Yang, Q. G.; Yang, H. P.; Wu, G., Photocatalysis and Photoelectrocatalysis Methods of Nitrogen Reduction for Sustainable Ammonia Synthesis. *Small Methods* **2019,** *3* (6), 1800352.

[57]. Marnellos, G.; Stoukides, M., Ammonia synthesis at atmospheric pressure. *Science* **1998,** *282* (5386), 98-100.

[58]. Graça, V. C.; Loureiro, F. J.; Holz, L. I.; Mikhalev, S. M.; Araújo, A. J.; Fagg, D. P., Electrochemical ammonia synthesis: Mechanism, recent developments, and challenges in catalyst design. *Heterogeneous Catalysis* **2022**, 497-514.

[59]. Skodra, A.; Stoukides, M., Electrocatalytic synthesis of ammonia from steam and nitrogen at atmospheric pressure. *Solid State Ionics* **2009,** *180* (23-25), 1332-1336.

[60]. Kyriakou, V.; Garagounis, I.; Vasileiou, E.; Vourros, A.; Stoukides, M., Progress in the Electrochemical Synthesis of Ammonia. *Catalysis Today* **2017,** *286*, 2-13.

[61]. Murakami, T.; Nishikiori, T.; Nohira, T.; Ito, Y., Electrolytic synthesis of ammonia in molten salts under atmospheric pressure. *Journal of the American Chemical Society* **2003,** *125* (2), 334-5.

[62]. Murakami, T.; Nohira, T.; Goto, T.; Ogata, Y. H.; Ito, Y., Electrolytic ammonia synthesis from water and nitrogen gas in molten salt under atmospheric pressure. *Electrochimica Acta* **2005,** *50* (27), 5423-5426.

[63]. Zhan, C. G.; Nichols, J. A.; Dixon, D. A., Ionization potential, electron affinity, electronegativity, hardness, and electron excitation energy: Molecular properties from density functional theory orbital energies. *Journal of Physical Chemistry A* **2003,** *107* (20), 4184-4195.

[64]. Jia, H. P.; Quadrelli, E. A., Mechanistic aspects of dinitrogen cleavage and hydrogenation to produce ammonia in catalysis and organometallic chemistry: relevance of metal hydride bonds and dihydrogen. *Chemical Society Reviews* **2014,** *43* (2), 547-64.

[65]. Tsuneto, A.; Kudo, A.; Sakata, T., Lithium-mediated electrochemical reduction of high pressure N_2 to NH_3. *Journal of Electroanalytical Chemistry* **1994,** *367* (1-2), 183-188.

[66]. Kim, K.; Cho, H.; Jeon, S. H.; Lee, S. J.; Yoo, C. Y.; Kim, J. N.; Choi, J. W.; Yoon, H. C.; Han, J. I., Lithium-Mediated Ammonia Electro-Synthesis: Effect of $CsClO_4$ on Lithium Plating Efficiency and Ammonia Synthesis. *Journal of the Electrochemical Society* **2018,** *165* (13), F1027-F1031.

[67]. Lazouski, N.; Schiffer, Z. J.; Williams, K.; Manthiram, K., Understanding Continuous Lithium-Mediated Electrochemical Nitrogen Reduction. *Joule* **2019,** *3* (4), 1127-1139.

[68]. Andersen, S. Z.; Statt, M. J.; Bukas, V. J.; Shapel, S. G.; Pedersen, J. B.; Krempl, K.; Saccoccio, M.; Chakraborty, D.; Kibsgaard, J.; Vesborg, P. C. K.; Norskov, J.; Chorkendorff, I., Increasing stability, efficiency, and fundamental understanding of lithium-mediated electrochemical nitrogen reduction. *Energy & Environmental Science* **2020,** *13* (11), 4291-4300.

[69]. Fichter, F.; Girard, P.; Erlenmeyer, H., Elektrolytische Bindung von komprimiertem Stickstoff bei gewöhnlicher Temperatur. *Helvetica Chimica Acta* **1930,** *13* (6), 1228-1236.

[70]. Tsuneto, A.; Kudo, A.; Sakata, T., Efficient Electrochemical Reduction of N_2 to NH_3 Catalyzed by Lithium. *Chemistry Letters* **1993,** *22* (5), 851-854.

[71]. Maheshwari, S.; Janik, M. J., Kinetics of Li-Mediated N_2 Electroreduction. *Joule* **2019,** *3* (4), 915-916.

[72]. Schwalbe, J. A.; Statt, M. J.; Chosy, C.; Singh, A. R.; Rohr, B. A.; Nielander, A. C.; Andersen, S. Z.; McEnaney, J. M.; Baker, J. G.; Jaramillo, T. F.; Norskov, J. K.; Cargnello, M., A Combined Theory-Experiment Analysis of the Surface Species in Lithium-Mediated NH_3 Electrosynthesis. *ChemElectroChem* **2020,** *7* (7), 1542-1549.

[73]. Lazouski, N.; Chung, M. J.; Williams, K.; Gala, M. L.; Manthiram, K., Non-aqueous gas diffusion electrodes for rapid ammonia synthesis from nitrogen and water-splitting-derived hydrogen. *Nature Catalysis* **2020,** *3* (5), 463-+.

[74]. Li, K.; Andersen, S. Z.; Statt, M. J.; Saccoccio, M.; Bukas, V. J.; Krempl, K.; Sazinas, R.; Pedersen, J. B.; Shadravan, V.; Zhou, Y.; Chakraborty, D.; Kibsgaard, J.; Vesborg, P. C. K.; Norskov, J. K.; Chorkendorff, I., Enhancement of lithium-mediated ammonia synthesis by addition of oxygen. *Science* **2021,** *374* (6575), 1593-1597.

[75]. Gao, L. F.; Cao, Y.; Wang, C.; Yu, X. W.; Li, W. B.; Zhou, Y.; Wang, B.;

Yao, Y. F.; Wu, C. P.; Luo, W. J.; Zou, Z. G., Domino Effect: Gold Electrocatalyzing Lithium Reduction to Accelerate Nitrogen Fixation. *Angewandte Chemie. International Edition in English* **2021,** *60* (10), 5257-5261.

[76]. Lin, D.; Liu, Y.; Cui, Y., Reviving the lithium metal anode for high-energy batteries. *Nature Nanotechnology* **2017,** *12* (3), 194-206.

[77]. Bruce, P. G.; Freunberger, S. A.; Hardwick, L. J.; Tarascon, J. M., Li-O_2 and Li-S batteries with high energy storage. *Nature Materials* **2011,** *11* (1), 19-29.

[78]. Wu, H. P.; Jia, H.; Wang, C. M.; Zhang, J. G.; Xu, W., Recent Progress in Understanding Solid Electrolyte Interphase on Lithium Metal Anodes. *Advanced Energy Materials* **2021,** *11* (5), 2003092.

[79]. Ooi, K.; Miyai, Y.; Katoh, S.; Maeda, H.; Abe, M., Topotactic lithium(1+) insertion to .lambda.-manganese dioxide in the aqueous phase. *Langmuir* **2002,** *5* (1), 150-157.

[80]. Zhao, A.; Liu, J.; Ai, X.; Yang, H.; Cao, Y., Highly Selective and Pollution-Free Electrochemical Extraction of Lithium by a Polyaniline/$Li_xMn_2O_4$ Cell. *ChemSusChem* **2019,** *12* (7), 1361-1367.

[81]. Wang, Y.; Chen, L.; Wang, Y.; Xia, Y., Cycling Stability of Spinel $LiMn_2O_4$ with Different Particle Sizes in Aqueous Electrolyte. *Electrochimica Acta* **2015,** *173*, 178-183.

[82]. Kim, D. K.; Muralidharan, P.; Lee, H. W.; Ruffo, R.; Yang, Y.; Chan, C. K.; Peng, H.; Huggins, R. A.; Cui, Y., Spinel $LiMn_2O_4$ nanorods as lithium ion battery cathodes. *Nano Letters* **2008,** *8* (11), 3948-52.

[83]. Ooi, K.; Miyai, Y.; Katoh, S.; Maeda, H.; Abe, M., Lithium-ion Insertion/Extraction Reaction with λ-MnO_2 in the Aqueous Phase. *Chemistry Letters* **1988,** *17* (6), 989-992.

[84]. Zhao, Y.; Shi, R.; Bian, X.; Zhou, C.; Zhao, Y.; Zhang, S.; Wu, F.; Waterhouse, G. I. N.; Wu, L. Z.; Tung, C. H.; Zhang, T., Ammonia Detection Methods in Photocatalytic and Electrocatalytic Experiments: How to Improve the Reliability of NH_3 Production Rates? *Adv Sci (Weinh)* **2019,** *6* (8), 1802109.

[85]. Zhao, Y.; Wu, F.; Miao, Y.; Zhou, C.; Xu, N.; Shi, R.; Wu, L. Z.; Tang, J.; Zhang, T., Revealing Ammonia Quantification Minefield in Photo/Electrocatalysis. *Angewandte Chemie. International Edition in English* **2021,** *60* (40), 21728-21731.

[86]. Giner-Sanz, J. J.; Leverick, G.; Perez-Herranz, V.; Shao-Horn, Y., Optimization of the salicylate method for ammonia quantification from nitrogen electroreduction. *Journal of Electroanalytical Chemistry* **2021,** *896,* 115250.

[87]. Searle, P. L., The Berthelot or Indophenol Reaction and Its Use in the Analytical-Chemistry of Nitrogen - a Review. *Analyst* **1984,** *109* (5), 549-568.

[88]. Van der Heide, P., *X-ray photoelectron spectroscopy: an introduction to principles and practices*. John Wiley & Sons: **2011**.

[89]. Ooi, K.; Miyai, Y.; Sakakihara, J., Mechanism of lithium(1+) insertion in spinel-type manganese oxide. Redox and ion-exchange reactions. *Langmuir* **2002,** *7* (6), 1167-1171.

[90]. Feng, Q.; Miyai, Y.; Kanoh, H.; Ooi, K., Lithium(1+) extraction/insertion with spinel-type lithium manganese oxides. Characterization of redox-type and ion-exchange-type sites. *Langmuir* **2002,** *8* (7), 1861-1867.

[91]. Luo, J. Y.; Cui, W. J.; He, P.; Xia, Y. Y., Raising the cycling stability of aqueous lithium-ion batteries by eliminating oxygen in the electrolyte. *Nature Chemistry* **2010,** *2* (9), 760-5.

[92]. Xiao, J.; Li, Q. Y.; Bi, Y. J.; Cai, M.; Dunn, B.; Glossmann, T.; Liu, J.; Osaka, T.; Sugiura, R.; Wu, B. B.; Yang, J. H.; Zhang, J. G.; Whittingham, M. S., Understanding and applying coulombic efficiency in lithium metal batteries. *Nature Energy* **2020,** *5* (8), 561-568.

[93]. Thackeray, M. M., Manganese oxides for lithium batteries. *Progress in Solid State Chemistry* **1997,** *25* (1-2), 1-71.

[94]. Tang, D. C.; Ben, L. B.; Sun, Y.; Chen, B.; Yang, Z. Z.; Gu, L.; Huang, X. J., Electrochemical behavior and surface structural change of $LiMn_2O_4$ charged to 5.1 V. *Journal of Materials Chemistry A* **2014,** *2* (35), 14519-14527.

[95]. Liu, T.; Dai, A.; Lu, J.; Yuan, Y.; Xiao, Y.; Yu, L.; Li, M.; Gim, J.; Ma, L.; Liu, J.; Zhan, C.; Li, L.; Zheng, J.; Ren, Y.; Wu, T.; Shahbazian-Yassar, R.; Wen, J.; Pan, F.; Amine, K., Correlation between manganese dissolution and dynamic phase stability in spinel-based lithium-ion battery. *Nature Communications* **2019,** *10* (1), 4721.

[96]. Zou, F.; Manthiram, A., A Review of the Design of Advanced Binders for High-Performance Batteries. *Advanced Energy Materials* **2020,** *10* (45), 2002508.

[97]. Gao, S. Y.; Su, Y. F.; Bao, L. Y.; Li, N.; Chen, L.; Zheng, Y.; Tian, J.; Li,

J.; Chen, S.; Wu, F., High-performance $LiFePO_4$/C electrode with polytetrafluoroethylene as an aqueous-based binder. *Journal of Power Sources* **2015,** *298*, 292-298.

[98]. Zhou, H. T.; Liu, M. H.; Gao, H. Q.; Hou, D.; Yu, C. C.; Liu, C.; Zhang, D.; Wu, J. C.; Yang, J. H.; Chen, D., Dense integration of solvent-free electrodes for Li-ion supercabattery with boosted low temperature performance. *Journal of Power Sources* **2020,** *473*, 228553.

[99]. Mitchell, P.; Xi, X.; Zhong, L.; Zou, B., Dry particle based electro-chemical device and methods of making same. Google Patents: 2005.

[100]. Tang, X. Y.; Zhou, J.; Bai, M.; Wu, W. W.; Li, S. W.; Ma, Y., Investigation of the self-discharge behaviors of the $LiMn_2O_4$ cathode at elevated temperatures: in situ X-ray diffraction analysis and a co-doping mitigation strategy. *Journal of Materials Chemistry A* **2019,** *7* (21), 13364-13371.

[101]. Tomon, C.; Sarawutanukul, S.; Phattharasupakun, N.; Duangdangchote, S.; Chomkhuntod, P.; Joraleechanchai, N.; Bunyanidhi, P.; Sawangphruk, M., Core-shell structure of $LiMn_2O_4$ cathode material reduces phase transition and Mn dissolution in Li-ion batteries. *Communications Chemistry* **2022,** *5* (1).

[102]. Lee, Y. J.; Wang, F.; Mukerjee, S.; McBreen, J.; Grey, C. P., ^{6}Li and ^{7}Li Magic-Angle Spinning Nuclear Magnetic Resonance and In Situ X-Ray Diffraction Studies of the Charging and Discharging of $Li_xMn_2O_4$ at 4 V. *Journal of the Electrochemical Society* **2000,** *147* (3), 803.

[103]. Paulsen, J. M.; Dahn, J. R., Phase diagram of Li-Mn-O spinel in air. *Chemistry of Materials* **1999,** *11* (11), 3065-3079.

[104]. Han, S. C.; Singh, S. P.; Hwang, Y.-h.; Bae, E. G.; Park, B. K.; Sohn, K.-S.; Pyo, M., Gadolinium-Doped $LiMn_2O_4$ Cathodes in Li Ion Batteries: Understanding the Stabilized Structure and Enhanced Electrochemical Kinetics. *Journal of the Electrochemical Society* **2012,** *159* (11), A1867-A1873.

[105]. Liu, J.; Bao, Z. N.; Cui, Y.; Dufek, E. J.; Goodenough, J. B.; Khalifah, P.; Li, Q. Y.; Liaw, B. Y.; Liu, P.; Manthiram, A.; Meng, Y. S.; Subramanian, V. R.; Toney, M. F.; Viswanathan, V. V.; Whittingham, M. S.; Xiao, J.; Xu, W.; Yang, J. H.; Yang, X. Q.; Zhang, J. G., Pathways for practical high-energy long-cycling lithium metal batteries. *Nature Energy* **2019,** *4* (3), 180-186.

[106]. Peled, E.; Menkin, S., Review-SEI: Past, Present and Future. *Journal of the*

Electrochemical Society **2017,** *164* (7), A1703-A1719.

[107]. Fang, C. C.; Lu, B. Y.; Pawar, G.; Zhang, M. H.; Cheng, D. Y.; Chen, S. R.; Ceja, M.; Doux, J. M.; Musrock, H.; Cai, M.; Liaw, B.; Meng, Y. S., Pressure-tailored lithium deposition and dissolution in lithium metal batteries. *Nature Energy* **2021,** *6* (10), 987-994.

[108]. Odziemkowski, M.; Irish, D., An electrochemical study of the reactivity at the lithium electrolyte/bare lithium metal interface: I. Purified electrolytes. *Journal of the Electrochemical Society* **1992,** *139* (11), 3063.

[109]. Oyakhire, S. T.; Gong, H. X.; Cui, Y.; Bao, Z. N.; Bent, S. F., An X-ray Photoelectron Spectroscopy Primer for Solid Electrolyte Interphase Characterization in Lithium Metal Anodes. *ACS Energy Letters* **2022,** *7* (8), 2540-2546.

[110]. Wood, S. M.; Pham, C. H.; Rodriguez, R.; Nathan, S. S.; Dolocan, A. D.; Celio, H.; de Souza, J. P.; Klavetter, K. C.; Heller, A.; Mullins, C. B., K^+ Reduces Lithium Dendrite Growth by Forming a Thin, Less-Resistive Solid Electrolyte Interphase. *ACS Energy Letters* **2016,** *1* (2), 414-419.

[111]. Herstedt, M.; Abraham, D. P.; Kerr, J. B.; Edstrom, K., X-ray photoelectron spectroscopy of negative electrodes from high-power lithium-ion cells showing various levels of power fade. *Electrochimica Acta* **2004,** *49* (28), 5097-5110.

[112]. Wang, Q.; Yao, Z.; Zhao, C.; Verhallen, T.; Tabor, D. P.; Liu, M.; Ooms, F.; Kang, F.; Aspuru-Guzik, A.; Hu, Y. S.; Wagemaker, M.; Li, B., Interface chemistry of an amide electrolyte for highly reversible lithium metal batteries. *Nature Communications* **2020,** *11* (1), 4188.

[113]. Kowalczyk, S.; Ley, L.; McFeely, F.; Pollak, R.; Shirley, D., X-ray photoemission from sodium and lithium. *Physical Review B* **1973,** *8* (8), 3583.

[114]. Fang, C.; Li, J.; Zhang, M.; Zhang, Y.; Yang, F.; Lee, J. Z.; Lee, M. H.; Alvarado, J.; Schroeder, M. A.; Yang, Y.; Lu, B.; Williams, N.; Ceja, M.; Yang, L.; Cai, M.; Gu, J.; Xu, K.; Wang, X.; Meng, Y. S., Quantifying inactive lithium in lithium metal batteries. *Nature* **2019,** *572* (7770), 511-515.

[115]. Wood, S. M.; Fang, C. C.; Dufek, E. J.; Nagpure, S. C.; Sazhin, S. V.; Liaw, B.; Meng, Y. S., Predicting Calendar Aging in Lithium Metal Secondary Batteries: The Impacts of Solid Electrolyte Interphase Composition and Stability. *Advanced Energy Materials* **2018,** *8* (26), 1801427.

[116]. Verma, P.; Maire, P.; Novak, P., A review of the features and analyses of the solid electrolyte interphase in Li-ion batteries. *Electrochimica Acta* **2010,** *55* (22), 6332-6341.

[117]. Otto, S. K.; Moryson, Y.; Krauskopf, T.; Peppler, K.; Sann, J.; Janek, J.; Henss, A., In-Depth Characterization of Lithium-Metal Surfaces with XPS and ToF-SIMS: Toward Better Understanding of the Passivation Layer. *Chemistry of Materials* **2021,** *33* (3), 859-867.

[118]. Zhang, X. Q.; Cheng, X. B.; Chen, X.; Yan, C.; Zhang, Q., Fluoroethylene Carbonate Additives to Render Uniform Li Deposits in Lithium Metal Batteries. *Advanced Functional Materials* **2017,** *27* (10), 1605989.

[119]. Kanamura, K.; Shiraishi, S.; Tamura, H.; Takehara, Z., X-Ray Photoelectron Spectroscopic Analysis and Scanning Electron-Microscopic Observation of the Lithium Surface Immersed in Nonaqueous Solvents. *Journal of the Electrochemical Society* **1994,** *141* (9), 2379-2385.

[120]. Bar-Tow, D.; Peled, E.; Burstein, L., A study of highly oriented pyrolytic graphite as a model for the graphite anode in Li-Ion batteries. *Journal of the Electrochemical Society* **1999,** *146* (3), 824.

[121]. Edström, K.; Herstedt, M.; Abraham, D. P., A new look at the solid electrolyte interphase on graphite anodes in Li-ion batteries. *Journal of Power Sources* **2006,** *153* (2), 380-384.

[122]. Zhang, Z.; Zhao, Y.; Sun, B.; Xu, J.; Jin, Q.; Lu, H.; Lyu, N.; Dang, Z. M.; Jin, Y., Copper Particle-Enhanced Lithium-Mediated Synthesis of Green Ammonia from Water and Nitrogen. *ACS Applied Materials & Interfaces* **2022,** *14* (17), 19419-19425.

[123]. Suryanto, B. H. R.; Du, H. L.; Wang, D. B.; Chen, J.; Simonov, A. N.; MacFarlane, D. R., Challenges and prospects in the catalysis of electroreduction of nitrogen to ammonia. *Nature Catalysis* **2019,** *2* (4), 290-296.